Evaluation of Turbulence Models in Gas Dispersion

Alexander Moen
University of Bergen, Department of Physics and Technology
Bergen, Norway

A thesis in partial fulfilment of the requirements for the degree of *Master of Science* in the subject of Physics; Process Safety Technology

Acknowledgements

I would like to thank Gexcon AS for allowing me to write my master thesis in collaboration with their R & D department.

Further, I would like to thank my two supervisors Lorenzo Mauri and Vagesh D. Narasimhamurthy for providing me with this thesis, helpful feedback and discussion. I would also like to thank associate professor Bjørn. J. Arntzen for introducing me to Gexcon and helpful feedback with the thesis.

Lastly I would like to thank Lise A. Haveraaen for reading my thesis many times and providing much needed help with language. I would also like to thank Magne Haveraaen for reading my thesis and providing comments on it.

Bergen, June 2016
Alexander Moen

Abstract

Several earlier model validation studies for predicting gas dispersion scenarios have been conducted for the three RANS two-equation eddy viscosity turbulence models, the standard k-ϵ (SKE), Re-Normalisation group k-ϵ (RNG) and Realizable k-ϵ (Realizable). However, these studies have mainly validated one or two of the models, and have mostly used one simulation case as a basis for determining which model is the best suited for predicting such scenarios. In addition, the studies have shown conflicting results as to which model is ideal for dispersion simulations. The aim of the study was therefore to assess three well-known RANS two-equation eddy viscosity models, in four different gas dispersion cases. The purpose was to evaluate the models' behaviour compared to experimental data, in order to see which of the models was best suited for predicting dispersion scenarios. The cases used in the thesis were: CO_2 dispersion in a cross- wind, neutral dispersion in an urban environment, hydrogen jet impinging on a surface, and a dense jet dispersion on an industrial site. All simulations were conducted with a CFD software that partially resolved the geometry, and was designed for large complex multiscale flow scenarios. The most important parameters for assessing the turbulence models were accuracy of the simulation results and computational time used. Overall, SKE seemed to be the best-suited model for 3 out of 4 cases, and provided good results for all the scenarios. However, RNG also provided reasonably results in all cases, in a practical timeframe. Realizable was the model that commonly used longest computational time, and was found least suitable for 3 out of 4 cases.

Keywords: Standard k-ϵ turbulence model, Re-Normalisation group k-ϵ turbulence model, Realizable k-ϵ turbulence model, gas dispersion, consequence modelling, partially resolved geometry.

Contents

List of Figures

List of Tables

Nomenclature

Abbreviations

BC	Boundary Conditions	-
CFD	Computational Fluid Dynamics	-
CSF	Concentration safety factor	-
CV	Control volume	-
DNS	Direct Numerical Simulations	-
FLACS	FLame ACceleration Simulator	-
LES	Large Eddy Simulations	-
MP	Monitor points	-
PDR	Porosity Distributed Resistance	-
RANS	Reynolds Averaged Navier-Stokes	-
RNG	Re-Normalisation Group k-ϵ model	-
SKE	Standard k-ϵ model	-
TKE	Turbulence Kinetic Energy	-

Dimensionless Groups

Fr	Densimetric Froude number	-
Gr	Grashof number	-
Re	Reynolds number	-
Ri	Richardson number	-

Greek Letters

β_j	Area porosity	-
β_v	Volume porosity	-
$\Delta i_{\min}$	Minimum grid cell size	m

δ	Kronecker delta	-
ϵ	Dissipation of turbulent kinetic energy	m^2/s^3
μ	Dynamic viscosity	Pa s
μ_{eff}	Effective viscosity	Pa s
ν	Kinematic viscosity	m^2/s
ν_t	Turbulent viscosity	Pas
ρ	Density	kg/m^3
σ	Prandtl-schmidt number	-
σ_{ij}	Stress tensor	N/m^2
ζ	mixture fraction	-

Roman Letters

$\dot{m}$	mass rate	kg/s
$\dot{Q}$	Heat rate	Js^{-1}
$C_{0,1,2,3}$	General constants	-
C_{ϵ_1}	Constant in the SKE, RNG and Realizable turbulence model	-
C_{ϵ_2}	Constant in the SKE turbulence model	-
$C^*_{\epsilon_2}$	Constant in the Realizable model	-
C_μ	Parameter in eddy viscosity model, often assumed to be constant	-
f_i	Geometry based parameter	-
$F_{o,i}$	Flow resistance	N
$F_{w,i}$	Flow resistance	N
g	Gravitational constant	$9.81 m/s^2$
G_0	Turbulence production from sub-grid model	m^2/s^3
G_b	Turbulence production from buoyancy	m^2/s^3
G_w	Turbulence production from wall-function	m^2/s^3

h	Specific enthalpy	Jkg^{-1}
k	Turbulent kinetic energy	$\mathrm{m}^2/\mathrm{s}^2$
L	Characteristic length	m
N_i	Number of grid cells in ith direction	-
P	Pressure	Pa
$P_{k/\epsilon}$	Production rate of TKE or dissipation	$\mathrm{m}^2/\mathrm{s}^3$
Q	Volume flow	m^3/s
S	Strain rate	1/s
T	Temperature	Kelvin
$T^{(v)}$	Viscous stress	$\mathrm{N/m}^2$
u	Velocity	m/s
V	Volume	m^3
x	Distance	m

Subscript

$*$	Friction	-
0	Start	-
eff	effective	-
a	Ambient fluid	-
b	Buoyancy	-
g	Released gas	-
i	Spatial index	-
j	Spatial index	-
k	Spatial index	-
t	Turbulent	-

1 Introduction

The major objective of this thesis is to assess and validate different turbulence models in gas dispersion scenarios, with particular focus on scenarios generated by accidental releases. Dispersion is a release of gas that is spread either through a self-motivating force, external force, or a mix of these. Dispersed gases can be toxic, flammable, asphyxiating or radioactive, and hazardous for our health and safety. In addition, if a flammable gas cloud is ignited, it can lead to a large explosion [1]. Usually, we see dispersion in industrial settings. However, dispersion can also take the form of pollution. With the growth of urban areas and the increase in road traffic, dispersing pollution increases within limited areas, making a dangerous living environment. Therefore it is important to monitor and accurately predict gas dispersion, both in industrial processes and urban areas [1, 2, 3]. Predicting gas dispersion can help us design mitigation procedures and/or prevention equipment, such as gas detectors, alarms and shutdown procedures. In addition, it can be useful when planning procedures preventing any escalation of an accidental release [4].

There are mainly two methods one can use to understand and predict dispersions, experiments or numerical methods. In order to use experimental data, a wide range of small to large scale experiments are required. Furthermore, as experiments depend on physical constructions, they often have high expenditures, and post-experiment moderations can be hard to perform. As well as measurements in experiments often depend upon a set number of probes, only measuring certain places, which limits what can be measured. Using experiments to understand and predict dispersion can therefore be a very time and resource consuming procedure. Consequently there are limited experimental data available for making new predictions about gas dispersion [1]. Numerical methods based on Computational Fluid Dynamics (CFD) are increasing in popularity, and are often preferred over experiments [1, 5]. CFD uses the governing equations of fluid flow (conservation laws for mass, momentum and energy [6]), allowing for easy control of individual parameters. CFD can also provide three-dimensional views, which help in process analyses of dispersion scenarios [7]. CFD is now a well-used method, and it can be used to assess different phenomena, including pollution, gas detection, and explosion hazards, in addition to making it possible to design safer structures [1, 8], such as oil platforms and nuclear plants.

Even though CFD is a well-used and powerful numerical method used for simulating flows, it is based on numerical assumptions, and therefore may not

reproduce experiments completely. Contrary to experiments, which studies real-life dispersion scenarios, CFD simulates dispersion by solving equations. The governing equations are continuous, but the numerical approximations solve the equations in a discrete fashion, so-called discretization [9]. Discretization divides space and time into a number of discrete points. The equations are only solved at these points, and not continuously. The volume between the discrete points in space is known as control volume or grid cell, and the procedure of dividing space into grid cells is known as gridding or meshing. By increasing the number of discrete points in a given computational domain, the accuracy of the CFD prediction improves. However, this demands more computational time and thus has large memory requirements. The CFD's accuracy depends on several parameters, including grid resolution, boundary conditions, geometrical representations, numerical approximations and turbulence models [7]. Turbulence models are especially important choices in CFD modelling, as turbulence occurs in almost all dispersion cases, and greatly affects the nature of the dispersion [7, 10, 11].

Turbulent flows and dispersion are characterised by random, unsteady, chaotic and three-dimensional behaviour, and are therefore hard to predict and describe [12]. In turbulent flows, rotational flow structures are often visible. These rotational structures are called eddies or vortices [12]. Turbulent flow consists of a wide spectrum of eddies, which vary in size, length and time scales [12]. In the rotational flow structure, energy in general is retrieved from the mean flow into the largest eddy, which transfers some of the energy to a smaller eddy, which again transfers the energy downwards in a cascade process to the smallest eddy [12]. The smallest eddy is limited by viscous force, and its kinetic energy dissipates into internal energy and has an isotropic structure [12]. The largest eddies are dominated by inertial forces and are highly anisotropically arranged.

Because of its inherent complexity, turbulence poses a challenge for CFD simulations. This challenge is mainly due to the ratio of the largest to the smallest eddy size, which usually is in the order of 10^6. This implies that in order to resolve all scales of eddy motions, the grid size should be in the order of a μm, a method adopted in the so-called direct numerical simulation (DNS). However, such DNS computations will require a very large amount of computation- time and memory, practically making it unfeasible to simulate industrial flows [12, 13]. As a consequence of the high computational costs associated with solving the equations directly, numerous turbulence models have been developed in order to reduce these costs, e.g. RANS, LES, and related techniques. Even though more accurate models exist, the approach

considered most practical, making it the most used model today, especially in industrial settings, is the Reynolds averaged Navier-Stokes (RANS) model [5, 12]. Several different RANS turbulence models exist, but the most common is the standard k-ϵ eddy-viscosity model. Previous testing of this model has provided accurate results in a practical timeframe over a wide range of dispersed flows. Despite this, the model has several known limitations. This has led to the development of other RANS turbulence models, in order to provide more robust models, with accurate results for a wider flow and dispersion scenarios. Two such models are the Realizable k-ϵ and the Re-Normalisation group k-ϵ model. Both are considered reliable eddy-viscosity turbulence models. Previous research has shown that both models have performed better than the original for some dispersion cases [14]. Some studies have also found that the Re-Normalisation group k-ϵ model works better than the Realizable k-ϵ model in some dispersion scenarios [2]. However, in other scenarios the original, standard k-ϵ has been found to work better than both the Re-Normalisation group k-ϵ and the Realizable k-ϵ model [3]. As far as previous literature shows, there seems to be conflicting results between which models is the preferred model for dispersion. Furthermore, there are few comparative studies of the three models. Thus there seems to be a need for comparative studies over a wide range of dispersion cases and flows, to assess which model may provide the best results.

In addition to validation, there is a need to assess turbulence models' performance in complex geometries, such as oil platforms or industrial sites [15]. With complex geometries it may become impractical to resolve the grid around the obstacles, as the size ratio between the largest and the smallest object may be large; the bulk scale of an industrial geometry has a characteristic length of 100 to 1000 meters. It is especially impractical to resolve all geometry on the grid due to the limitations imposed by current computer speed and memory [1]. This problem is somewhat solved by treating larger geometries "on-grid", i.e. well resolved grid around them, and smaller geometries "sub-grid", i.e. geometries smaller than the grid or not aligned with the grid are accounted by special sub-grid models. This implies that there is not only a discretisation assumption, but also a sub-grid modelling assumption. This approach is popularly termed porosity/distributed resistance (PDR) method, and often used for large multiscale geometries. The experience gained with CFD softwares that uses PDR, such as FLACS, has revealed that the PDR concept is one of the best ways to solve different flows in complex geometries [16]. However, there seems to be a lack of studies where a CFD software that partially resolves the geometry is used, and thus what effect it might have on different turbulence models.

Therefore, the aim of the study was to assess three well-known RANS two-equation eddy viscosity models, in four different gas dispersion cases. The purpose was to evaluate the models' behaviour compared to experimental data, in order to see which of the models was best suited for predicting dispersion scenarios. Also, a CFD software that uses partially resolved geometry was used to see its effect. Accordingly, the main research question for this thesis is:

Which of the existing turbulence models in the CFD software FLACS, i.e.: standard k-ϵ model, RNG k-ϵ model and Realizable k-ϵ model, is better suited for simulating gas dispersions when partially resolved geometry is used?

To answer this research question, four dispersion cases were chosen. These cases where simulations of previously conducted experiments, and covered a wide spectre of dispersion scenarios. Table 1.1 presents an overview of the study cases. The purpose of each case is to examine which of the turbulence models would best predict the dispersion scenario. The most important parameters to evaluate the models' performance was the ability to reproduce experimental results, computational time used and numerical stability.

Table 1.1: Case Overview.

	Type of gas	Geometry	Release condition	Ambient
Study case 1	Dense	Complex	Laminar, low momentum	Turbulent wind
Study case 2	Neutral	Simple	Laminar, low momentum	Turbulent wind
Study case 3	Buoyant	Simple	Turbulent, high momentum	No wind
Study case 4	Dense	Complex	Turbulent, high momentum	Turbulent open-air wind

2 Background

This chapter describes the basic theory of gas dispersion, turbulence modelling and FLACS. The intention is not to present the theory in full detail, but to highlight important concepts that are needed in order to better understand the models and dispersion. The reader is thus referred to the original papers and manuscripts for more details.

2.1 Gas dispersion

A general definition of dispersion is the spatial spreading and distribution of matter (like gas particulates, etc.). A broader definition of dispersion is a generalised diffusion that accounts for molecular diffusion plus the diffusion inducted by turbulence. Thus, turbulence is important for dispersion. Here a distinction between two types of gas releases was used: jets and plumes. There is more than one way to define both these concepts. One way takes into account the density of the surrounding fluid with the leaked gas. When the buoyancy forces are negligible, the release is termed jet, conversely if buoyancy forces dominate or affects the flow greatly, it is termed plume [17]. Another definition of plume and jet has its origin in where the fluid motion draws it source of kinetic energy and momentum flux from. If the leak comes from a pressure drop through an orifice, the leak will be seen as a jet [18]. However, if the leak originates from body forces, the leak is seen as a plume [18]. Regardless of the original character of the leak, in calm homogeneous surroundings, all leaks will eventually become plumes far away from the origin of release [17].

A dispersion consists of the interaction between a plume/jet and the surrounding flow field, where both the fluid field and the plume/jet is affected by the geometry [10]. Thus, as a jet or a plume develops from its origin, it will interact with the ambient flow field and geometry, creating concentration changes. A change in concentration is intimately tied to the rate of entrainment from surrounding fluid, i.e. the rate at which surrounding fluid is mixed within the boundaries of the jet or plume [18]. Therefore, the larger the velocity difference between the gas and the surrounding fluid is, the larger the entrainment and mixing will be. Indeed, the relative velocity of the jet/plume to the velocity of the surrounding fluid generates small-scale turbulence, or small eddies, which increases entrainment and mixing between the gas and the surrounding fluid at the interface. Thus, initial momentum, velocity and turbulence of the leak and surrounding fluid are factors deciding the mixing process.

As seen in the distinction between jets and plumes, density plays an important role in gas dispersion. When the dispersed gas has a density less than the surrounding fluid, the gas cloud will be lighter than the surrounding fluid. This is called a buoyant gas and it has buoyancy characteristics. When the dispersed gas has a density greater than the surrounding fluid, the gas cloud will be heavier than the surrounding fluid. This gas is termed as dense, and has a negative buoyancy. When the dispersed gas has a density equal or close to the surrounding fluid, the gas cloud will be neutral with its surroundings, and its movement is not affected by gravity. Buoyancy often have a high impact in production and destruction of turbulence inside a plume [19].

To identify the characteristics of a dispersion case certain dimensionless numbers will be introduced here. These numbers identify if a gas is dense, neutral or buoyant, and if the dispersion is turbulent. The first dimensionless number to be introduced is the Richardson number. The Richardson number provides an indication of how a dense gas affects the dispersion, by relating the stabilising effects' density (potential energy) on the kinetic energy of the ambient turbulence [20]. There exists many definitions of the Richardson number, but here, unless stated differently, the Richardson number is defined as [20]:

$$Ri = \frac{g(\rho_g - \rho_a)Q}{\rho_a u_*^2 LU} \tag{1}$$

Here ρ_a and ρ_g represents the density of ambient fluid and the gas, respectively; Q is the volume flow of the gas from the source, L is a characteristic length, u_* is the friction velocity, U is the ambient mean velocity and g is the gravitational acceleration constant. A value of ten for the Richardson number can be considered as limit for density effects to dominate over kinetic energy of the ambient turbulence [20]. Thus the release tends to stratify in layers with different densities.

The next number to be introduced is the densimetric Froude number. The densimetric Froude number is also used for determining density effects. The densimetric Froude number represents the inertial force divided by gravitational force, which provides a ratio of inertial forces to the weight of the fluid.

The densimetric Froude number is defined as [20]:

$$Fr = \frac{u_0}{\sqrt{g^{'} L}} \tag{2}$$

$$g^{'} = g\frac{\rho_g - \rho_a}{\rho_a} \tag{3}$$

Here u_0 is the initial velocity of the gas. A densimetric Froude number greater than one indicates that inertial forces are dominant over gravitational forces. A densimetric Froude number less than one indicates that gravitational forces are dominant.

The third number to be introduced is the Grashof number. The Grashof number tells if a buoyant plume or jet is turbulent. There are other numbers providing information about the turbulence, but they do not account for buoyancy effects. Consequently the Grashof number is a parameter that accounts for buoyancy effects, and will identify if a buoyant plume/jet actually is turbulent, even though the momentum of the leak may be low [18]. The Grashof number is defined as [18]:

$$G_r = \frac{gx^3\sigma(T_g - T_a)}{\nu_g^2} \tag{4}$$

Were x is a measure of the vertical distance above the source, σ is the volumetric thermal expansion coefficient (approximately equal to $\frac{1}{T}$, for an ideal gas), T is temperature in Kelvin, T_g and T_a represent the temperature of the gas and air respectively, ν_g is the kinematic viscosity of the gas. A Grashof number greater than 3×10^8 indicates that the plume/jet is turbulent [18].

The last number to be introduced is the Reynolds number. The Reynolds number is the most common parameter used to determine whether a flow is turbulent or not. The Reynolds number is defined as:

$$Re = \frac{uL\rho}{\nu} \tag{5}$$

where u, L ρ and ν is velocity, characteristic length, density and kinematic viscosity respectively. In a turbulent flow, a high Reynolds number would indicate that the kinetic energy of the turbulent motion is high, whereas a low Reynolds number would indicate that the kinetic energy of the turbulent motion is low. A high Reynolds number would also indicate a large difference between the largest and the smallest eddy [11].

Table 2.1 presents an overview of the four different numbers

Table 2.1: Overview of defined non-dimensional numbers.

	Indicating effect of Body force	Indicating Turbulence
Richardson number	Yes	No
Densimetric Froude number	Yes	No
Grashof number	No	Yes, but used only if body forces are dominant
Reynolds number	No	Yes, but may mislead if body forces are dominant

2.2 Turbulence models

2.2.1 Reynolds averaged Navier-Stokes

In RANS, the Navier-Stokes equations are averaged. This means that components that deviate from the mean are removed, thereby resulting in equations governing the mean flow. As a consequence of averaging the Navier-Stokes equations, a closure problem arises. The closure problem has its origin in the extra terms, called the Reynolds stresses. This Reynolds stress represents the interaction of the fluctuations and the mean, and because of it, turbulence models are required to close the set of equations. Several models that close the set of equations exist. The models used and that consequently will be presented is: the standard k-ϵ (SKE), Re-Normalisation Group k-ϵ (RNG) and the Realizable k-ϵ (Realizable) turbulence model. All equations are written with the Einstein notation or Einstein summation convention. The Einstein summation convention is a tensor rule implying summation over repeated indices in a formula.

The equations that describe any flow and dispersion motions, including tur-

bulent dispersion, are known as the Navier-Stokes equations [11].

$$\rho[\frac{\partial \tilde{u}_i}{\partial t} + \tilde{u}_j \frac{\partial \tilde{u}_i}{\partial x_j}] = -\frac{\partial \tilde{p}}{\partial x_i} + \frac{\partial \tilde{t}_{ij}^{(v)}}{\partial x_j} \quad (6)$$

$$\frac{\partial \tilde{\rho}}{\partial t} + \tilde{u}_j \frac{\partial \tilde{\rho}}{\partial x_j} + \tilde{\rho} \frac{\partial \tilde{u}_j}{\partial x_j} = 0 \quad (7)$$

$$\frac{\partial}{\partial t}(\tilde{\rho} e_0) + \frac{\partial}{\partial x_j}\left[\tilde{\rho}\tilde{u}_j\tilde{e}_0 + \tilde{u}_j\tilde{p} + \tilde{q}_j - \tilde{u}_i\tilde{t}_{ij}^{(v)}\right] = 0 \quad (8)$$

Here the symbol , ˜, represents the instantaneous component, u_i, x_i, p, e_0, q and $t_{ij}^{(v)}$ represents velocity and space in the different directions, pressure, total energy, heat flux and viscous stress, respectively. There are three equations in Navier-Stokes equations, the first correspond to the momentum (equation (6))- the second continuity- (equation (7)) and the third is the energy equation (equation (8)). The continuity equation formulates the conservation of mass [9]. The momentum equation has its origin in Newton's second law [9]. The energy equation has its origin in conservation of energy [9]. There are several ways of averaging the Navier-Stokes equations. In order to easily show the averaging scheme and the RANS models the equations presented will be the *incompressible time averaged* equations. While the equations used in the simulations was the *compressible Favre average* equations. Favre averaging is the best scheme, when large variations in density are expected [21]. All the results and points that arise from time-averaging are transferable to Favre averaging. As for Favre averaging, time-averaging splits the instantaneous variable into two quantities: an average and a fluctuating variable.

$$\tilde{u}_i = U_i + u_i \quad (9)$$

$$\tilde{p} = P + p \quad (10)$$

$$\tilde{t}_{ij}^{(v)} = T_{ij}^{(v)} + t_{ij}^{(v)} \quad (11)$$

In this equation, upper case letters and lower case letters represents the mean and the fluctuating components, respectively. Using the split of variables, inside the Navier-Stokes equations and average, the results of the algebraic manipulation is (energy equation not included here):

$$\rho[\frac{\partial U_i}{\partial t} + U_j \frac{\partial U_i}{\partial x_j}] = -\frac{\partial P}{\partial x_i} + \frac{\partial}{\partial x_j}[T_{ij}^{(v)} - \rho\langle u_i u_j\rangle] \quad (12)$$

$$\frac{\partial U_j}{\partial x_j} = 0 \quad (13)$$

Where $\langle\rangle$ means that it is averaged. In equation (12) a new term has appeared in the momentum equation, as a consequence of averaging. The new term can be seen inside the square brackets on the right of equation (12). The new term, $\langle u_i u_j \rangle$, has the dimension of a stress, but is not a stress in itself [22]. This term, $\langle u_i u_j \rangle$ is the Reynolds stress [22]. The Reynolds stress represents the contribution from the fluctuating part (deviation of the mean) on the mean, also seen as turbulent transport [23]. The Reynolds stress is a very important part of turbulence in any flow calculations and exact calculations of the Reynolds stress is paramount in order to calculate and simulate flows and dispersions. It is also important to note that the Reynolds stress arises directly from the *flow* itself and is not a property of the fluid, but of the flow [22]. In equation (12-13) there are 4 equations and 10 unknowns (U_1, U_2, U_3, P, $\langle u_1 u_1 \rangle$, $\langle u_2 u_2 \rangle$, $\langle u_3 u_3 \rangle$, $\langle u_1 u_2 \rangle$, $\langle u_1 u_3 \rangle$, $\langle u_2 u_3 \rangle$) which implies that a closure problem exists. The closure problem from the averaging procedure is often referred to as the turbulence closure problem [22].

There has been some research on solving the Reynolds stress by creating a direct transport equation. Such transport equations are termed the Reynolds stress equation. The problem with such an equation is that it also has a closure problem. A Reynolds stress equation does not give a simple equation that can be used to solve the turbulent closure problem, instead a new exceedingly complex equation is created [22]. Thus modelling the Reynolds stress is, for industrial flows, a more practical solution than trying to solve transport equations for it.

2.2.2 The Boussinesq assumption

One of the first attempts to model the Reynolds stress was by using the Boussinesq assumption [11]. In this assumption, the Reynolds stress was replaced with an eddy (or turbulent) viscosity [13, 24, 25]. The eddy viscosity is in analogy with the molecular viscosity. Just as how the momentum transfer caused by the molecular motion in a fluid can be described by molecular viscosity, so can momentum transfer caused by the eddy motion be described by an eddy viscosity. It is important to notice, just as with the Reynolds stress, that the eddy viscosity is a parameter that is not dependent on the fluid (as molecular viscosity is), but on the *flow* itself [26]. Many RANS turbulence models use the Boussinesq assumption, or some variation of it, as a starting point. All of the turbulence models in this thesis uses the Boussinesq assumption, which is defined as:

$$\langle u_i u_j \rangle = -2\nu_t S_{ij} + \frac{2}{3}\delta_{ij}\frac{1}{2}\langle u_i u_i \rangle \tag{14}$$

Here ν_t is the eddy viscosity, $S_{ij} = \frac{1}{2}[\frac{\partial U_i}{\partial x_j} + \frac{\partial U_j}{\partial x_i}]$ is the mean strain term, and δ_{ij} is the Kronecker delta defined as:

$$\delta_{ij} = \begin{cases} 0 & \text{if } i \neq j \\ 1 & \text{if } i = j \end{cases} \tag{15}$$

The Reynolds stress is then linearly related to the mean strain rate, and consequently it is the eddy viscosity that needs to be modelled [27]. Thus by the Boussinesq assumption, one has reduced the number of unknowns from six to one [26]. The turbulent viscosity is not homogeneous (it varies in space), it is however assumed to be isotropic (it is the same in all direction), which is valid for some flows, but not for all.

Even though we have decreased the number of unknowns to ν_t, it is not a straightforward unknown to solve, as it depends on the fluid. Usually ν_t is expressed as a function of a velocity and a length scale that is characteristic of local turbulence [27]. Expressing ν_t as a function will define how ν_t is calculated, and how the eddy viscosity is modelled. There are generally three classifications for modelling the eddy viscosity: zero-, one- and two-equation models [27]. The number of equations refer to the number of transport equations that are additionally needed to calculate the eddy viscosity in the zero-, one- or two-equation models [27].

Zero- and one-equation models are generally not considered in today's application, as they tend to fail in complex flows [27]. Thus, the two-equation models are the most common [27]. Two-equation models are widely used and tested, but not on scales typical of accidental releases in industrial or urban sites. Therefore, the two-equation eddy viscosity models were used in the current study, in order to validated their performances in different dispersion scenarios. All two-equation models in this thesis modelled the eddy viscosity as shown in equation (16), with the Boussinesq assumption, but with some variations, described later.

$$\nu_t = C_\mu \frac{k^2}{\epsilon} \tag{16}$$

In this equation, one assumes that the turbulent viscosity varies with the turbulent kinetic energy, k, and the dissipation rate of this kinetic energy, ϵ. C_μ is a non-dimensional quantity, often assumed to be constant. Thus in order to close and calculate the average Navier-Stokes equations, two additional transport equations are required, one for k and one for ϵ [28].

The turbulent kinetic energy, k, is defined as the sum of all normal Reynolds stresses, or in equation form:

$$k = \frac{1}{2}\langle(u_1^2 + u_2^2 + u_3^2)\rangle = \frac{1}{2}\langle u_i u_i\rangle \tag{17}$$

The dissipation, ϵ, is defined as:

$$\epsilon = 2\nu\langle s_{ij} s_{ij}\rangle \tag{18}$$

To find these quantities we need transport equations that show us their behaviour, with the goal of calculating the kinetic energy, the dissipation rate of the kinetic energy and the turbulent viscosity.

In an eddy viscosity model, one does not wish to generate non-physical results, as a consequence of the situation being non-realizable. The realizable condition is defined through mathematical constraint developed to hinder the flow becoming unphysical. The realizable condition is defined as:

$$\langle u_i u_i\rangle > 1 \tag{19}$$

$$\frac{\langle u_i u_j\rangle}{\langle u_i u_j\rangle\langle u_i u_j\rangle} \leq 1 \tag{20}$$

There is no Einstein summation over indices for equation (19-20). In equation (19-20) one states that the normal Reynolds stress must be non-negative and the Schwarz inequality must be satisfied. There is a problem with the Boussinesq assumption (equation (14)) in that for some situations this model will become non-realizable, such as in the case of large normal strain rates [25]. In some flow situations S_{ii} can become large, violating the realizable condition and creating non-physical situations. This is a well-known weakness in some turbulence models.

The k-equation is the same in all models used in this thesis, and is presented below. The ϵ equation is different and will be described for each model. The k-equation can be derived by contracting the free indices in the Reynolds strain equation (see [22] for derivation):

$$\begin{aligned}[\frac{\partial}{\partial t} + U_j\frac{\partial}{\partial x_j}]k = \frac{\partial}{\partial x_j}\{-\frac{1}{\rho}\langle p u_i\rangle\delta_{ij} - \frac{1}{2}\langle u_i u_i u_j\rangle + 2\nu\langle s_{ij} u_i\rangle\}+ \\ - \langle u_i u_j\rangle\frac{\partial U_i}{\partial x_j} - 2\nu\langle s_{ij} s_{ij}\rangle\end{aligned} \tag{21}$$

Each of the different terms can be identified and has a unique role to play in the overall turbulent kinetic energy balance [22]. Briefly they are:

- The rate of change of fluctuating kinetic energy, given in energy per unit mass. This is due to non-stationarity; i.e., time dependence of the mean [22]:

$$\frac{\partial k}{\partial t}$$

- The rate of kinetic energy per unit mass due to convection (or advection) by the mean flow through an inhomogeneous field [22]:

$$U_j \frac{\partial k}{\partial x_j}$$

- Transport of kinetic energy in an inhomogeneous field due to pressure fluctuations, turbulence and viscous stresses [22].

$$-\frac{1}{\rho}\langle p u_i \rangle \delta_{ij} - \frac{1}{2}\langle u_i u_i u_j \rangle + 2\nu \langle s_{ij} u_i \rangle$$

- Rate of production of turbulence kinetic energy per unit mass [22]:

$$\langle u_i u_j \rangle \frac{\partial U_i}{\partial x_j}$$

- Rate of dissipation of turbulence kinetic energy per unit mass due to viscous stresses [22]:

$$\epsilon = 2\nu \langle s_{ij} s_{ij} \rangle$$

The equation (21) represents a transport equation for k. As the current form of the k-equation has turbulent fluctuation terms that are unknown, a further assumption is used, which was a gradient assumption. In the gradient assumption, the diffusion of the kinetic energy is proportional to the gradient of the kinetic energy [29]. Consequently, the transport of kinetic energy by pressure fluctuations, turbulence and viscous stresses are model with a gradient assumption. The final and commonly used k-equation is seen in equation (22).

$$\begin{aligned} \frac{\partial k}{\partial t} + U_j \frac{\partial k}{\partial x_j} &= \frac{\partial}{\partial x_j}[(\nu + \frac{\nu_t}{\sigma_k})\frac{\partial k}{\partial x_j}] + P_k - \epsilon \\ P_k &= \nu_t S^2 \\ \sigma_k &= 1.0 \\ S &= \sqrt{2 S_{ij} S_{ij}} \\ S_{ij} &= \frac{1}{2}(\frac{\partial U_i}{\partial x_j} + \frac{\partial U_j}{\partial x_i}) \end{aligned} \tag{22}$$

Originally, the gradient assumption resulted in the production term defined as above: $P_k = \nu_t S^2$, which included only strain. However, extra terms are often included. For all simulations performed here, extra production terms, including the effects of buoyancy, wall-treatment and sub-grid model were included in the P_k term. These extra terms in the P_k term was added in the CFD FLACS software and will be presented in section 2.3. The inclusion of the Prandtl number, σ_k, relates the diffusivity of k to the turbulent viscosity.

2.2.3 The Standard k-ϵ turbulence model (SKE)

One of the first two-equation RANS eddy viscosity models created was the k-ϵ turbulence model. Harlow and Nakayama first proposed a version of the model in 1968 [30], and it was was further developed by Launder and Spalding in 1973 [29]. Today, this turbulence model is a highly tested model, which has produced good results in many dispersion scenarios [8].

The SKE model uses the Boussinesq assumption as already defined (see equation (16)). The constant C_μ is derived from a wide range of experiments and set to 0.09 for all simulation performed with SKE. For the ϵ equation an exact equation, as for the k equation, can also be found, but it is a very complicated equation, and in the end many of the terms are found negligible and seldom used [26]. Therefore the ϵ equation is modelled like the k equation [26]. Consequently, the ϵ equation should include a convection term, C, a diffusion term, D, a production term, P, and a destruction term, Ψ [26], resulting in:

$$C = P + D - \Psi \tag{23}$$

By looking into the dimensions of the k equation, the production, diffusion and destruction term for the epsilon equation is further assumed [26]:

$$P - \Psi = \frac{\epsilon}{k}(c_1 \langle u_i u_j \rangle \frac{\partial U_i}{\partial x_j} - c_2 \epsilon) \tag{24}$$

Where c_1 and c_2 are unknown coefficients. The diffusion term in the ϵ equation was modelled by using a standard gradient hypothesis [26]:

$$D = \frac{\partial}{\partial x_j}[(\nu + \frac{\nu_t}{\sigma_\epsilon})\frac{\partial \epsilon}{\partial x_j}] \tag{25}$$

Resulting in an ϵ equation:

$$\frac{\partial \epsilon}{\partial t} + U_j \frac{\partial \epsilon}{\partial x_j} = \frac{\epsilon}{k}(c_1 \langle u_i u_j \rangle \frac{\partial U_i}{\partial x_j} - c_2 \epsilon) + \frac{\partial}{\partial x_j}[(\nu + \frac{\nu_t}{\sigma_\epsilon})\frac{\partial \epsilon}{\partial x_j}] \tag{26}$$

It is common to rearrange the ϵ equation such that the final equation has the form:

$$\begin{aligned}
\frac{\partial \epsilon}{\partial t} + U_j \frac{\partial \epsilon}{\partial x_j} &= \frac{\partial}{\partial x_j}[(\nu + \frac{\nu_t}{\sigma_\epsilon})\frac{\partial \epsilon}{\partial x_j}] + \frac{\epsilon}{k}(C_{\epsilon 1} P_\epsilon - C_{\epsilon 2}\epsilon) \\
P_\epsilon &= \nu_t S^2 \\
S &= \sqrt{2 S_{ij} S_{ij}} \\
S_{ij} &= \frac{1}{2}(\frac{\partial U_i}{\partial x_j} + \frac{\partial U_j}{\partial x_i}) \\
C_{\epsilon 1} &= 1.44 \\
C_{\epsilon 2} &= 1.92 \\
\sigma_\epsilon &= 1.3
\end{aligned} \tag{27}$$

It is important to note that the epsilon equation defined here is a simplified model that has shortcomings [26]. As the ϵ and k equation interlocks, if the k-equation includes other terms in the production the ϵ-equation must also include them. This in order to balance out the production of turbulent energy. The extra term of the ϵ equation are described in the section about FLACS[1].

When using k and ϵ equation as previously defined, in addition to the Boussinesq assumption, a closed set of equations are produced, making it possible to solve the average Navier-Stokes equations. SKE is a popular model to implement in CFD programs, consequently the shortcomings of SKE are known: SKE is only valid for fully turbulent flows (high Reynolds numbers), its performance in swirling and rotating flows is weak, as well as flows with strong separation, axis-symmetric jets, flows driven by thermal effects and flows containing large adverse pressure gradients. Despite the shortcomings, SKE is applicable and gives satisfactory results for most flows.

2.2.4 Re-Normalisation group k-ϵ Turbulence Model (RNG)

In 1986, Yakhot and Orszag developed a new two-equation eddy viscosity k-ϵ turbulence model [24], which was further developed and finalised in 1992 by Yakhot and Smith [31]. The idea behind Re-Normalisation group theory is that since turbulent flows at high Reynolds number have a wide range of length and time scales, one could systematically remove the smaller scales until a point where the remaining scales are resolvable with available computer capacities [31].

[1] section 2.3

For the RNG k-ϵ model the equation governing dissipation is

$$\begin{aligned}
\frac{\partial \epsilon}{\partial t} + U_j \frac{\partial \epsilon}{\partial x_j} &= \frac{\partial}{\partial x_j}[(\nu + \frac{\nu_t}{\sigma_\epsilon})\frac{\partial \epsilon}{\partial x_j}] + \frac{\epsilon}{k}(C_{\epsilon 1} P_\epsilon - C^*_{\epsilon 2}\epsilon) \\
P_\epsilon &= \nu_t S^2 \\
C_{\epsilon 1} &= 1.68 \\
C^*_{\epsilon 2} &= 1.42 - \frac{\eta(1-\eta/4.38)}{1+0.012\eta^3} \\
\eta &= \frac{k}{\epsilon} S \\
\sigma_\epsilon &= 0.719.
\end{aligned} \tag{28}$$

The main difference between RNG and SKE is the substitution of the constant $C_{\epsilon 2}$ to $C^*_{\epsilon 2}$, which modifies the rate of destruction for ϵ [32]. The destruction term in the equation (28) was modified such that the RNG model would properly account for the larger dissipation rate experienced in the laminar regions near solid surfaces [32]. This modification of ϵ makes the model more accurate and reliable for a wider class of flows [7]. $C^*_{\epsilon 2}$ may vary in magnitude and sign, and can influence the turbulent viscosity, especially in regions of large-strain rates [33]. As well as the change in the destruction term, the Prandlt number, σ_ϵ, and other modelled constant have also been changed. Here the modelled constants are more analytical derived than for SKE, where the constants are based upon experiments. The extra features described above, allows the RNG model to partially account for strong anisotropy in regions of large shear. This enables the RNG model to provide improved predictions of separated flows and anisotropic large-scale eddies [33]. RNG works equally good for low and high Reynolds number [24].

The RNG model uses the Boussinesq assumption as it is presented in equation (14), where the constant C_μ had the value of 0.085. This value of C_μ was derived in an analytical way.

2.2.5 Realizable k-ϵ turbulence model (Realizable)

In 1995, Shih et al. developed a new two-equations eddy viscosity k-ϵ turbulence model [25]. This model has a new dissipation equation closer related to the exact equation of dissipation in addition to a further developed Boussinesq assumption, making the term C_μ to vary between flows. The change in C_μ makes the model realizable[2] and consequently it is named Realizable [25].

[2] see section 2.2.2, equation (19-20)

The Realizable model is the only model that will hinder violation of the realizable constraints. The conditions defining realizable, are mathematical conditions that hinders non-physical conditions. A turbulence model that use these constraints will possibly perform better for flows with high mean shear rate or massive separation, as such flows have a tendency to become non-realizable. The reason for such flow to become non-realizable is that the eddy viscosity will overpredict the mean strain compared to the standard eddy viscosity formulation [25], see equation (14).

In addition to a new formulation for the eddy viscosity, the dissipation equation was also adjusted in order to provide more appropriate length scales for turbulence [25]. It has been stated that in the SKE model, the dissipation equation is assumed and modelled on a similar structure as for the turbulent kinetic energy equation [25]. In the Realizable turbulence model, a dissipation equation, which is more physically related to the analytical derived dissipation equation (see [25] for derivation), was developed and used [25]. The Realizable dissipation model is a simpler and more robust model compared to the one used in the standard k-ϵ model [25].

$$\begin{aligned}
\frac{\partial \epsilon}{\partial t} + U_j \frac{\partial \epsilon}{\partial x_j} &= \frac{\partial}{\partial x_j}[(\nu + \frac{\nu_t}{\sigma_\epsilon})\frac{\partial \epsilon}{\partial x_j}] + C_1 S\epsilon - C_2 \frac{\epsilon^2}{k + \sqrt{\nu\epsilon}} \\
C_1 &= max[0.43, \frac{\eta}{\eta + 5}] \\
C_2 &= 1.68 \\
\sigma_\epsilon &= 1.2 \\
\eta &= S\frac{k}{\epsilon} \\
S &= 2\sqrt{2S_{ij}S_{ij}}.
\end{aligned} \tag{29}$$

Here ϵ, U_j, x_j, ν_t, k and ν represents dissipation rate, average velocity, space, turbulent viscosity, turbulent kinetic energy and molecular viscosity respectively.

The difference between the SKE and the Realizable dissipation model mainly lies in the destruction term [25]. When comparing equation (29) with equation (26)), we see that the dissipation equation for the Realizable dissipation equation does not include the Reynolds stress in the production term. When a second-order closure scheme is used, the dissipation model becomes more robust by not including the Reynolds stress [25]. The reason that the model is more robust when the Reynolds stress is not used in the equation, lies

in that the S normally behaves better than the Reynolds stress in numerical calculations, especially for flow calculations with poor initial conditions [25].

The Realizable dissipation model do not include P_ϵ, as this has been changed with the more robust S, instead of the Reynolds stress. If additional terms are included in the k equation for production of turbulence, these extra terms should also be included in the ϵ equation, and will be added in the following form

$$+ C_3 \frac{\epsilon}{k}(G_i) \tag{30}$$

Were G_i is the extra production terms and C_3 is a constant (in FLACS equal to $C_{\epsilon 1}$).

The Realizable eddy viscosity model has the form of equation (14), but the term C_μ is modelled and not assumed constant as it is for SKE and RNG. The reason that C_μ is not a constant, is that experiments on boundary layer and homogeneous shear flows have shown that the value of C_μ is different in each case [25]. For Realizable C_μ has the form

$$C_\mu = \frac{1}{A_0 + A_s U^{(*)} \frac{k}{\epsilon}}. \tag{31}$$

Were A_s and $U^{(*)}$ are functions of velocity gradients and A_0 was a model coefficient (assumed constant). The eddy viscosity formulation satisfies the realizability constraints. All constants defined for Realizable was equal for all simulations performed here.

All turbulence models are summarised and can be seen in table 2.2.

Table 2.2: An overview of the turbulence equations used.

	Expression of eddy viscosity ν_t	Transport equation of k	Transport equation of ϵ
Standard k-ϵ (SKE)	$\nu_t = C_\mu k\frac{k}{\epsilon}$, $C_\mu = 0.09$	$\frac{\partial k}{\partial t} + U_j\frac{\partial k}{\partial x_j} = \frac{\partial}{\partial x_j}[(\nu + \frac{\nu_t}{\sigma_k})\frac{\partial k}{\partial x_j}] + P_k - \epsilon$, $P_k = \nu_t S^2$, $\sigma_k = 1.0$, $S = \sqrt{2S_{ij}S_{ij}}$, $S_{ij} = \frac{1}{2}(\frac{\partial U_i}{\partial x_j} + \frac{\partial U_j}{\partial x_i})$	$\frac{\partial \epsilon}{\partial t} + U_j\frac{\partial \epsilon}{\partial x_j} = \frac{\partial}{\partial x_j}[(\nu + \frac{\nu_t}{\sigma_\epsilon})\frac{\partial \epsilon}{\partial x_j}] + \frac{\epsilon}{k}(C_{\epsilon 1}P_\epsilon - C_{\epsilon 2}\epsilon)$, $C_{\epsilon 1} = 1.44$, $\sigma_\epsilon = 1.3$, $C_{\epsilon 2} = 1.92$, $P_\epsilon = \nu_t S^2$
RNG k-ϵ (RNG)	$\nu_t = C_\mu k\frac{k}{\epsilon}$, $C_\mu = 0.085$	$\frac{\partial k}{\partial t} + U_j\frac{\partial k}{\partial x_j} = \frac{\partial}{\partial x_j}[(\nu + \frac{\nu_t}{\sigma_k})\frac{\partial k}{\partial x_j}] + P_k - \epsilon$, P_k and σ_k as above	$\frac{\partial \epsilon}{\partial t} + U_j\frac{\partial \epsilon}{\partial x_j} = \frac{\partial}{\partial x_j}[(\nu + \frac{\nu_t}{\sigma_\epsilon})\frac{\partial \epsilon}{\partial x_j}] + \frac{\epsilon}{k}(C_{\epsilon 1}P_\epsilon - C^*_{\epsilon 2}\epsilon)$, $C_{\epsilon 1} = 1.68$, $\sigma_\epsilon = 0.719$, $C^*_{\epsilon 2} = 1.42 - \frac{\eta(1-\eta/4.38)}{1+0.012\eta^3}$, $\eta = \frac{k}{\epsilon}S$, $P_\epsilon = \nu_t S^2$
Realizable k-ϵ (Realizable)	$\nu_t = C_\mu k\frac{k}{\epsilon}$, $C_\mu = \frac{1}{A_0 + A_s U^{(*)}\frac{k}{\epsilon}}$	$\frac{\partial k}{\partial t} + U_j\frac{\partial k}{\partial x_j} = \frac{\partial}{\partial x_j}[(\nu + \frac{\nu_t}{\sigma_k})\frac{\partial k}{\partial x_j}] + P_k - \epsilon$, P_k and σ_k as above	$\frac{\partial \epsilon}{\partial t} + U_j\frac{\partial \epsilon}{\partial x_j} = \frac{\partial}{\partial x_j}[(\nu + \frac{\nu_t}{\sigma_k})\frac{\partial \epsilon}{\partial x_j}] + C_1 S\epsilon - C_2\frac{\epsilon^2}{k+\sqrt{\nu\epsilon}}$, $C_1 = max[0.43, \frac{\eta}{\eta+5}]$, $C_2 = 1.9$, $\sigma_\epsilon = 1.2$

2.3 FLACS

FLACS is a commercial CFD software developed and validated, by GexCon AS, which has been ongoing since the 1980s, with support from major oil and gas companies. FLACS is developed to perform engineering calculations related to safety and security in industry and society in general [34]. FLACS is a CFD software especially developed to be used on industrial complex flows and is very well tested over a wide range of flows. Consequently, it is a well-known and stable program known to give good results, where simulation errors from programming are few, and thus remaining errors will either be numerical- or user-errors. This was the reason FLACS was chosen as the CFD software, and all simulations was performed with FLACS, version 10.4.

FLACS governing equations are transport equations for: conservation of mass (equation (32)), momentum (equation (33)), enthalpy (equation (34)) and mixture fraction (equation (35)) [16]. The governing equations and the equations for SKE are display below, with emphasis on how PDR is integrated into the equations. For more information see [34].

$$\frac{\partial}{\partial t}(\beta_v \rho) + \frac{\partial}{\partial x_j}(\beta_j \rho u_j) = \frac{\dot{m}}{V} \tag{32}$$

$$\begin{aligned} \frac{\partial}{\partial t}(\beta_v \rho u_i) + \frac{\partial}{\partial x_j}(\beta_j \rho u_i u_j) &= -\beta_v \frac{\partial \rho}{\partial x_i} + \frac{\partial}{\partial x_j}(\beta_j \sigma_{ij}) + \\ +F_{o,i} + \beta_v F_{w,i} &+ \beta_v(\rho - \rho_0) g_i \end{aligned} \tag{33}$$

$$\frac{\partial}{\partial t}(\beta_v \rho h) + \frac{\partial}{\partial x_j}(\beta_j \rho u_j h) = \frac{\partial}{\partial x_j}(\beta_j \frac{\nu_{\text{eff}}}{\sigma_h} \frac{\partial h}{\partial x_j}) + \beta_j \frac{Dp}{Dt} + \frac{\dot{Q}}{V} \tag{34}$$

$$\frac{\partial}{\partial t}(\beta_v \rho \zeta) + \frac{\partial}{\partial x_j}(\beta_j \rho u_j \zeta) = \frac{\partial}{\partial x_j}(\beta_j \frac{\nu_{\text{eff}}}{\sigma_\zeta} \frac{\partial \zeta}{\partial x_j}) \tag{35}$$

$$\frac{\partial}{\partial t}(\beta_v \rho k) + \frac{\partial}{\partial x_j}(\beta_j \rho u_j k) = \frac{\partial}{\partial x_j}(\beta_j \frac{\nu_{\text{eff}}}{\sigma_k} \frac{\partial k}{\partial x_j}) + \beta_v P_k - \beta_v \rho \epsilon \tag{36}$$

$$\begin{aligned} \frac{\partial}{\partial t}(\beta_v \rho \epsilon) + \frac{\partial}{\partial x_j}(\beta_j \rho u_j \epsilon) &= \frac{\partial}{\partial x_j}(\beta_j \frac{\nu_{\text{eff}}}{\sigma_\epsilon} \frac{\partial \epsilon}{\partial x_j}) + \\ +\beta_v P_\epsilon &- C_{2\epsilon} \beta_v \rho \frac{\epsilon^2}{k} \end{aligned} \tag{37}$$

Where β_v is volume porosity, β_j is area porosity in the j direction, $\dot{m}$ is mass rate, V is volume, σ_{ij} is the stress tensor, $F_{o,i}$ is flow resistance due to subgrid obstructions , $F_{w,i}$ is flow resistance due to walls, h is specific enthalpy, σ_h is Prandtl-Schmidt number for enthalpy, ν_{eff} is effective viscosity ($\nu + \frac{\nu_t}{\sigma}$), $\dot{Q}$ is heat rate, ζ is mixture fraction and σ_ζ is Prandtl-Schmidt number for mixture fraction, respectively. For a further description of the numbers and

how they are modelled see [34]. Table 2.3 shows an overview of the Prandtl-Schmidt number used for this thesis and their values.

Table 2.3: Prandtl-Schmidt Numbers

σ_h	σ_ζ	σ_k	σ_ϵ
0.7	0.7	1	1.2

FLACS solves these equation by favre averaged compressible flow formulation on a Cartesian grid, with the finite volume method [16]. FLACS uses a second order scheme for calculating diffusive fluxes combined with a second order κ scheme for convective fluxes [34]. The κ scheme is a hybrid scheme with weighting between 2nd order upwind and 2nd order central difference [34]. The time stepping scheme used in FLACS is a first order backward Euler scheme [34]. Iterations in FLACS are repeated until a mass residual of less than 10^{-4} is obtained [34].

FLACS uses the porosity / distributed resistance (PDR) modelling concept for sub-grid objects. In PDR there is no attempt to resolve any individual obstacles by the grid, instead the objects effect is accounted for by introducing appropriate porosities and distributed resistances into the flow equations (β_j and β_v, see equations (32) to (37)) [1]. Using the porosity concept for complex geometries is an ability to represent large objects on-grid and smaller objects sub-grid, or even all objects sub-grid. Here porosity will be assigned to each grid cell, and the amount of porosity, in each cell, represent local congestion and confinement [34]. Assigning the grid cells with the correct amount of porosity allows sub-grid objects to contribute for flow resistance and turbulence generation in simulations, without being resolved by the grid [34]. Porosity calculations are often divided into two types (as in FLACS): area and volume porosities. Volume porosity is the mean blockage inside the control volume (CV), and the area porosity is the blockage of the surface area of the CV [34]. Porosity calculations provide a value between 0 and 1, where a value of 0 means that the CV is completely blocked and a value of 1 mean that the CV is fully open [34]. The sub-grid contribution increases when the dimensions of objects decreases [34]. This increase in contribution is done, so that there is a gradual transition from sub grid to on-grid representation.

The following boundary conditions (BC) in FLACS were used, and must be specify for the outer boundaries of the simulation domain (higher and lower X-,Y,-Z) [34]:

- Euler
- Nozzle
- Wind

The Euler BC gives that the Euler equations (equations for inviscid flow) are discretised for the boundary element for outflow, assuming ambient pressure outside the boundary [34]. For the Nozzle BC a discharge coefficient is calculated from the area porosity and a drag coefficient [34]. The wind BC models an external wind field [34]. In this wind model, velocity and turbulence profiles are specified, either by setting some turbulence parameters manually or by choosing one of the atmospheric stability Pasquill classes [34]. In the Wind BC the wind speed at a given reference height can be specified along with wind direction, relative turbulence intensity and length scale and wind build up time. Walls and floor override the BC preventing the flow from crossing solid walls and imposing source terms for turbulence and momentum according to the wall functions.

In the k-equation (equation (22)) for all the turbulence models the production term, P_k is defined as: $P_k = \nu_t S^2$. Using P_k this way only accounts for the contribution of the flow shear stress. In FLACS three additional terms are added in the production term, P_k. These terms are equal and added for all the models, SKE, RNG and Realizable. The extra terms in P_k accounts for turbulence production that has its origin in: buoyancy (G_b), sub-grid objects (G_o) and wall function (G_w).

The production of turbulence in the k-equation from buoyancy, G_b can be seen in equation (38). Here the model for the turbulence generation from buoyancy is presented. G_b work as a source term in the turbulence model.

$$\begin{aligned} G_b &= -\frac{1}{\rho}\frac{\mu_{\text{eff}}}{\sigma_b} g_i \frac{\partial \rho}{\partial x_i} \\ \mu_{\text{eff}} &= \mu + \rho C_\mu \frac{k^2}{\epsilon} \end{aligned} \tag{38}$$

Where G_b, σ_b, g_i, μ and $\rho C_\mu \frac{k^2}{\epsilon}$ represents turbulence generation from buoyancy, prandtl-schmidt number, gravitational acceleration, dynamic viscosity and the turbulent or eddy viscosity, respectively. In this model of buoyancy, the outcome may be different depending on the specific turbulence model, because of the different μ_{eff} or more specific C_μ values. How the C_μ changes through the different models may impact the modelling of the buoyancy differently.

The production of turbulence due to sub-grid objects, can be seen in equation (39). Here the turbulence generation, G_0 is modelled. G_0 work as a source term in the turbulence models [16].

$$G_0 = C_0 \beta_v \rho |\mathbf{u}| u^2 f_i \tag{39}$$

Where G_0, C_0, β_v, ρ, $\mathbf{u}$ and f_i represents turbulence generation from sub-grid, a model constant, volume fraction (from PDR), density, velocity and a geometry based parameter, respectively. It is important to notice that even though this model of sub-grid production is equal for all turbulence model, the outcome may be different depending on the specific turbulence model, because of how velocity may vary between models. Thus if one turbulence model dampens or enhances the velocity either overall or for certain areas, this again will affect the sub-grid modelling production term.

Close to walls and obstructions, there are boundary layers that often consist of steep gradients and peak values for the turbulent kinetic energy and dissipation rate [34]. Viscous forces often dominate over inertial effect close to surfaces [34]. To include the effects of boundary layers it is possible to either use a fine grid or model the effects with wall functions. Using a fine grid requires a lot of computational power and it is time demanding. Consequently, the common practice is to use wall-functions. In the CFD software FLACS wall functions are used. This wall function, G_w work as a source term in the turbulence models. The wall function model, G_w, can be seen in the FLACS manual, [34], and will not be outlined here.

Putting all of these contribution together results in the production term for the k-equation to equal:

$$P_k = \nu_t S^2 + C_0 \beta_v \rho |\mathbf{u}| u^2 f_i - \frac{1}{\rho} \frac{\mu_{\text{eff}}}{\sigma_b} g_i \frac{\partial \rho}{\partial x_i} + G_w = \nu_t S^2 + G_0 + G_b + G_w \tag{40}$$

As well as extra terms for the production term in the k-equation there are extra terms in the production term for the ϵ equation. These extra terms can be seen under in equation (41) for SKE and RNG

$$\frac{\epsilon}{k} C_{\epsilon 1} P_\epsilon = \frac{\epsilon}{k} C_{\epsilon 1} P_k (1 - C_{3\epsilon} \frac{G_b}{P_k} \frac{\mathbf{u} \times \mathbf{g}}{|\mathbf{u}||\mathbf{g}|}) + \epsilon_w. \tag{41}$$

Where G_b and P_k is as above. $C_{3\epsilon}$ is a constant equal to 0.8. As Realizable do not include a P_ϵ in its dissipation model, an extra term will be added to it:

$$+ \frac{\epsilon}{k} C_{\epsilon 1} (G_0 + G_b)(1 - C_{3\epsilon} \frac{G_b}{G_0 + G_b} \frac{\mathbf{u} \times \mathbf{g}}{|\mathbf{u}||\mathbf{g}|}) + \epsilon_w \tag{42}$$

Were ϵ_w is the dissipation of turbulent kinetic energy at the wall point [34]. ϵ_w is defined in the FLACS manual, [34], and is not presented here.

This implies that SKE, RNG and Realizable are all affected by buoyancy, non-resolved object by the grid (sub-grid objects) and wall functions in the k and in the ϵ equation, through extra models from FLACS.

3 Previous research

Several comparative studies using the SKE, RNG and Realizable have been conducted. However, these studies have been conducted under different environmental and release conditions, and comparisons between the studies are therefore difficult to do. Santiago et al., [14], for example, tested the three models in a plume dispersion in a street canyon, and found that both RNG and Realizable provided equally good results, and that SKE behaved poorly. Rahimi et al., [35], found similar results for a dense plume dispersion. Tauseef and colleagues, [4], on the other hand found that Realizable was better suited than both SKE and RNG, the Realizable model gave a higher peak value and a wider spread. In their study, the three models were tested in a dense plume dispersion in the presence of obstacles. Gildeh et al, [36], also found Realizable to be the best model. They tested the models in a dense jet dispersion. Other studies found that RNG outperformed the two other models [37, 2]. Chan et al., [37], for example, tested the three models in a plume pollutant dispersion in a street canyon. Tominage and Stathopoulos, [2], found similar results for a plume pollutant dispersion in a street canyon. Contrary to these results, Hang et al, [38], found that SKE was better than the other two models for simulating dispersion in an urban environment. They concluded that this was because SKE predicted better airflow velocity in weak wind regions, and this made SKE simulate more accurately compared to the two other models. Still other studies have found that there is no difference in the three models' accuracy [3]. Because most of these studies have been conducted under different dispersion scenarios, it has been suggested that the conflicting results are due to the diversity of gas dispersion scenarios. That some models function better under conditions such as high separation, impingement, low Reynolds number, whereas other models function better under conditions such as weak winds, high Reynolds number and jet dispersion. Thus the preferred model differs under the different environmental and leak conditions, and thus it might be situational. To support this, Klein et al. (2015), [27] did a large study of 13 different turbulence models in 8 different *fluid flows*. They concluded that none of the models were superior to the others and that the best-suited model was determined by the situation it was tested in. Nonetheless, many of the studies indicate that both RNG and Realizable are better suited for predicting gas dispersion, regardless of the gas dispersion scenarios [39, 35, 3, 14, 7].

Some explanations for why RNG and Realizable do it well in different dispersion scenarios have been suggested. Gildeh et al, for example, suggested that Realizable performs better because of how it deals with the turbulent

viscosity, and that the model gives more accurate predictions because of its non-constant values of C_μ, [36]. A similar explanation has been used for RNG, Chan et al. who tested the models in a street canyon also said it was because the turbulent viscosity term of RNG that provided the more accurate numerical results [37].

Another frequent finding in the literature is that SKE in general has been found to perform more poorly than the other models. Also here the literature points to different explanations. Santiago et al. believed that the poor results were due to the fact that SKE overpredicted turbulence near edges [14]. Tominaga and Stathopoulos found that SKE could not predict the general flow structure, such as the reverse flow on the roof, in a street canyon [2]. Lateb et al. (2013) concluded that the strong separation and recirculation found in their study, probably was the reason for SKE's inaccurate performance; SKE provided un-physical results breaking the realizable condition [7]. Rahimi and colleagues on the other hand, believed that SKE's lack of performance was due to how the turbulent viscosity was predicted, and because it was a low Reynolds number, RNG and Realizable performed better [35].

Because of these inconclusive and conflicting findings, there is a need for more comparative studies of SKE, RNG and Realizable turbulence models in a wider range of test cases.

4 Simulated dispersion scenarios

In this chapter the test cases used to assess the performance of different turbulence models are presented. A variety of dispersion scenarios was investigated, from plume and jets releases, dense, neutral and buoyant gases and simple geometries and complex geometries. The purpose of this chapter is thus to present the dispersion cases simulated, simulation setup, results and discussion of the performance of the turbulence models described in section 2.2, for each test case. All the test cases are replicas from full scale scenarios. The test cases were chosen to provide a wide range of dispersion scenarios, particularly for industrial dispersion, to test the turbulence models. The general methodology for each test case was: First build the geometry, second run preliminary tests, where wind profiles, boundary and initial conditions and grid sensitivity were performed and finally the turbulence models were tested.

The reason for running preliminary tests is to recreate the experimental setup within the numerical domain, in order to provide close simulation results to experimental results. This is important in order to judge the performance of a turbulence model since the experimental concentration are used as reference. This means that it is assumed that the experimental results are reproduced, in order to trust and relay on the turbulence test. All preliminary tests were simulated with the SKE turbulence model, and thus all pre-turbulence testing were based on this model.

For the turbulence testing, all simulations were run with the same computer and resources. This was done in order to compare the models in terms of computational time needed. The computer was a Dell Precision M4500, Intel(R) Core(TM) i7 CPU 2.0GHz, 8GB RAM and 4 cores (8 logical cores), where the models were tested with parallel execution using 2 cores. All simulations were run with the CFD software FLACS version 10.4. Where the common CPU usage ranged from 80-100% and memory usage ranged from 5-6GB. Run time can be decreased by factors such as: better CPU and memory capacity, better architecture of the computer, more cores, etc.

The main source of information in the cases came from concentration measurements, measured with probes, where accuracy was seldom provided. There exist experiments that provide measurements of turbulence, velocity and concentration, but they are rare, and limited to academic cases. As this thesis focused on presenting a wide range of dispersion scenarios, that mimic "real" scenarios in terms of complexity (geometrical and phenomenology) and characteristic scales (Re, Ri, Fi and Gr numbers) there is a limited

capacity of comparison between the turbulence models.

The cases chosen, were selected on basis of having as low a source of uncertainty as possible. In spite of this, the cases are limited to a visual comparison of graphs that show measured data, only for concentration data. It is often rather difficult to draw general conclusions from a visual comparison only and using only concentration to compare the models performances [5]. Thus it was often not possible to know how the models were performing inside the accuracy interval of the experimental measurement, or to know what happened between the probes or outside of the probes measurement areas. As it was possible to do model comparison of non-measured-test variables between the model this was done for some test cases. Care was taken when conclusion were based on these. Often initial condition, such as leak and ambient temperature, initial turbulence and pressure was not provided and had to be guessed, or for some cases tested. It was believed that the lack of data on initial conditions would mostly create errors that influenced all models ability to reconstruct the experimental values equally, not creating problems individually.

4.1 Case 1: Low momentum CO_2 plume in a cross-wind

For the first case, a wind tunnel experiment conducted at the Chemical Hazard Research Centre at the University of Arkansas was used for RANS model validation. The experiment consisted of a wind tunnel covered with small obstacles on the floor, where CO_2 was released at the centre of the tunnel. Because the obstacles on the floor were quite small they were not resolved by the grid in the simulations. This implies that sub-grid modelling was used in the simulations to account for the floor obstacles. This made for an interesting study, of an industrial dense gas release, where the dispersion was influenced by objects that were dependent on sub-grid modelling.

4.1.1 Experimental case

The wind tunnel that was used in the experiment was designed in order to study atmospheric dispersion of denser-than-air gases under various wind conditions [40]. The wind in the tunnel was driven by two large fans, which were designed to imitate neutral atmosphere. The floor in the tunnel was covered with small obstacles. The obstacles on the floor consisted of a L-shaped object, that represented ground roughness, hereafter referred to as roughness elements. These roughness elements were placed in a staggered

array at a constant distance between each subsequent element, both in the downwind and lateral directions. At the centre of the tunnel, there was a roughness element-free squared area, where the leak was injected. The size of the obstacle-free squared area was L^2, where L is the characteristic length ($L = \sqrt{0.3341}$). The tunnel was 3.69L high, 10.55L wide and 42.21L long, respectively. An overview of the tunnel and roughness elements with dimension can be seen in figure 4.1 and 4.2. For a more detailed description of the tunnel and experiment see Havens and Spicer [40].

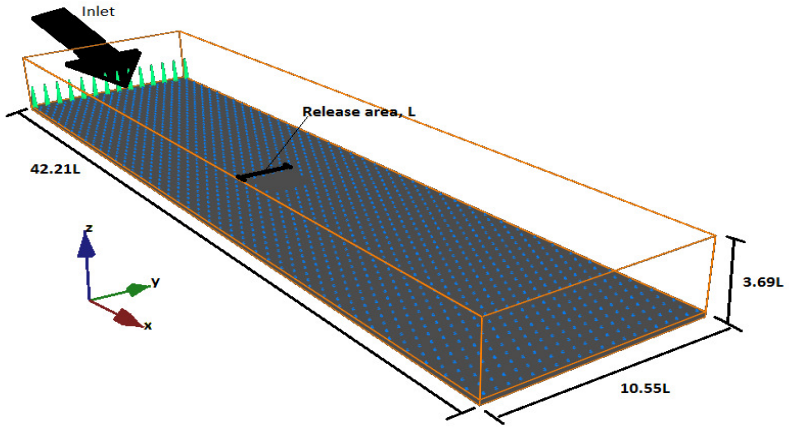

Figure 4.1: Wind tunnel; all of the lengths are given in L, which is the characteristic length. The floor of the wind tunnel is covered with roughness elements.

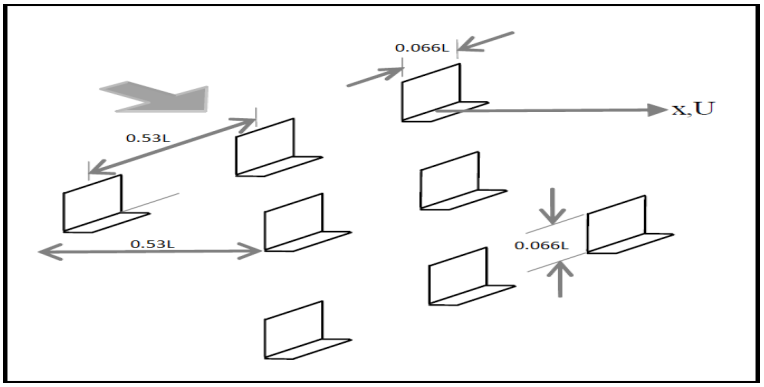

Figure 4.2: Roughness elements in the wind tunnel. All of the lengths are given in L, which is the characteristic length.

In the experiment, the wind flow was in positive X-direction. The wind was assumed to be air at standard conditions. The dispersed gas consisted of 33.4 standard litres per minute (slpm) CO_2 mixed with 0.5 slpm C_3H_8 tracer [40], meaning that the gas mainly consisted of denser-than-air CO_2. Because the gas was dense it may behave as a bluff body at the release location, which forces the wind to move around the gas at the leakage. This bluff-body-like behaviour was the reason why the square shaped release area was chosen to give the characteristic length, L. The gas release was a low-momentum negatively-buoyancy dispersion that exhibited plume behaviour. Because of the gas density the plume moved close to the floor, where the roughness elements had an impact on the plume behaviour and mixing of the air, creating patterns visible in the concentration plots. The Reynolds number of the gas release, based on L and the outflow *gas* velocity, was about 200. The Reynolds number of the wind, based on L and the downwind *air* flow velocity, was in the range of 3000 - 10 000, depending on the height from the floor (0-0.0009L). A Reynolds number of 200 is seen as a laminar flow, and a Reynolds number of 3000 - 10 000 is seen as turbulent. Thus the experiment was a continuous laminar gas release mixed with a turbulent down-wind airflow. Because a continuous gas release with a stable wind was used in the experiment, the air-gas mix reached a steady state after about 65-70 seconds. The Richardson number for this case was about 160 implying that, as expected, density played a large role.

Multiple measurement probes were placed in the wind tunnel at different X, Y and Z positions. The majority of the probes measured concentration, and the rest measured velocity. All the probes measuring concentration were placed at 5 different x-positions (x=0.95L, 1.52L, 3.03L, 4.1L, 6.2L) downstream of the leak, with varying distances in the y-direction (all in vicinity of y$\pm$2L) and at a constant height (z = 0.0009L). The velocity probes were placed at the centre before the release, at different heights. No information about the accuracy of the probes was given in the experimental report.

The concentration probes in the experiment were used for model validation, while the velocity probes were used to extract information about the wind profile in the tunnel. As the measurement probes were placed between -2L<Y<2L only the plume concentration was measured in the experiment.

4.1.2 Simulation setup

With the release area at (0,0,0) the simulation volume was, x: -5L to 10.7L, y: -5.3L to 5.3L and z: 0L to 1.04L. This simulation volume was chosen

in order to include wall and floor boundaries. The simulation volume was divided into a core and a stretched domain. The core domain was centred around the release area and mainly consisted of, x: -1.45L to 9.37L, y: -2.54L to 2.54L and z: 0L to 0.14L. Outside the core domain the stretched domain started and continued until the end of the simulation domain. The core domain consisted of a constant grid cell size. The grid cells in the stretched domain increased in size the further away from the core domain they were placed.

The size of the grid cells in the core domain was matched to the size of the roughness elements in X, Y and Z directions (all 0.066L). Boundary condition was defined as Nozzle for the outflow. The inflow and upper boundary condition were defined as Wind[3]. Solid walls at lateral ($\pm$y) and bottom (-z) boundaries imposed a no-slip boundary. Initial conditions about temperature, pressure, relative turbulence, etc. were not documented in the experiment, and thus were assumed to be at standard conditions. A reference height and velocity for the wind was documented: $z_{ref} = 0.12$L, $U_{ref} = 0.4$m/s and was used to simulate the wind. Unless stated differently, L and U_{ref} will be the characteristic length and velocity as stated for this case.

In the simulations, monitor points (MP) were defined at every measurement probes' location. MPs in FLACS corresponds to virtual sensors monitoring one or more variables in a continuous way (i.e. every time step). The MPs measured the same quantities as in the experiment as well as k, ϵ and velocity components. The MPs made it possible to do direct comparisons of experimental and simulation data for concentration, and to do model comparison for the other quantities. Since there was no accuracy provided from the experiment, only a visual and highest concentration value comparison was done. All simulations were run with a time duration of 70 seconds. The wind build up for 25 seconds, before the gas was released. The system reached a steady state after time iteration summing up to about 60-66 seconds.

Figure 4.3 represents a flow chart of all the tests that were conducted, and in which order they were performed. As a first step, preliminary tests were conducted in the following order: First, a geometry simulation was performed to control that the geometry was satisfactory with the experiment. After the geometry simulations were completed, 5 more simulations were performed, based on different wind profiles. These 5 wind-profile simulations were conducted in order to find the best-suited wind profile to replicate the

[3]For information about FLACS boundary conditions see section 2.3

experimental wind profile. Finally, when the best profile had been identified (in this case, wind profile 1), grid sensitivity tests were performed using 6 different grids. Based on the preliminary analyses, one grid was chosen, and the turbulence model validation tests were performed. The process, and the choices made will be presented in greater detail below.

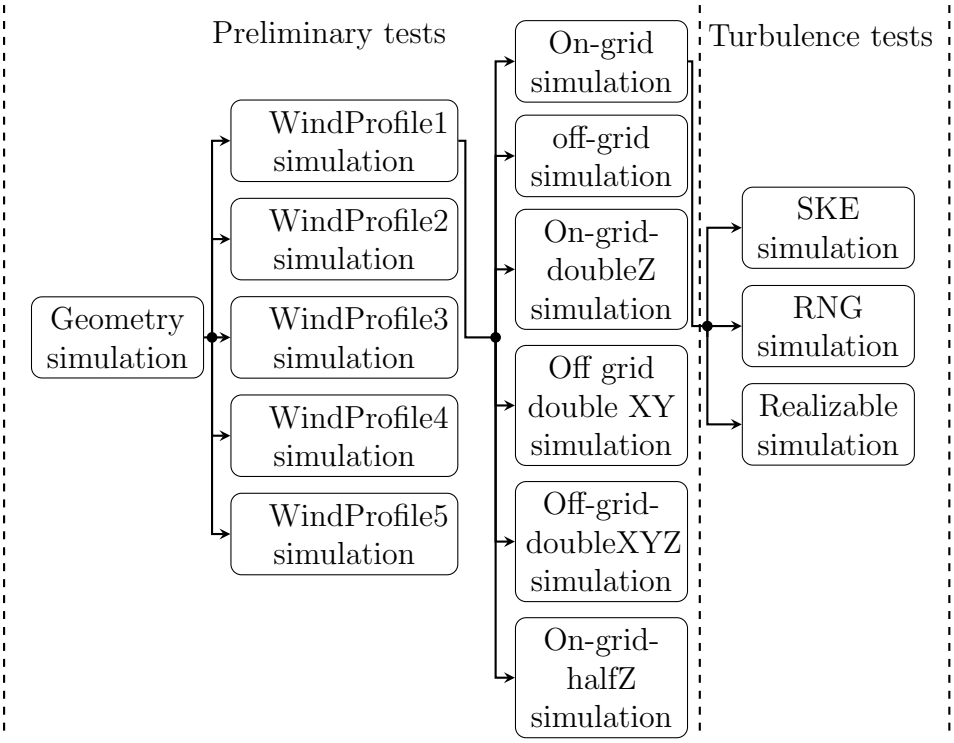

Figure 4.3: Flow chart, presenting which order the simulations were performed

The wind profiles were tested in the preliminary analyses changing the inflow conditions and verifying the velocity profile at the measurement location inside the wind tunnel. This was done in order to find the best fit according to the given experimental data. An overview of the tested wind profile is in table 4.1. Based on the results of figure 4.4 wind profile 1 was found to best replicate the experimental wind profile, as it was the profile best recreating the behaviour and with closest reference values (0.4 m/s at 0.067m).

Table 4.2 specifies the grid sensitivity test and highlights the different grids in addition to describing the concept behind each grid. The number of grid cells, in all directions (Nx, Ny and Nz) is also included in table 4.2, in addi-

Table 4.1: An overview of the differences in the different wind profiles.

Name	Wind speed at reference height [m/s]	Reference height [m]
Wind Profile 1	0.4	0.067
Wind Profile 2	0.45	0.067
Wind Profile 3	0.35	0.067
Wind Profile 4	0.4	0.06
Wind Profile 5	0.4	0.074

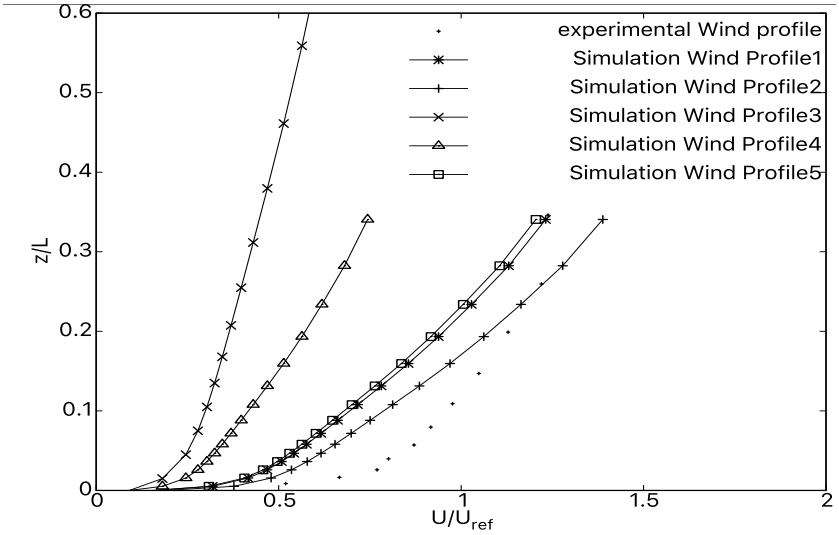

Figure 4.4: Different wind profiles compared with experimental wind profile. The vertical axis is z/L. The horizontal axis represents normalised U/U_{ref}.

tion to the minimum grid dimension ($\Delta i_{\min}$) in the different grids.

As well as a grid sensitivity test, i.e. testing grids with different Ni and Δi_{min}, a simple test was also included that tested the effect of amount of sub-grid modelling needed in the simulation. The test on amount of sub-grid modelling was the difference in results between the *On*- and *Off*-grid. The difference in concept between the on- and off-grid is illustrated in figure 4.5. Figure 4.5 represents a small selection of the floor on the wind tunnel. In this selection roughness elements and grid lines are represented. Grid lines are virtual lines going in X and Y direction in between grid points and is a helpful visualisation plot when it comes to display a mesh. If the lines are *off* or missing the outer surface of the roughness elements, as in figure 4.5a, the

Table 4.2: Grid name along with a short description, number of grid points in the grid, N_i, and minimum grid dimension in the grid, $\Delta i_{\min}$ for the remaining preliminary tests.

Type of grid	Description	Number of grid cells	Minimum grid dimension [m]
On-grid	This is the reference grid. Here the "L" shaped roughness elements blocks three faces of the grid cell.	Nx - 199 Ny - 116 Nz - 38	$\Delta X_{min} - 0.0381$ $\Delta Y_{min} - 0.0381$ $\Delta Z_{min} - 0.005$
Off-grid	This is the same as the reference grid, but the grid cells are slightly off the roughness elements in the x and y direction.	Nx - 199 Ny - 116 Nz - 38	$\Delta X_{min} - 0.0381$ $\Delta Y_{min} - 0.0381$ $\Delta Z_{min} - 0.005$
On-grid-doubleZ	This is an on-grid mesh. The grid cells have double in size in the z-direction, thus decreasing the number of grid cells in z-direction	Nx - 199 Ny - 116 Nz - 19	$\Delta X_{min} - 0.0381$ $\Delta Y_{min} - 0.0381$ $\Delta Z_{min} - 0.01$
Off-grid-doubleXY	This is an off-grid mesh. The grid cells have double in size both in x and in y direction, thus decreasing the number of grid cells.	Nx - 100 Ny - 60 Nz - 38	$\Delta X_{min} - 0.0758$ $\Delta Y_{min} - 0.0763$ $\Delta Z_{min} - 0.005$
Off-grid-doubleXYZ	This is an off-grid mesh. The grid cells have double in size both in x, y and in z direction, thus decreasing the number of grid cells	Nx - 100 Ny - 60 Nz - 19	$\Delta X_{min} - 0.0758$ $\Delta Y_{min} - 0.0763$ $\Delta Z_{min} - 0.01$
On-grid-halfZ	This is an on-grid mesh. The grid cells have halved in size in z direction, thus increasing the number of grid cells	Nx - 199 Ny - 116 Nz - 77	$\Delta X_{min} - 0.0381$ $\Delta Y_{min} - 0.0381$ $\Delta Z_{min} - 0.0029$

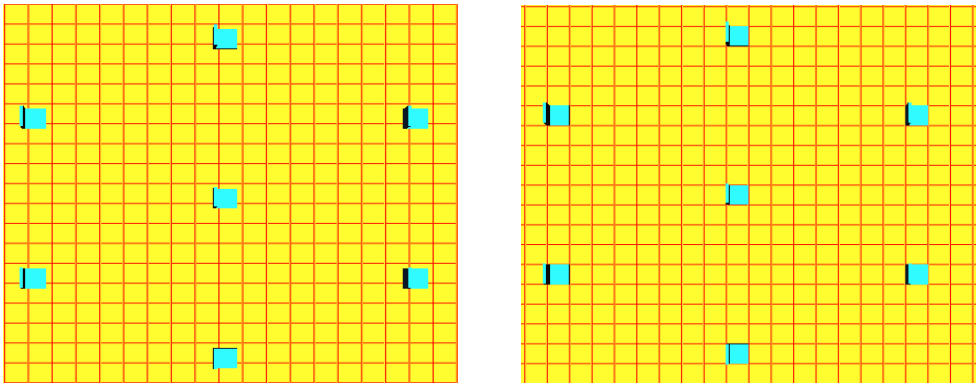

(a) *Off* grid, porous grid cells around the roughness elements.

(b) *On* grid, porosity limited to a single grid cell.

Figure 4.5: Difference in defining the grid on or off obstacles.

configuration is off-grid. If the lines are *on* or hitting the outer surfaces of the roughness element, as in figure 4.5b, the configuration is on-grid. In the on-grid configuration, contradictory to the off-grid configuration, the roughness elements were somewhat resolved by the grid. Indeed not all of the element was resolved by the grid, and in much of the stretched domain the grid lines missed the roughness element that increased the amount of sub-grid modelling. Thus both concepts needed sub-grid modelling, but the off-grid cases produced more porosity, creating a simple test on how the amount of sub-grid modelling affected the simulations.

The graphs in figure 4.6 show CO_2 concentration plots of all the grid tests represented in table 4.2 with experimental values where concentration measurements were made in the experiment. The vertical axis is the mole fraction, while the horizontal axis is y/L.

From the graphs of figure 4.6, the on-grid configuration was chosen as the optimal grid. There were no large differences in the grids for x>0.95L implying that no further grid resolution was needed. Furthermore, there was not a large difference between on- and off-grid. The on-grid mesh was chosen because it behaved best at x=0.95L as well as equally good for x>0.95L. In general, the concentration profile for all simulations is relatively close to the experimental data, however, the values are always lower.

As an extra note about the results from the preliminary tests, in the graph 4.6a the experimental concentration profile displays a double peak, while all

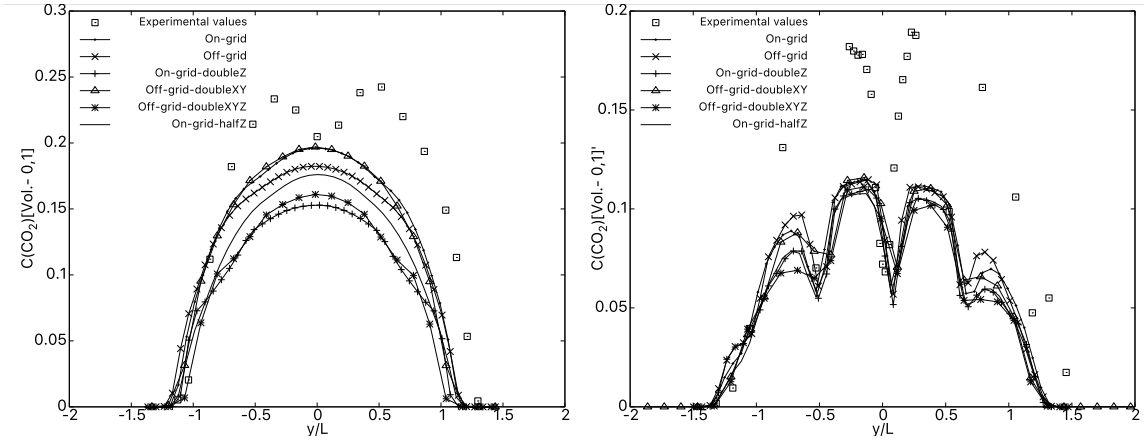

(a) x=0.95L

(b) x=1.52L

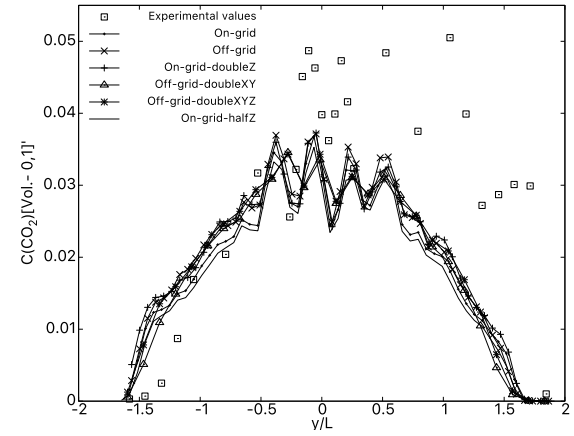

(c) x=3.03L

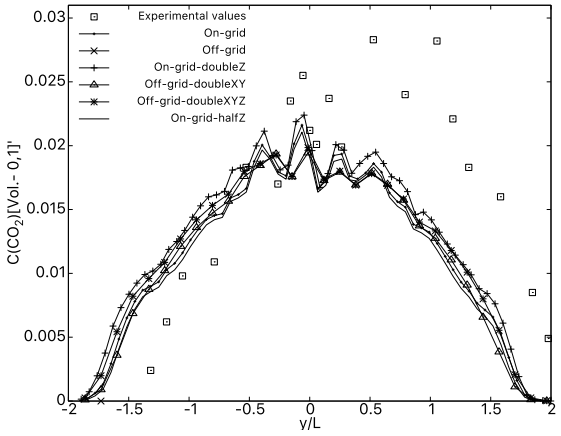

(d) x=4.1L

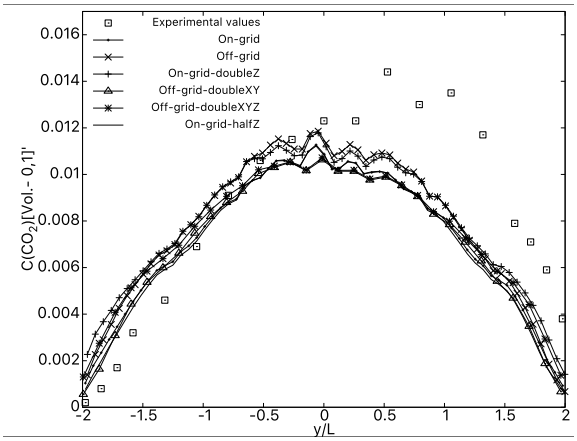

(e) x=6.2L

Figure 4.6: Predicted concentration from the six grids and the experimental data. All graphs are for y ±2L, z is fixed at 0.0009L while the x position varies.

of the simulation concentration profiles only had a single peak. It was first believed that this double peak stemmed from a gravitational effect as a result from the fact that the gas was heavy. Thus a new simulation was performed, using the on-grid setup, where the roughness elements for x>0 were removed, in order to reduce the turbulence and increase the Richardson number. The result from this test was that the double peak concentration could not be found at any spatial placement in the wind tunnel. Later in the process it was discovered that the experiment contained a blocked area at the release, that were not mentioned or described in the original experimental report [40]. The detailed description of the release geometry was found in an another report, [41], that also described the same experiment. It was believed that this different configuration was the reason for the lack of prediction of a double concentration peak as results from the simulations. It does not seem that this lack of object influences the plume behaviour or concentration level at other measuring placement. Thus the simulations were not repeated with inclusion of the modified leak geometry.

For x>1.52L the experimental concentration values starts to shift in the +Y direction. This was the result of a slight tilt in the tunnel. This tilt resulted in the experimental plume to drift towards the positive y-direction, and was reported as a highly repeatable result for all experiments performed in the wind tunnel [40]. The slight slope was not taken into account in the geometry of the simulation. This was simply because the slope was not well documented. The drift also made it hard to do any other quantitative comparison other than highest concentration and visualisation.

As well as a visual comparison of performances a quantitative comparison was also done. Table 4.3 shows an overview of Concentration safety factor (CSF), which represents a quantitative comparison through a dimensional factor defined as:

$$CSF = |\frac{(Simulation\ value)_{max}}{(Experimental\ value)_{max}}|$$

Here as well as for the visual inspection, the on-grid mesh seemed to give better results and recreating the experiment, as it had, overall, CSF values closes to one.

From all of these tests the on-grid mesh with Wind Profile 1 was chosen, because it closely recreated the experiment. The on-grid mesh was used further to test and validate the three turbulence models. No more tests were done, as more testing on either grid, boundary conditions or initial conditions

Table 4.3: Overview of the CSF of the different grids for the different x-positions.

	x=0.95L	x=1.52L	x=3.03L	x=4.1L	x=6.2L
On-grid CSF	0.809	0.605	0.728	0.764	0.783
Off-grid CSF	0.752	0.606	0.735	0.786	0.823
On-grid-doubleZ CSF	0.631	0.580	0.738	0.791	0.818
Off-grid-doubleXY CSF	0.812	0.612	0.684	0.687	0.738
Off-grid-doubleXYZ CSF	0.664	0.587	0.680	0.701	0.744
On-grid-halfZ CSF	0.726	0.569	0.699	0.744	0.779

did not seem necessary.

4.1.3 Results

All models reached a stable condition and no model differs greatly in used computational time. Table 4.5 show used clock time and it is seen that RNG was the most effective turbulence model. However, RNG only used a time-range of 2-6 hours shorter, which was not considered significant for choosing a model, when the whole simulation time was in the range of 112-120 hours.

Figure 4.7 presents the concentration at all the downwind position. Visually, in figure 4.7, SKE and RNG behave similar to each other, while Realizable stands out as the model giving the most conservative values. While all the models showed very similar behaviour and values close to the release, Realizable started to differ in concentration values further downwind. Farther from the release downstream Realizable depicted higher, more conservative concentration values while SKE and RNG gave almost equal values at all the downwind positions. This is also concerned from table 4.4 which shows the CSF values of the different models at all the downwind positions. Here as well as in the concentration graphs, Realizable predicts better the highest concentration values, especially farther downwind. As well as higher values, Realizable seemed to give a wider spread at downwind positions. Also seen is that Realizable has a more bumpy concentration curve than the other two models, that is believed to stem from concentration fluctuations.

Here as well as for the preliminary tests the missing two peak concentration at x=0.95L for the simulations was present, as well as the missing compensation of the tilt in the tunnel. From the graph 4.7a, which shows the concentration at x=0.95L, it was noticeable that Realizable had a different

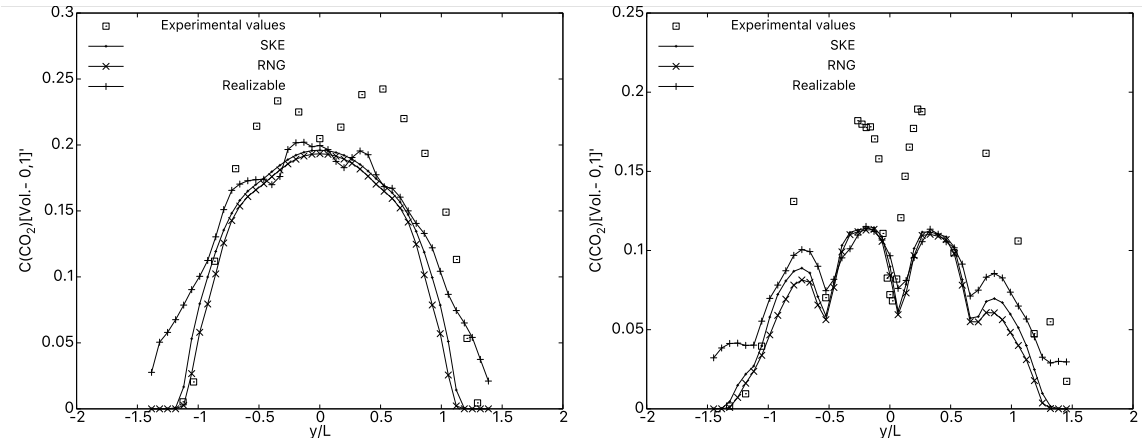

(a) x=0.95L

(b) x=1.52L

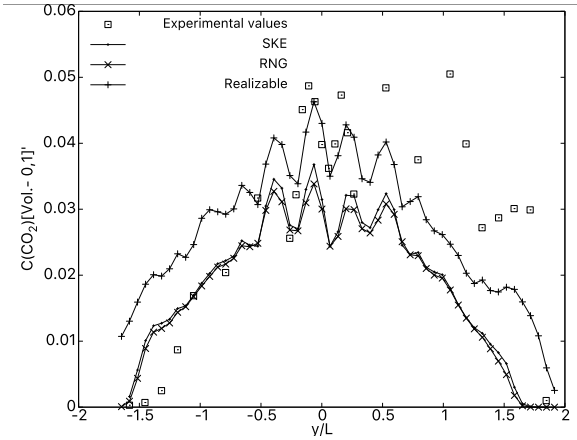

(c) x=3.03L

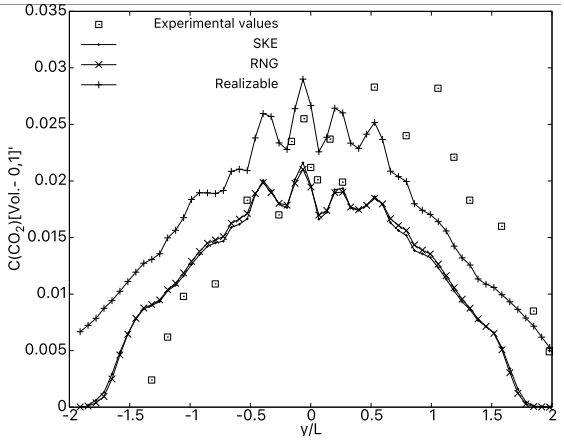

(d) x=4.1L

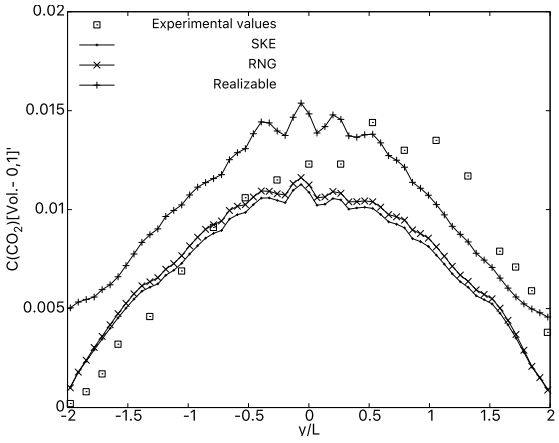

(e) x=6.2L

Figure 4.7: Concentration for SKE, RNG and Realizable and experimental data. All graphs shows y between ±2L and z fixed at 0.0009L.

Table 4.4: The CSF values for the different models.

	SKE	RNG	Realizable
x=0.95L	0.809	0.798	0.834
x=1.52L	0.605	0.599	0.609
x=3.03L	0.728	0.670	0.917
x=4.1L	0.764	0.743	1.025
x=6.2L	0.783	0.807	1.068

Table 4.5: Used clock time for simulation with the different models.

Model	SKE	RNG	Realizable
Time[hour]	119.56	111.3	117.04

concentration distribution than the others. Realizable seemed to oscillating slightly between the time steps and did not reach a fully steady state, but a quasi-steady state. This is not a great defect as the oscillation was only modest.

Because Realizable gave higher concentration values and a wider spread, turbulent kinetic energy (TKE) values were extracted from the SKE, RNG and Realizable to do model comparison, and find a possible explanation for this behaviour. There were no experimental data on TKE. In figure 4.8 the TKE values of the simulation at the same downwind positions as the concentration measurement are presented. The horizontal axis is y/L, while the vertical axis is TKE values normalised by a reference velocity.

From the graphs of figure 4.8 it was seen that Realizable had a different TKE profile close to the release and outside of the plume (y>2L and y<-2L) than SKE and RNG, which showed a very similar TKE profile. Whereas, the TKE for SKE and RNG increased rapidly farther away from y=0, TKE for Realizable decreased rapidly, going towards zero, farther away from y=0.

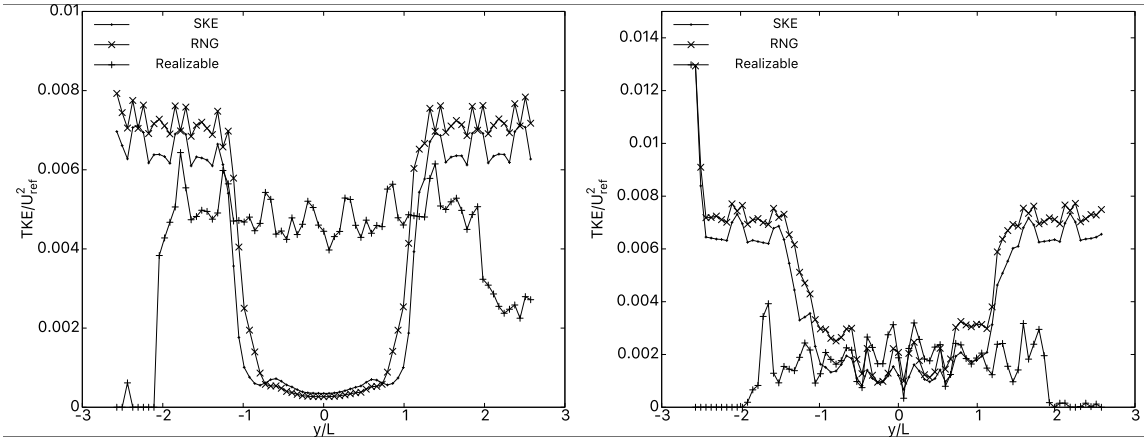

(a) x=0.95L

(b) x=1.52L

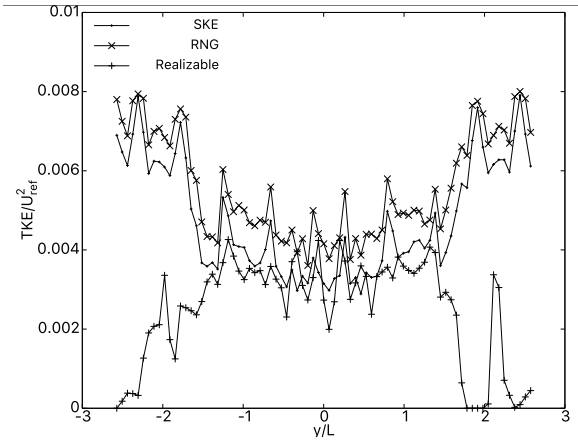

(c) x=3.03L

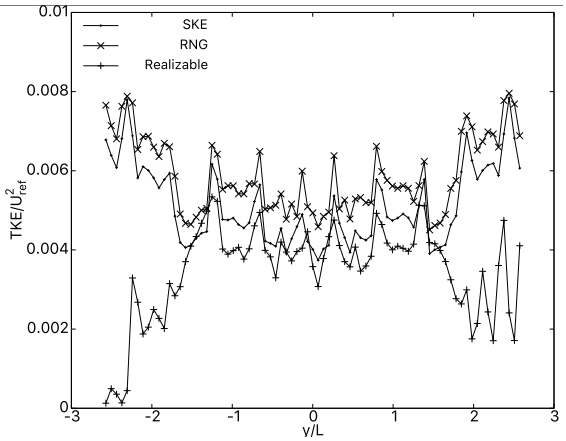

(d) x=4.1L

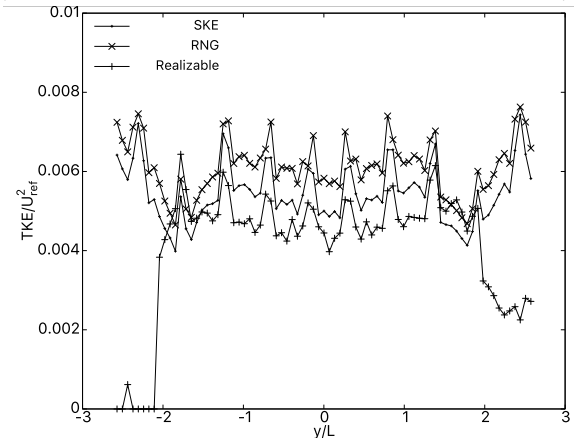

(e) x=6.2L

Figure 4.8: TKE/u^2_{ref} for SKE, RNG and Realizable and experimental data. All graphs shows y between -3L to 3L and z fixed at 0.0009L.

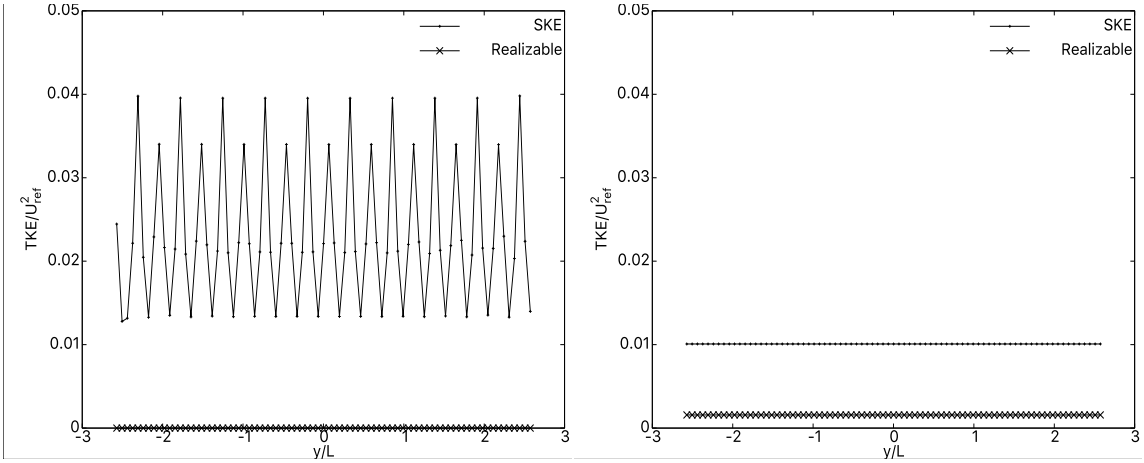

(a) TKE with obstacles. (b) TKE without obstacles.

Figure 4.9: TKE differences for with and without obstacles (hypothetical scenario without gas release, i.e. pure wind simulations).

Based on the difference in TKE profile between the models, four more simulations were conducted. These four simulation represented firstly one simulation with SKE and one with Realizable where the roughness elements had been removed, secondly one simulations with SKE and one with Realizable where roughness elements were present. For these four simulations the simulation volume was decreased, in X and Z direction, there was also no gas release, i.e. a pure wind flow simulation. The results of the with and without roughness elements can be seen in figure 4.9. Here TKE was taken upwind at -3.46L at z=0.0009L. When the obstacles were removed, and thus removed the need for modelling sub-grid objects, TKE was reduced for SKE and enhanced for Realizable, this reduced the difference in TKE between SKE and Realizable.

4.1.4 Discussion

The purpose of this case study was to examine which of the turbulence models, SKE, RNG and Realizable, would best predict a dense gas dispersion under a cross-wind with smaller-than grid sized objects on the floor. The following findings will be discussed: (1) Realizable simulated the experimental values most correctly, (2) Realizable had a different TKE profile outside of the plume compared to SKE and RNG.

In general, all the models were stable, used the same computational time, $\pm$ 5 hours, and produced reasonable answers. However, some differences

were found between the models: Although all the models provided similar concentration values close to the gas release, Realizable showed higher concentration values that closer resembled the experiment farther away from the release. Realizable was therefore considered to be the best suited model for simulating a dense dispersion under a cross-wind.

Whereas SKE and RNG detected smooth curves, Realizable seemed to predict concentration fluctuations. Concentration fluctuation are visible in the sense that the concentration curves are bumpy and not smooth. These bumpy features are likely to stem from buoyancy effects as a consequence of gravity slumping often seen with dense gas dispersion [4]. The ability to predict concentration fluctuations is important for optimising the placement of gas detection alarms, and can also assist in designing effective preventive and mitigation procedures [4]. It is therefore advantageous of Realizable to predict these fluctuations from a safety perspective. However, the experimental results were not sufficiently detailed to know if concentration fluctuation actually were present, and if Realizable predicted them at the correct place. Nonetheless, as the Richardson number indicated that density effected the dispersion, it is believed that concentration fluctuations were present. Consequently, it was a drawback that neither SKE or RNG seemed to predict any fluctuations in concentration values. Similar finding has also been found in other studies. In 2011 Tauseef et al., [4], for example, did a comparative study of SKE and Realizable in a heavy gas dispersion in presence of obstacles, and found that only Realizable was able to predict concentration fluctuation. Based on this, the researchers concluded that Realizable was the best suited model for predicting dispersion with a dense gas in present of obstacles [4]. Thus, it seemed as Realizable gave the best predictions, which was also supported from previous literature.

The second major finding in this case study was that Realizable predicted very different TKE values outside the plume compared to SKE and RNG. Both SKE and RNG showed high TKE values outside of the plume, whereas Realizable provided much lower TKE values. Since the turbulent wind was present outside of the plume, one would expect to see a high TKE value there.

This might be explained from the interaction between the turbulence models and the sub-grid. Other studies have shown that modifying individual parts in the production term of the k and ϵ equations in the different turbulence models may provide different outcomes on the turbulence models [19, 42, 43]. In a study by Maele and Merci, [43], simulations were performed on a buoyant plume, were SKE and Realizable was used. Their goal was to test the

effect of modifying the turbulence production due to buoyancy on different turbulence models. They found that both models performed better, but the enhancement in Realizable was greater than for SKE. Consequently, it might be that the interaction between Realizable and the sub-grid model was incorrect, while the interaction for SKE and RNG was correct.

In order to test the sub-grid's contribution effect on the turbulence models, further simulations where the sub-grid modelling was removed, was conducted. The tests consisted of four simulations, two with SKE and two with Realizable. For both models, one simulation was run with sub-grid objects, and the other where the sub-grid objects had been removed. The tests showed that removing the objects on the floor had a significant effect on the TKE values. By not including the sub-grid objects, the TKE values for SKE were reduced, whereas the TKE values for Realizable were enhanced. A possible reason for this might be that the realizable condition was violated at the sub-grid objects. As the flow impinges on the objects, a separation is created that might have been non-realizable. Further it is possible that this violation reduced the velocity such that the turbulence production by the sub-grid model was very small for Realizable contradictory to SKE. This could, in turn, explain the difference in TKE. Thus, SKE (and RNG) may have violated the realizable condition. As the condition was not violated for Realizable, the velocity was reduced, which affects the contribution of sub-grid modelling on turbulence production. Thus, it is possible that Realizable reduced the sub-grid contribution where it was not supposed too. This could also explain why Realizable showed equal TKE values to SKE and RNG inside the plume. As the flow had lower velocity inside the plume, the realizable condition was not violated. Therefore, Realizable did not reduce the velocity, and the sub-grid model's contribution was about equal for all the turbulence models. However, outside of the plume, the grid is mostly built up of the stretched grid, thus much of the roughness elements will be porous. Consequently, there might not be much physical impingement or physical flow separation, and perhaps the realizable condition did not get violated. However, the sub-grid model will create a blockade of the flow at the sub-grid object, and the behaviour of the flow should be similar. As experimental data on turbulence was lacking, it was hard to know which turbulence model predicted the right TKE behaviour outside of the plume.

Nonetheless, it is possible that this difference might be an explanation for why Realizable predicted higher concentration values and concentration fluctuations, compared to the other models. As a high TKE increases mixing, leading to lower concentration levels inside the plume, a low TKE would

lead to higher concentration. Additionally, a low TKE would indicate that density forces would be stronger, and thus more likely to have concentration fluctuations. However, the difference in TKE levels between SKE and RNG was similar to the difference between SKE and Realizable. One would therefore expect the same difference in concentration levels between SKE and RNG as between SKE and Realizable. In spite of this, there were no large concentration difference between SKE and RNG, and SKE did not show any more concentration fluctuations than RNG. Therefore, it is possible that the Realizable model interacts better with density effects, and is able to predict important characteristics of it. Whereas, SKE and RNG was not able to include the density effects, such as concentration fluctuations.

Based on the concentration data, Realizable was considered the better model of the three. The unexpected TKE values outside of the plume created some uncertainty as to whether Realizable's results were reasonable. However, as experimental data on turbulence behaviour was lacking, it was not possible to identify how the TKE should have behaved outside the plume. Realizable was therefore seen as the best fit for this case.

4.2 Case 2: Low momentum neutral gas dispersion in urban environment

Here an experiment performed on a wind tunnel designed by the University of Hamburg was used for RANS model validation. The experiment consisted of a wind tunnel with a box at its centre. The wind in the tunnel was turbulent, blew downwards and impinged on the box. On the lee side of the box there was a continuous leak of gas. The impinging air mixed with the gas, and the mixture continued downwards. This experimental setup represents a simple urban geometry, where the geometry was resolved by the grid.

4.2.1 Experimental case

The wind tunnel used in this experiment was designed to recreate dispersion scenarios under various wind conditions [44]. The wind-blowing fan and tunnel was built such as to provide a wind that was uniform and undisturbed [44]. In the centre of the tunnel a box was placed with dimension 0.8L in length, 1.2L width and 1L height, respectively. L was the characteristic length for this experiment, equal to the height of the box (L=0.125m). The tunnel was 128L in length, 12L width and 8L in height, respectively. The floor of the tunnel was a smooth surface. An overview of the tunnel and box with dimensions can be seen in figure 4.10. For a complete description about

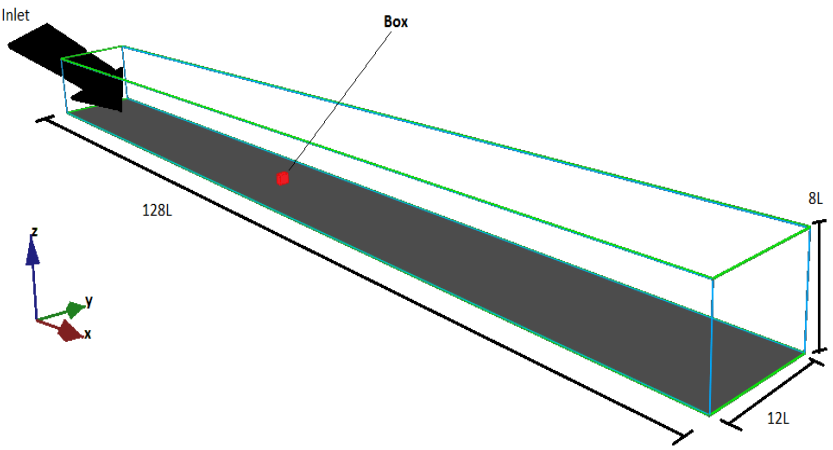

(a) Wind tunnel with dimensions.

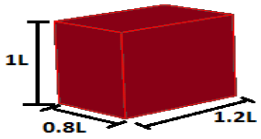

(b) Box in the tunnel with dimensions.

Figure 4.10: Wind tunnel.

the wind tunnel see Schatzmann, Marotzke and Donat [44].

The wind blew in positive X direction and was assumed to be air at standard conditions. The dispersed gas was a neutral tracer gas, that was released through 4 leaks at the lee side of the box, each with an area of 1.15 cm^2. The leaks had exhaust velocity of approximately 0.033 m/s. The downward blowing wind impinged on the box and was driven around it. As the wind moved around the box, a recirculation zone was created on the lee side of the box. The recirculation zone on the lee side of the box, dispersed the gas. The Reynolds number of the wind, with U_{ref} = 5.6 m/s and L, was around 38 000. The Reynolds number of the gas, using the exhaust velocity and the length of the source elements as the characteristic length, was around 150. This gives that the experiment was modelling a fully developed turbulent wind that mixed with a laminar gas release. Because it was a continuous gas release with a stable wind, the air-gas mixture reached a steady state after approximately 4-8 seconds. Hereafter for this case, the side where the wind impinges on the box will be referred to as the windward side. The opposite side will be referred to as the lee side. The two last sides will be referred to as the alongsides.

In the experiment more than 1200 measure probes were placed, at different X, Y and Z positions. The majority of the probes was placed at two heights, either z=0.08L or z=0.28L. The greater number of the probes measured concentration and a few measured velocity, shear and turbulence. All of the probes was placed at the negative Y-axis (the box's centre at zero X and Y), because of this, all values that are later exhibit on the positive Y-axis were mirrored. Information about the accuracy of the measurements was given, and can be seen in table 4.6. The probes that measured velocity were used to determine wind profile. The probes that measured concentration were used to determine the models behaviour and accuracy of recreating the experiment. The probes that measured shear and turbulence were not used, as they were so few and placed before the leak. Even though not stated explicitly it was believed that all experimental measurements were taken at a steady-state.

Table 4.6: Overview of the accuracy in the experiment

Measured value	accuracy $\pm$	unit
Velocity/U_{ref}	5.4×10^{-3}	
Concentration	2×10^{-6}	[0,1]
x/L-position	1.6×10^{-3}	[L]
y/L-position	1.6×10^{-3}	[L]
z/L-position	0.4×10^{-3}	[L]

4.2.2 Simulation setup

The geometry of the experiment was constructed in FLACS according to specification provided from the article and report concerning the experiment, Schatzmann, Marotzke and Donat [44, 45]. The simulation volume, with its centre at the box's centre, was x: -8L to 8L, y: -6L to 6L and z: 0L to 8L. This volume was chosen such that walls, floor and roof effects were included. The simulation volume was divided into a core domain and a stretched domain. The core domain centred around the box and for all tests was x:-1.2L to 1.2L, y:-1.8L to 1.8L and z:0L to 1.6L. Outside the core domain the stretched domain started and continued until end of simulation volume. The core domain consisted of a constant grid cell size. The stretched grid consisted of grid cells that increased in size. Outflow boundary condition was defined as nozzle, and at the lower boundaries for x and higher boundaries for z the boundary conditions was defined as wind. Solid walls and lateral boundaries

corresponds to no-slip boundary[4]. To achieve a neutral gas dispersion, 1% propane was used as a tracer leak. Initial conditions about temperature, pressure, relative turbulence, etc. was not documented and was assumed to be at standard conditions. A reference height ($z_{ref} = 5.28L$), reference velocity ($U_{ref} = 5.6m/s$) and velocity measurements (before the box) was used to correctly simulate the wind. Further in the description of this case, unless stated differently, L and U_{ref}, as defined, were used as the characteristic length and velocity.

In the simulations, MPs were defined for every measurement probes' placement. The MPs monitored the same quantities as the experiment as well as: k, ϵ and velocity. As the MPs were placed equally in the simulation and experiment, direct comparison of experimental and simulation data for the concentration was performed. The wind was given a build up time of 4 seconds before gas was released. The simulations ran for time iteration summing up to 16 seconds in total. For this case the gas quickly reached a steady state after it was released, approximately 4 seconds.

The flow chart in figure 4.11 represents all the simulations that were performed and relevant setups. As a first step preliminary tests were done in the following order: first, a geometry simulation was performed to control that the geometry was satisfactory. Second, a wind simulation was conducted. Finally, a grid sensitivity and initial condition tests was performed. Based on the preliminary tests the fine grid was chosen, and the turbulence model tests were performed based on this. The process, and the choices made will be presented in greater detail below.

An overview of the result from the wind profile test can be seen in figure 4.12. In figure 4.12, the horizontal axis represents a normalised height, the vertical axis represents a normalised velocity. Only one wind simulation was needed as that wind profile was very satisfactory.

Table 4.7 shows an overview of the different grid sensitivity and initial testing. Here it may be seen that the fine grid and very fine grid have the same Δi_{min}, but not N_i. Having equal Δi_{min}, but not N_i, implies that the number of grid cells, especially the number of Δi_{min}, has increased inside the simulation volume from fine to very fine grid.

Table 4.8 provide a quantitative comparison of the performances of the grid

[4]For more information about boundary conditions in FLACS see section 2.3

Table 4.7: Test name along with a short description, number of grid points in the grid, N_i, and minimum grid dimension in the grid, Δi_{min} for the remaining preliminary tests.

Type of test	Description	Number of grid cells	Minimum grid dimension [m]
Coarse grid$_1$	This is a coarse grid	Nx - 72 Ny - 72 Nz - 51	$\Delta X_{min} - 0.01$ $\Delta Y_{min} - 0.005$ $\Delta Z_{min} - 0.0025$
Coarse grid$_2$	This is a coarse grid, as coarse grid$_1$, but here the relative turbulent intensity and turbulence length scale is doubled	Nx - 72 Ny - 72 Nz - 51	$\Delta X_{min} - 0.01$ $\Delta Y_{min} - 0.005$ $\Delta Z_{min} - 0.0025$
Fine grid	This is a finer grid than the coarser grid, in all directions	Nx - 92 Ny - 118 Nz - 61	$\Delta X_{min} - 0.005$ $\Delta Y_{min} - 0.005$ $\Delta Z_{min} - 0.0025$
Very fine grid	This is same as fine grid, but the amount of grid cells in x-direction has increased	Nx - 137 Ny - 118 Nz - 61	$\Delta X_{min} - 0.005$ $\Delta Y_{min} - 0.005$ $\Delta Z_{min} - 0.0025$

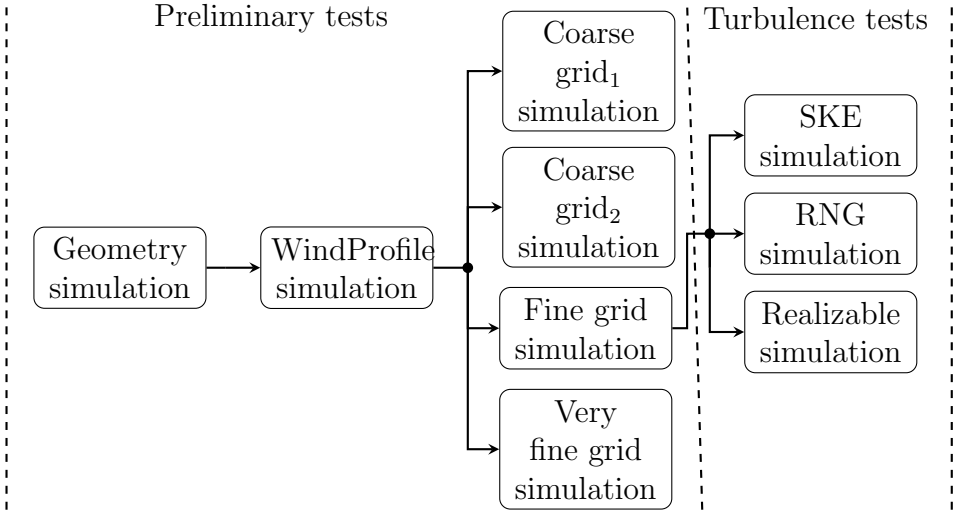

Figure 4.11: Flow chart, presenting in which order the simulations were performed.

sensitivity and initial condition testing. It is given in %, the amount of MPs concentration values that were inside the interval: "experimental values ± accuracy". This table provides a direct comparison of the simulations ability to correctly predict concentration values for all MP' positions. From this table alone it was seen that the fine grid was the better solution and a further grid resolution was not necessary. Also seen is that there seems to be no difference in changing relative turbulence intensity or turbulence length in the leak.

Table 4.8: The % of simulation value that is in the interval "experimental values ± accuracy", for all MPs.

	0.08L [%]	0.28L [%]
Coarse $grid_1$	37.58	39.16
Coarse $grid_2$	37.58	39.16
Fine grid	54.04	57.47
Very fine grid	49.38	55.49

The graphs of figure 4.13 provides a visual overview of the results of the grid sensitivity and initial condition tests, along with the experimental result. All graphs are XY-planes, at z=0.28L, with concentration in the vertical direction. Even though differences are observed, the overall trend is that the

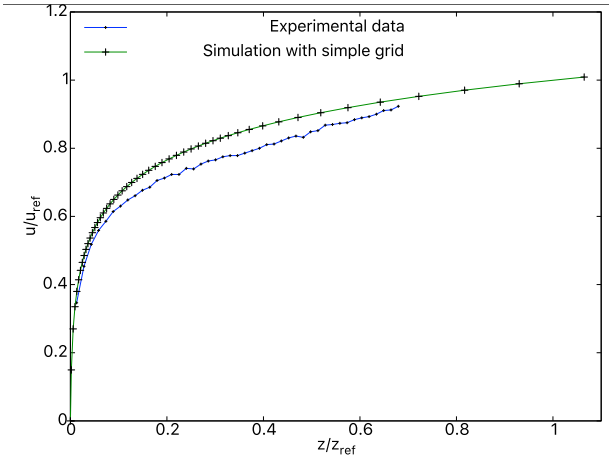

Figure 4.12: Experimental and simulation wind profile.

different grids and initial condition gave similar results. It is seen that the same patterns are at the same positions for experiment and simulations, this was also seen for other heights. Noticeable, is that the fine and very fine grids concentration peak was lower than the experiment. Both of these grids predicted only about 3×10^{-5}, while the experiments had a value at about 4.5×10^{-5}. For the coarse grid$_1$ and coarse grid$_2$ the concentration peaks was about equal as for the experiment. The difference in how the coarse grid$_1$ and coarse grid$_2$ predicted highest concentration values contrary to the prediction of fine and very fine grids, seems to indicate that coarse grid$_1$ and coarse grid$_2$ do a better job at predicting concentration peaks, but according to table 4.8, the fine and very fine grid do a better job at predicting concentration better overall. Also noticeable, is that the fine grid predict a higher % for both heights, compared to the other grids. Consequently, the fine grid was chosen to do turbulence test with.

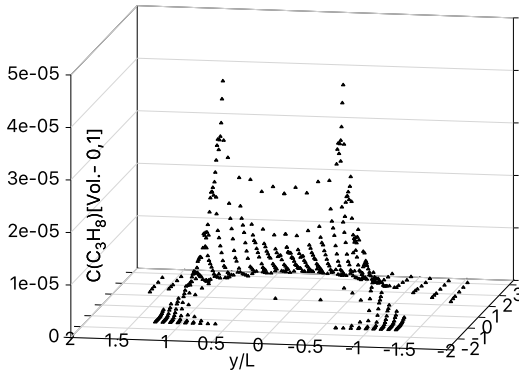

(a) Experimental

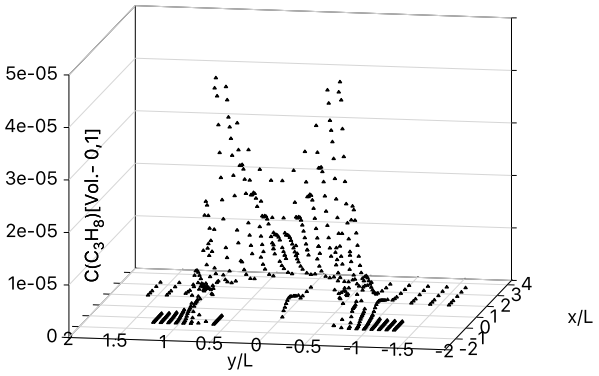

(b) Coarse Grid$_1$

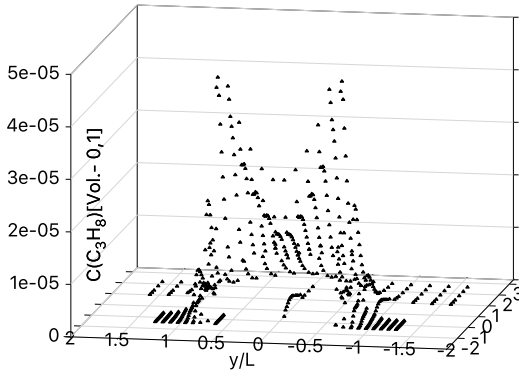

(c) Coarse Grid$_2$

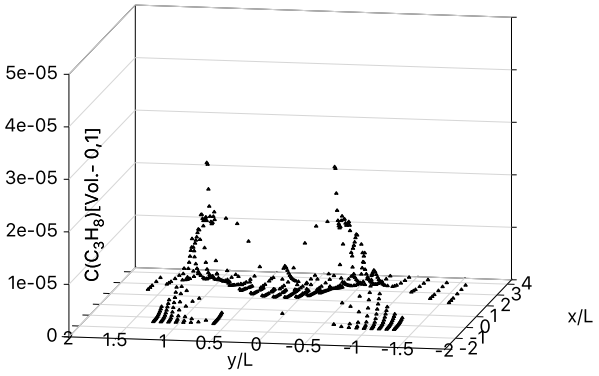

(d) Fine grid

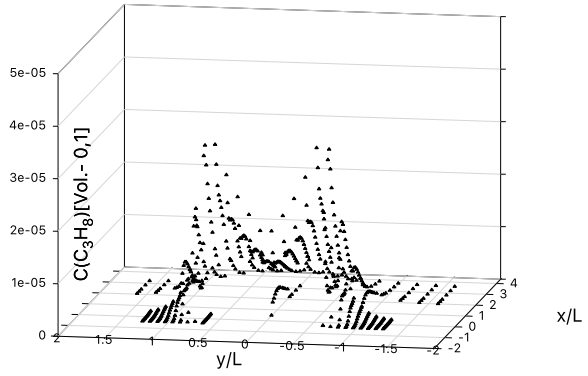

(e) Very fine grid

Figure 4.13: Concentration of the preliminary tests at z=0.28L.

4.2.3 Results

Table 4.9 provides clock time used for the different models. Here it was concerned that SKE and RNG have about the same simulation run time, while Realizable used about 21-27 hours longer for simulation. The time differences was believed to be significant as to affect the choice of turbulence model.

Table 4.10 shows the % of how many of the MP concentration values that was inside the interval "experimental values ± accuracy". In this table it is seen that Realizable enhanced the % for Z=0.08L, but for Z=0.28 the % was slightly reduced, compared with SKE. For RNG it is seen that the % is enhanced for Z=0.08L by 4%, but for Z=0.28 the % was reduced with about 8%, compared with SKE. Therefore, based on table 4.10 and time used, SKE was the preferred model for this case study.

Table 4.9: Clock time used for simulation with the different models.

Model	SKE	RNG	Realizable
Time[hour]	303.35	308.93	329.45

Table 4.10: The % of simulation value that was in the interval "experimental values ± accuracy", for all MP.

	0.08L [%]	0.28L [%]
SKE	54.04	57.47
RNG	58.39	49.30
Realizable	55.59	55.49

Figure 4.14 and 4.15 provides a visualisation of the results of the models and experimental results. When comparing the simulation results with the experimental values in the graphs some general trends are observed. Firstly, in general, the results from the simulations are in moderate good agreement with the experimental results. Secondly, the simulated dispersion seemed more equal to the experimental dispersion at z=0.28L than for z=0.08L. Thirdly, in spite of visually being in good agreement, quantitively, the best model predicted only correctly at about 55% for both heights. Next, all the models gave lower than experimental measurements for x>0 and -1L<y<1L, which is in the wake region of the flow. This also seemed to predict a too

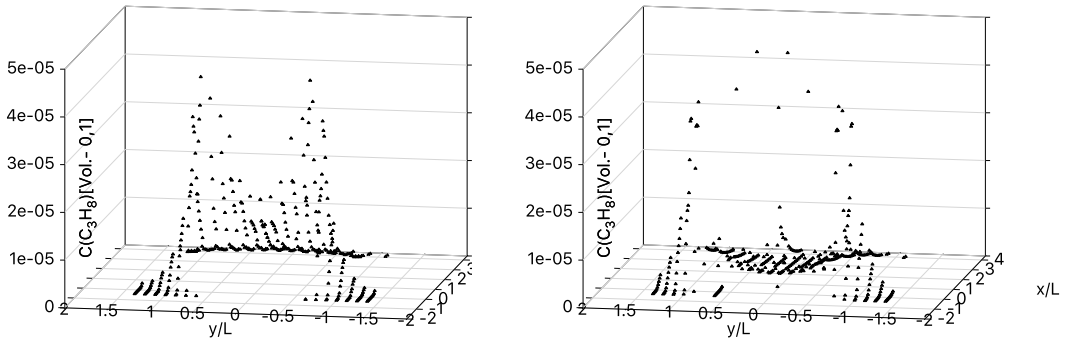

(a) Experiment

(b) SKE

(c) RNG

(d) Realizable

Figure 4.14: Concentration of the turbulence tests at z=0.08L.

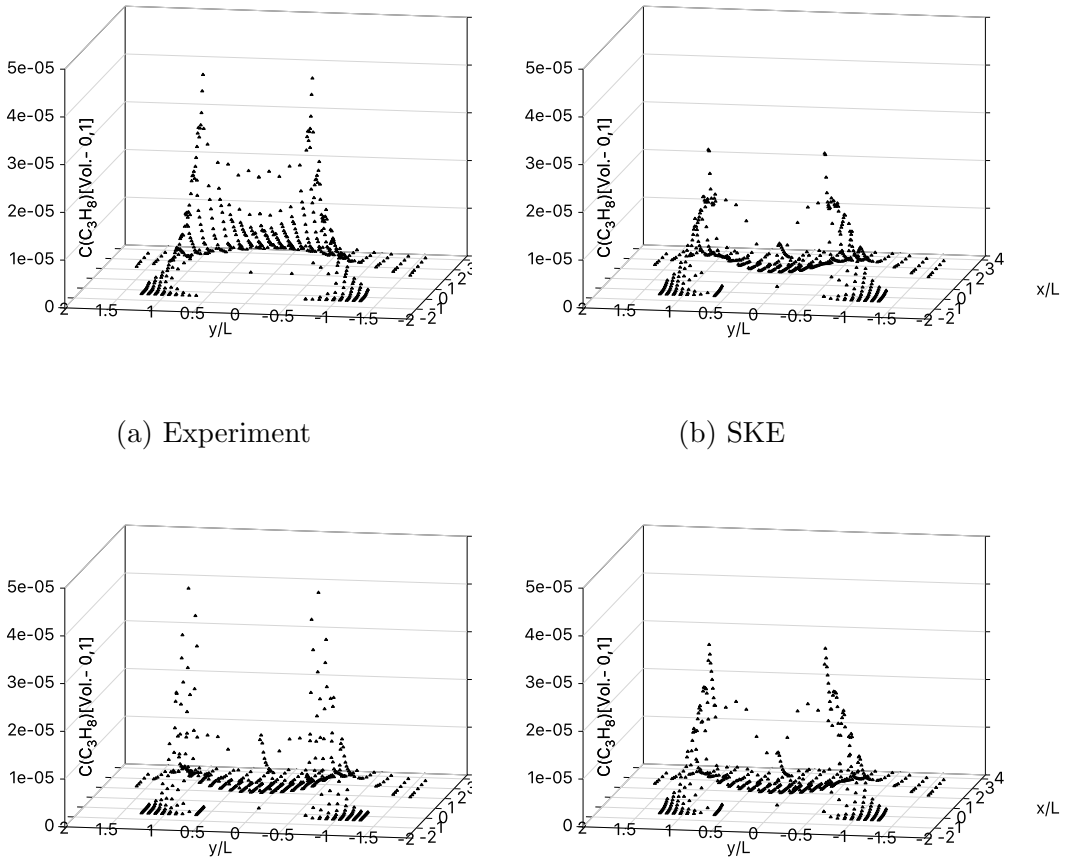

(a) Experiment

(b) SKE

(c) RNG

(d) Realizable

Figure 4.15: Concentration of the turbulence tests at z=0.28L.

steep concentration drop from the maximum concentration peak to the middle of the lee side of the box, which all models show.

Another trend was that the concentration on the sides of the box was, in some degree, recreated by the models SKE and Realizable, but not by RNG. The dispersed gas on the sides of the box is highlighted in figure 4.16. Figure 4.16 shows the concentration along the vertical wall of the box, on the negative side, at z=0.28L. In figure 4.16 concentration is represented along the vertical axis and the horizontal axis is x/L. Here, it is clear that the models behaved very differently on the lee side of the box. RNG predicted a low concentration on the alongside, barely visible, but the concentration quickly increased close to the corner of the along- and lee side. SKE and Realizable seemed to predict the same concentration trend, with a more equal concentration value to experiment than RNG. The drawback of the results from SKE and Realizable, was that while the experimental value increased, the concentration value of SKE and Realizable decreased close to the corner of the along and lee side.

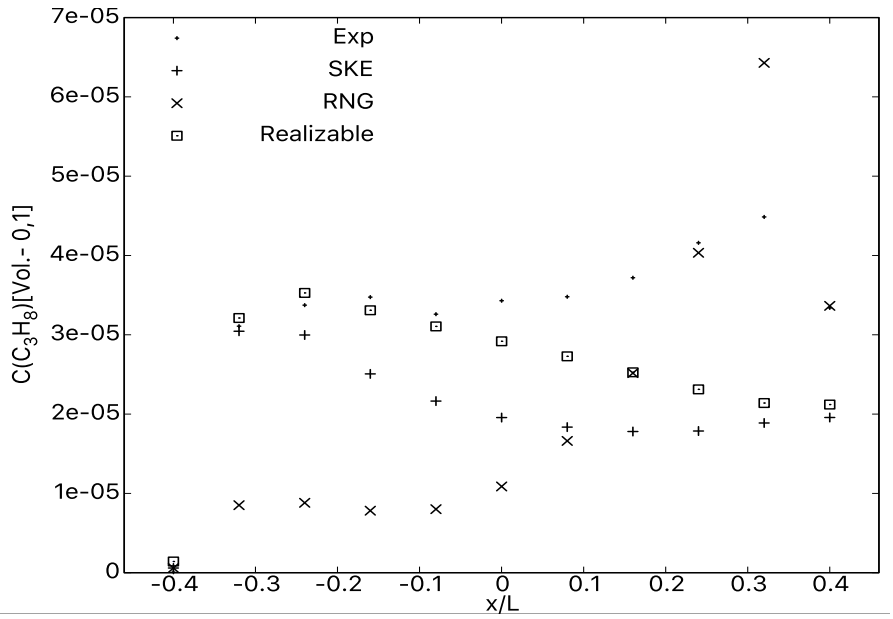

Figure 4.16: Concentration at the negative y side of the box at z=0.28L.

Table 4.11 shows the X, Y and Z coordinates for the maximum concentration and its value. From this table it was seen that the coordinates of where the maximum concentration takes place was the same for the experiment and RNG for both heights, but not for SKE and Realizable. Close to the

ground SKE and Realizable predicted the placement correctly, but further away from the floor the prediction of the placement was not correct. Also concerned was that close to the floor all models predicted a too high maximum concentration value. Further away from the floor SKE and Realizable predicts a too low maximum value, while RNG still overpredicts.

Table 4.11: Overview of placement of maximum concentration and its value.

	Z = 0.28L			Z = 0.08L		
	X [L]	Y [L]	$C_{max} \times 10^{-5}$ [0,1]	X [L]	Y [L]	$C_{max} \times 10^{-4}$ [0,1]
Experiment	0.32	-0.64	4.49	0.4	-0.64	1.47
SKE	-0.32	-0.64	3.04	0.4	-0.64	2.33
RNG	0.32	-0.64	6.43	0.4	-0.64	2.30
Realizable	-0.24	-0.64	3.53	0.4	-0.64	1.98

4.2.4 Discussion

The purpose of this simulation case was to examine which of the turbulence models, SKE, RNG or Realizable, would best predict a neutral low momentum dispersion in an urban environment. The following findings will be discussed: (1) SKE gave the most accurate results according to the experimental values, (2) even though RNG did not predict the flow field accurately inside the measured area, it may be a better suited model for predicting dispersion outside the measured area in this case.

All models were stable and predicted reasonably good results. In computational time, SKE and RNG operated inside the same time range (± 2.5 hours), while Realizable used a significantly longer duration (+20 hours). As Realizable's results did not significantly increase in accuracy in accordance with the longer run time, the model was not seen as a good fit for this case. As SKE showed a more accurate dispersion according to the experiment, than RNG, it was considered the best suited turbulence model for this case.

In spite of SKE producing good results for the dispersion scenarios, it was not able to predict where the maximum concentration took place at the higher z position. RNG, on the other hand, was able to correctly predict the position of the maximum concentration at both heights. Tominaga and Stahopoluos, [2], reported similar findings in their study on numerical simulations of dispersion, around an isolated cubic building. In their study, they found that

RNG was the only model capable of reconstructing the flow field satisfactory, and that SKE was not able to recreate the flow field on the roof. This implies that SKE might be the better fit of the measured data, but that RNG might be a better fit if there had been measurements on the roof of the box.

Also reported in the study by Tominaga and Stahopoluos, [2], was that on the lee side of the box, in the wake, the reconstruction of all models was poor. This was also found for this case. From the concentration graphs here it seemed as none of the models were fully capable of reconstructing the experimental dispersion in the wake region. Tominaga and Stahopoluos believed it was a poor reconstruction of vortex shedding behind the cube that hindered a correct prediction of concentration at the wake. This might also be applicable for this case.

Even though RNG was not able to fully recreate the flow pattern, as it did not properly predict the concentrations on the alongside of the box. Both SKE and Realizable showed recirculating flows at all heights, whereas, RNG only exhibited recirculating flows at a higher height. In other words: Further away from the floor, RNG started to provide similar concentration levels to the experimental values. A possible explanation for this might be that RNG predicted a too weak flow field, that hindered a recirculating flow on the alongside of the box. It is believed that the boundary layer, produced by the floor, weakened the flow field. As the gas was elevated, the influence of the boundary layer was decreased, and a recirculating flow was able to form. As a consequence, the gas became dispersed further up on the alongside of the box. However, as there were no concentration measurements further away from the floor, it was not possible to examine whether RNG predicted the correct dispersion according to the experiment at a higher level.

Because RNG seemed to predict a recirculating flow farther from the floor and was able to properly predict the placement of the maximum concentration, it is possible that RNG might be a better fit than SKE. This is supported in previous studies on neutral dispersion, where both RNG and Realizable have been found to be capable of reproducing the wind field, while SKE fails, especially in wake regions and with increased height [14, 39]. It is therefore possible that if there had been measurements higher up, SKE would have provided poorer results. Nonetheless, based on the available measurements in this study case, SKE was the best-suited model.

4.3 Case 3: Hydrogen jet impinging on a surface

In this case an experiment of a buoyant jet impinging on a surface, was used for RANS model validation. Two different experimental setups was used where, both were squared surfaces, one with no walls the other with walls on all sides (an open box). Also used, was two different jets, one low momentum the other high momentum. Because there are few comparative studies of turbulence models on buoyant jets and as buoyant releases are rather common in safety and environmental impact studies, this case was chosen as an interesting simulation case from an application point of view.

4.3.1 Experimental case

The experiment under study consisted of a high-pressure gas system, that provided a continuous hydrogen release through a nozzle which, in turn impinged on a surface. A geometrical representation of the setup and the two different surfaces can be seen in figure 4.17. The geometry on the left was the simpler geometry of the two, only a nozzle and a square plate, hereby referred to as the simple geometry. The geometry on the right of figure 4.17 was the more complex geometry of the two, a nozzle and a square plate with walls on all sides, hereby referred to as the complex geometry. The jet was oriented in positive Z-direction. There was no wind in the experiment, thus it was a pure buoyant jet release. For more details about the experiment see Friedrich and colleagues [46].

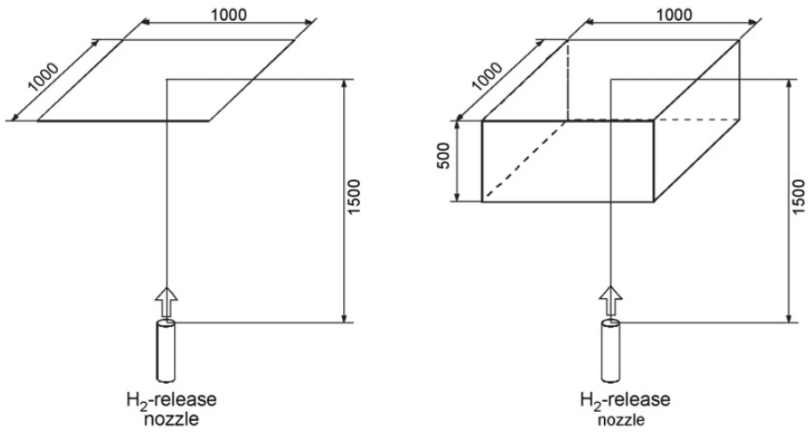

Figure 4.17: The geometrical setup under study, all numbers are given in [mm], extracted from [46].

From this report, [46], three experiments were chosen for model validation. Two experiments used the simple geometry: one with a low momentum and large nozzle (PIA), the other a high momentum and small nozzle (PIE). The last experiment concerns the complex geometry and was a high momentum and small nozzle (PIE). Thus, PIE was used for both for the complex and simple geometry, while PIA was only used for the simple geometry. An overview of nozzle size, exhaust rate, naming and geometrical setup for the three experiments used can be seen in table 4.12.

Table 4.12: Overview of experiment that were simulated

Name	Nozzle Diameter [mm]	Exhaust rate [g/s]	Geometry simple/complex
PIE	21	3	Simple
PIA	100	0.14	Simple
PIE	21	3	Complex

The Reynolds number calculated with the nozzle diameter as the characteristic length and the exhaust velocity as the characteristic speed, was about 200 for PIA and about 21 000 for PIE. In the article by R. Viskanta, a Reynolds number for an impinging jet based on the nozzle diameter greater than 3000 identifies a fully turbulent jet [47]. This implies that PIE was a fully turbulent jet at the release, while PIA was, according to the article by R. Viskanta, a laminar jet at the release [47]. In spite of this, because of buoyancy effects, PIA was turbulent before impingement. This is known by using the Grashof number, a Grashof number greater than 3×10^8 for a buoyant jet will be turbulent. The Grashof number for PIA was about 1.56×10^{12}, thus the jet released in PIA was turbulent before impingement. The densimetric Froude number was about 1.4×10^{-4} for PIA, and about 6.6×10^{-3} for PIE. Consequently, both PIE and PIA were turbulent and influenced by buoyancy, but buoyancy played a large role for PIA than for PIE. Both PIE and PIA was seen as jet releases, in the general sense of releases with initial momentum > 0.

In the experiment only concentrations were measured. The concentrations were measured with probes where no accuracy was provided. For the simple geometry they were placed both along the vertical direction and across the release (y direction) at elevation z=38.1d in PIE and z=2.5d in PIA. In the complex geometry there were two arrays of concentration sensors in the Y

direction, at Z = 5d and 5.95d.

Measurements were taken just before the release was terminated, which was after 10g of hydrogen had been released for all experiments [46]. This implies that a steady-state may or may not have been reached at termination. Also provided from the experiment was Schlieren-photographs, taken at certain time intervals. The Schlieren-photos were used to give a general visualisation of simulation and experiment, while the concentration measurements were used to give a better, more detailed, visualisation, and to characterise the models individual behaviour.

4.3.2 Simulation setup

The geometry of the experiment was constructed in FLACS according to specifications provided from the report [46]. The simulation volume was, with the nozzle at origin, x:-1.5m to 1.5m, y:-1.5m to 1.5m and z:-0.1m to 2m. The simulation volume was divided into a core domain and a stretched domain. The core domain was from, x:-0.8m to 0.8m, y:-0.8m to 0.8m and z:0m to 1.5m. Outside the core domain the stretched domain started and continued until end of the simulation volume. The core domain consisted of a constant grid cell size and the stretched grid was built up of grid cells increasing in size. A refined mesh was used at the outlet of the nozzle. Boundary conditions were defined as Nozzle for all of the simulation domain[5]. Initial conditions about temperature, pressure, relative turbulence, etc. was not documented. Since this was a release from a high-pressure container it was initially believed that information about temperature would be necessary for the simulation. It was however found, that the pressure in the tank was low enough such that transition from stagnation in the tank to ambient was not characterised by any large change in temperature. In addition the gas flowed through a piping system before being released in the testing room. The different nozzle sizes and exhaust velocity, for PIE and PIA was used as the characteristic length and reference velocity of the release.

In the experimental report it was stated that the leak was stopped after 10g of hydrogen had been released, and they provided a time for this. This time was used for both PIE and PIA, in such a fashion that when the time iteration summed up to the end of release duration, the simulations stopped. The PIE simulation ran for a sum of time iteration up to 3.23 second. The PIA simulations ran for a sum of time iteration up to 71.3 seconds. In the ex-

[5]For more information about FLACS boundary conditions see section 2.3

periment, based on Schlieren pictures, PIA seemed to have reached a steady state at the end of release duration time, while PIE do not seem to have reached a steady state. MPs were defined at every measurement probes' placement were they measured the same quantities as in the experiment. The MPs were used for a direct comparison of experimental and simulation data.

The flow chart in figure 4.18 represents all the simulations performed and the sequence in which they were executed. As a first step Preliminary tests was done in the following order: Firstly, 3 simulations to control the geometry of PIA, PIE simple geometry and PIE complex geometry was run. Secondly, 3 simulations was run for PIE simple geometry only, where initial conditions for PIE simple grid was changed. It was believed that if there were no, or little difference between these three different initial conditions for PIE simple grid, the result would apply to PIA and PIE complex geometry as well. Thirdly 9 simulations were run, 3 simulation on PIA, 3 simulations on PIE simple geometry, and 3 simulations on PIE complex geometry. These 9 simulations provided a grid sensitivity test. Based on the preliminary tests the simplest of the grids for PIA, PIE (both geometries) was chosen and turbulence tests were performed based on this. The process, and the choices made will be presented in greater detail below.

Table 4.13 presents a description of all the preliminary tests. The test on initial conditions represents changes in relative turbulence intensity (RTI), turbulence length scale (TLS) and temperature of the leak. The grid sensitivity tests was performed with 3 different grids all simulated on PIA and PIE (both geometries). The three grid sensitivity tests used a simple grid, a simple grid with an increase in N_i for all i, and a further increase in N_Z.

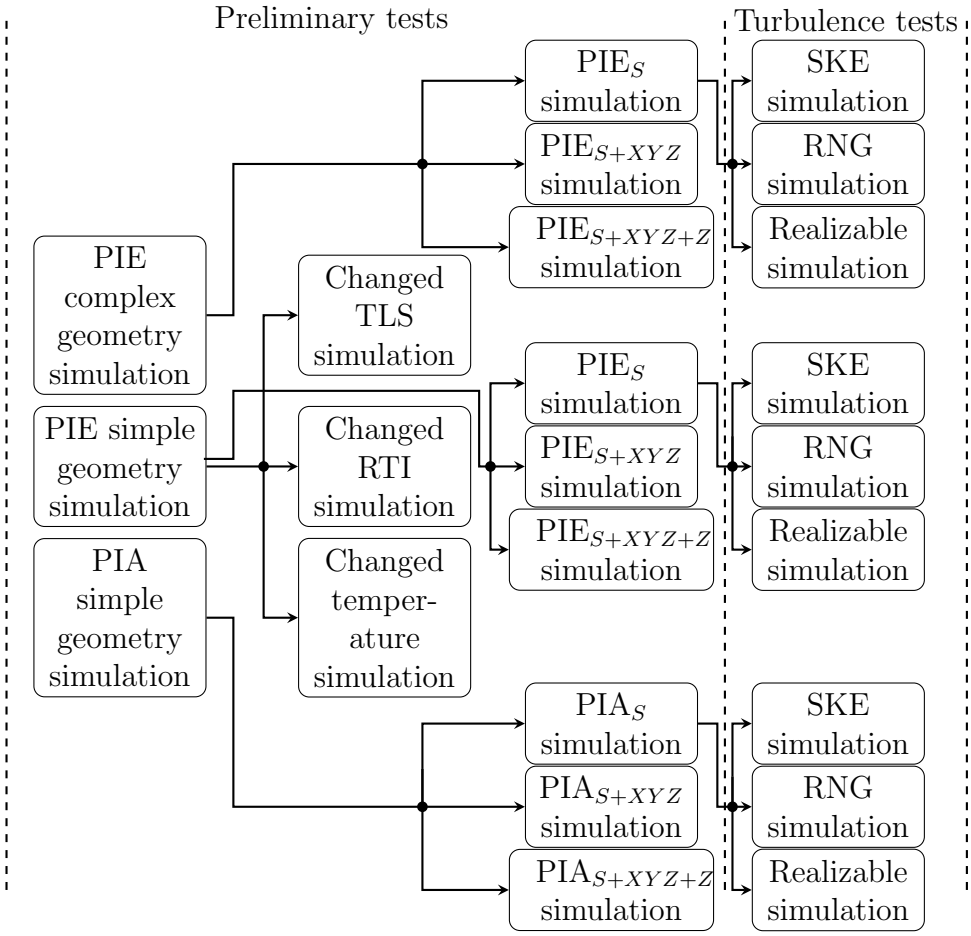

Figure 4.18: Flow chart, presenting in which order the simulations were performed.

Table 4.13: Test name along with a short description, number of grid points in the grid, N_i, and minimum grid dimension in the grid, Δi_{min} for the remaining preliminary tests.

Type of test	Description	Number of grid cells	Minimum grid dimension [m]	S/C geometry
PIE_S	The $_S$ implying the simplest of the three geometry	Nx - 75 Ny - 77 Nz - 45	$\Delta X_{min} - 0.03$ $\Delta Y_{min} - 0.03$ $\Delta Z_{min} - 0.03$	S
$PIE_{S,RTI}$	Decrease RTI (from 0.15 to 0.05)	Nx - 75 Ny - 77 Nz - 45	$\Delta X_{min} - 0.03$ $\Delta Y_{min} - 0.03$ $\Delta Z_{min} - 0.03$	S
$PIE_{S,TLS}$	Decrease TLS (from 0.011 to 0.003 m)	Nx - 75 Ny - 77 Nz - 45	$\Delta X_{min} - 0.03$ $\Delta Y_{min} - 0.03$ $\Delta Z_{min} - 0.03$	S
$PIE_{S,T}$	Decrease *Temperature* of the leak (from 20 to 10 degree Celsius)	Nx - 75 Ny - 77 Nz - 45	$\Delta X_{min} - 0.03$ $\Delta Y_{min} - 0.03$ $\Delta Z_{min} - 0.03$	S
PIE_{S+XYZ}	$_{+XYZ}$ indicates an increase in N_i for all i	Nx - 100 Ny - 100 Nz - 67	$\Delta X_{min} - 0.025$ $\Delta Y_{min} - 0.025$ $\Delta Z_{min} - 0.025$	S
$PIE_{S+XYZ+Z}$	$_{+XYZ+Z}$ indicates a further increase for N_z	Nx - 103 Ny - 103 Nz - 79	$\Delta X_{min} - 0.025$ $\Delta Y_{min} - 0.025$ $\Delta Z_{min} - 0.025$	S
PIA_S	The $_S$ implying the simplest of the three geometry	Nx - 65 Ny - 63 Nz - 48	$\Delta X_{min} - 0.03$ $\Delta Y_{min} - 0.03$ $\Delta Z_{min} - 0.03$	S
PIA_{S+XYZ}	$_{+XYZ}$ indicates an increase in N_i for all i	Nx - 87 Ny - 87 Nz - 67	$\Delta X_{min} - 0.025$ $\Delta Y_{min} - 0.025$ $\Delta Z_{min} - 0.025$	S
$PIA_{S+XYZ+Z}$	$_{+XYZ+Z}$ indicates a further increase for N_z	Nx - 85 Ny - 86 Nz - 79	$\Delta X_{min} - 0.025$ $\Delta Y_{min} - 0.025$ $\Delta Z_{min} - 0.025$	S
PIE_S	The $_S$ implying the simplest of the three geometry	Nx - 77 Ny - 77 Nz - 48	$\Delta X_{min} - 0.03$ $\Delta Y_{min} - 0.03$ $\Delta Z_{min} - 0.03$	C
PIE_{S+XYZ}	$_{+XYZ}$ indicates an increase in N_i for all i	Nx - 103 Ny - 103 Nz - 67	$\Delta X_{min} - 0.025$ $\Delta Y_{min} - 0.025$ $\Delta Z_{min} - 0.025$	C
$PIE_{S+XYZ+Z}$	$_{+XYZ+Z}$ indicates a further increase for N_zs	Nx - 103 Ny - 103 Nz - 79	$\Delta X_{min} - 0.025$ $\Delta Y_{min} - 0.025$ $\Delta Z_{min} - 0.025$	C

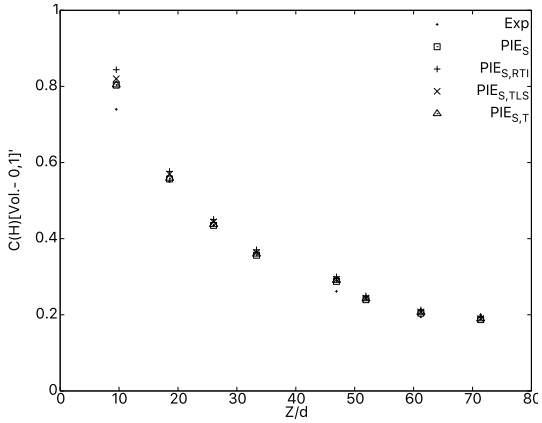

(a) Initial testing, with concentration in Z-direction.

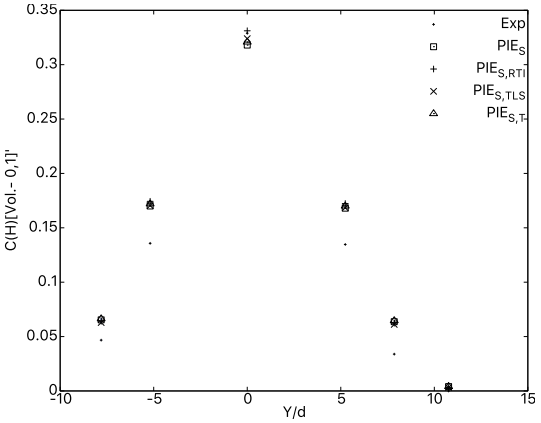

(b) Initial testing, with concentration in Y-direction

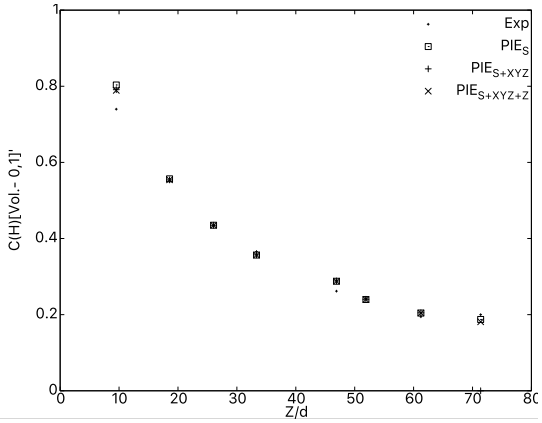

(c) Grid testing, with concentration in Z-direction.

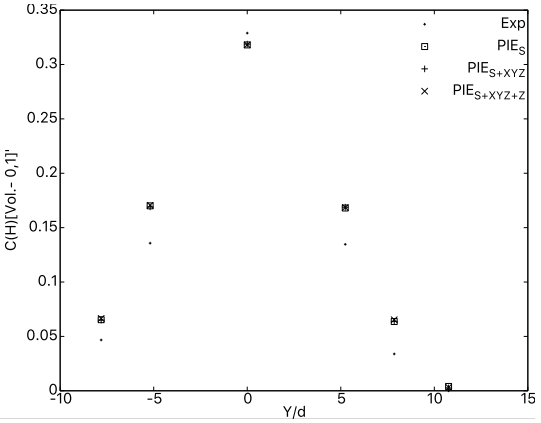

(d) Grid testing, with concentration in Y-direction.

Figure 4.19: Concentration from initial and grid sensitivity testing on PIE simple geometry.

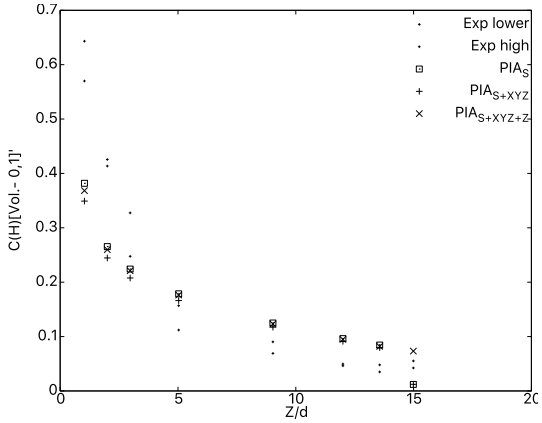

(a) Concentration in Z-direction for PIA for simple geometry.

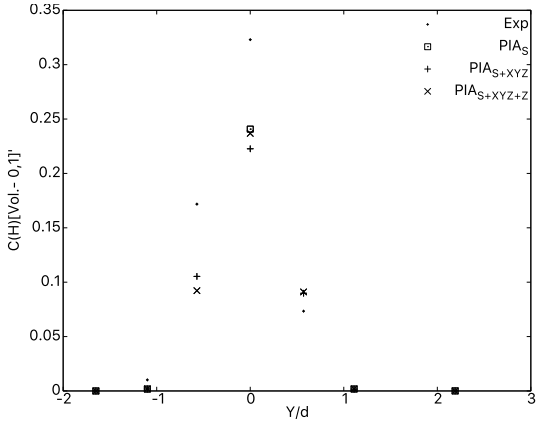

(b) Concentration in Y-direction for PIA for simple geometry.

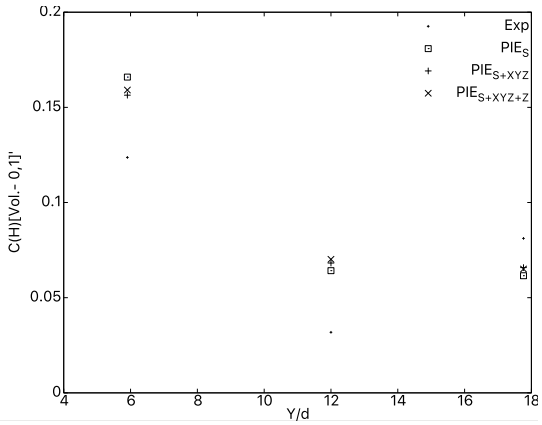

(c) Concentration in Y-direction for PIE for complex geometry, at z=5d.

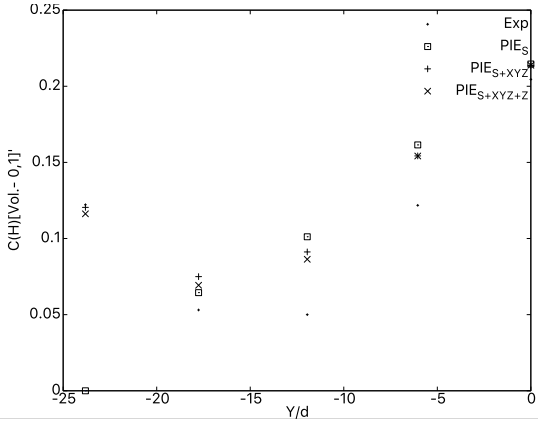

(d) Concentration in Y-direction for PIE for complex geometry, at z=5.95d.

Figure 4.20: Concentration from grid sensitivity testing on PIA and PIE complex geometry.

As can be seen in all graphs of figures 4.19 - 4.20 the general behaviour of the simulation was maintained, as well as the values were in general good agreement. For the initial tests graphs 4.19a and 4.19b show that there was a minimal effect of changing RTI, TLS or temperature of the leak. This lead to the conclusion that the initial conditions firstly chosen was in good agreement with the experiment, as well as no further testing of initial conditions seemed needed. In general there were no large difference for concentration values between the grids for PIA and PIE (both geometries). For PIA, PIE (both geometries) the grid PIA$_S$ and PIE$_S$ was chosen for further turbulence testing.

For PIA, on measurements in Z direction (graph 4.20a) two repetitions of the experiment were performed, providing two experimental data sets. In the graph 4.20a it can be seen that the simulation values were seldom inside these two experimental values. There seems to be no, to little difference in concentration values between the different grids, and in general, model - experiment agreement for PIA was lower than for PIE (both geometries).

For PIE on the complex geometry no information about the concentration in the Z direction was given. The simulation values seemed to be the diverging from the experimental values farther from the centre. There seems to be no, to little difference in concentration values between the grids.

4.3.3 Results

Table 4.14 show computational clock time used for all the models, for all the different simulated experiments. SKE stands out as the model that used almost half the run time compared to the other models.

Figure 4.21 shows a Schlieren picture of the experimental jet and 2D plots of the simulated jets, simulated with SKE, RNG and Realizable, for PIE simple Geometry. The measurement probes and their values of the experiment were marked in the Schlieren picture, and the MPs and their values were marked in the 2D plots. These figures were included to provide a concentration overview of experiment and simulations. The Schlieren picture was from the report, [46]. More detailed information about the values and placement of the measurement probes and MP is seen in figure 4.22. Figure 4.22 displays a normalised Y (figure 4.22b) or Z (figure 4.22a) in horizontal axis and concentration in the vertical axis. The 2D plots and Schlieren picture showed that SKE and RNG gave a good reconstruction of the experiment, while Realizable had a too wide spread of the jet. The wide spread predicted by Realizable seemed to be the reason for the much lower concentration values compared to SKE, RNG and Experiment. Based on these two figures, SKE reconstructed the jet most accurately, followed by RNG, while Realizable failed to capture the jets behaviour, for PIE simple geometry.

Figure 4.23 shows a Schlieren picture of the experimental jet along with 2D plots of the modelled jet, simulated with SKE, RNG and Realizable for PIE complex geometry. The Schlieren picture was from the report, [46]. In the PIE complex geometry, as for the PIE simple geometry, Realizable seemed to give a too wide spread, not reconstructing the jet dispersion as

Table 4.14: Clock time used for simulation with the different models.

	PIA, simple geometry, time [h]	PIE, simple geometry, time [h]	PIE, complex geometry, time [h]
SKE	65.9	15.6	23.7
RNG	122.5	24.3	41.6
Realizable	130.8	27.93	37.8

SKE and RNG seemed to do. Based on figure 4.23 it was apparent that Realizable simulated a dispersion with a too low centreline concentrations, while SKE seemed to be the better model, better reconstructing the dispersion. Concentration profiles at two different heights are displayed in figure 4.24. Here, a normalised Y placement is shown in the horizontal axis and concentration in the vertical axis. The graphs of figure 4.24 confirmed that Realizable simulated a dispersion with a too low centreline concentrations, and that SKE was the model best reconstructing the experimental dispersion, for PIE complex geometry.

Figure 4.25 shows a Schlieren picture of the experimental jet along with 2D plots of the modelled jet, simulated with SKE, RNG and Realizable for PIA simple geometry. The Schlieren picture was from the report, [46]. For PIA simple geometry all models seemed to reconstruct the experimental jet satisfactory. This was contrary to the performance of PIE (both geometries), where Realizable did not properly reconstruct the dispersion. More detailed information about the values and placement of the measurement probes and MP is seen in figure 4.26. Figure 4.26 displays a normalised Y (figure 4.26b) or Z (figure 4.26a) in horizontal axis and concentration in the vertical axis. Based on this figure, SKE recreated the experiment more closely, followed by RNG and lastly Realizable.

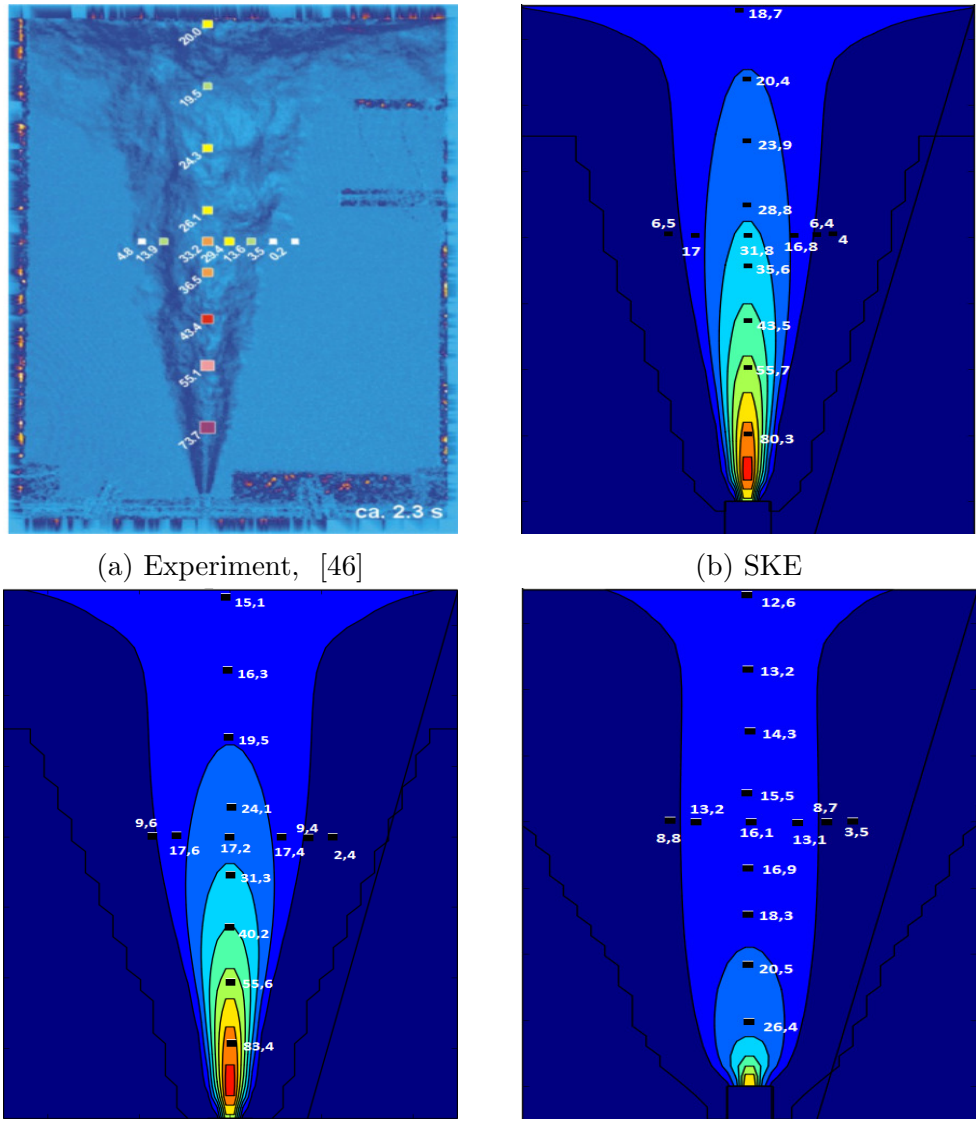

(a) Experiment, [46]

(b) SKE

(c) RNG

(d) Realizable

Figure 4.21: Schlieren picture of the experiment, and concentration at the measurement points [46], and 2D cutting with concentration at MP from simulation for PIE simple geometry, taken at about 2.2 seconds.

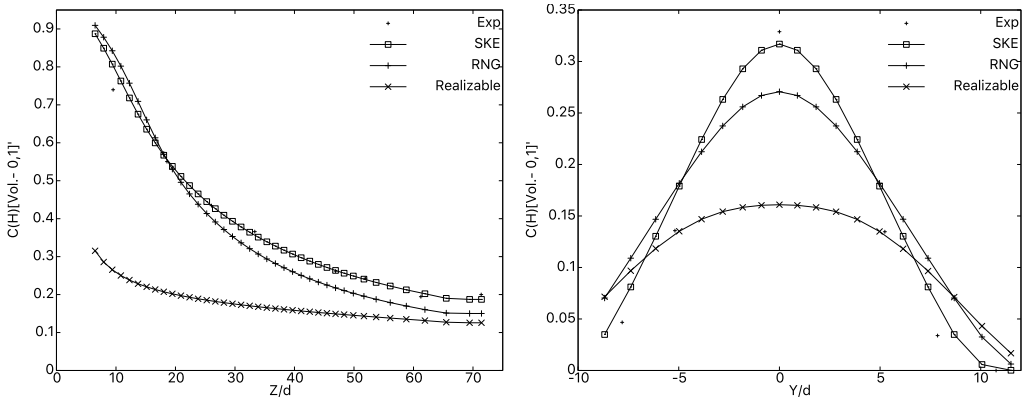

(a) Concentration in z-dir. (b) Concentration in y-dir.

Figure 4.22: Concentration for PIE for simple geometry.

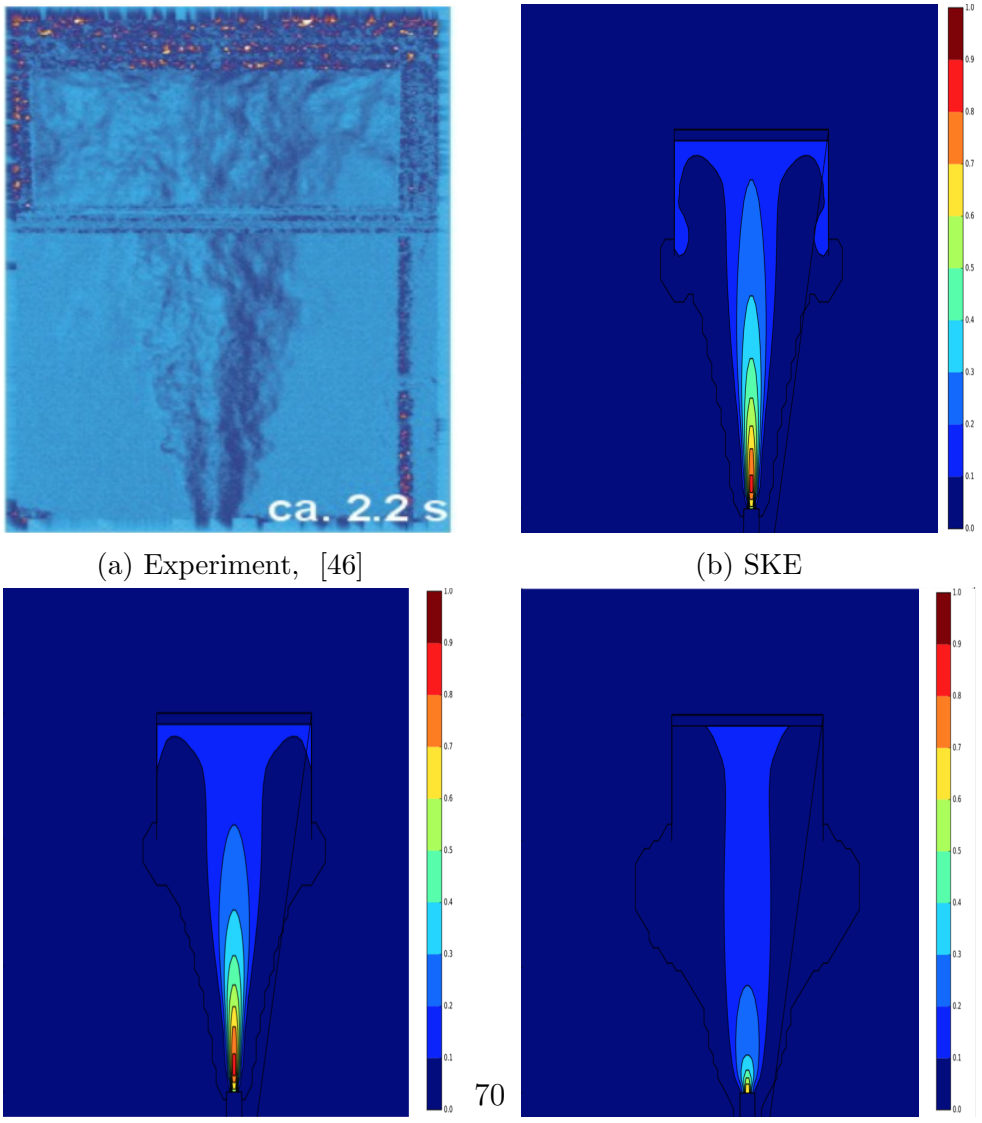

(a) Experiment, [46] (b) SKE

(c) RNG (d) Realizable

Figure 4.23: Schlieren picture of the experiment [46], and 2D cuttings of the three models for PIE complex geometry, taken at about 2.2 seconds.

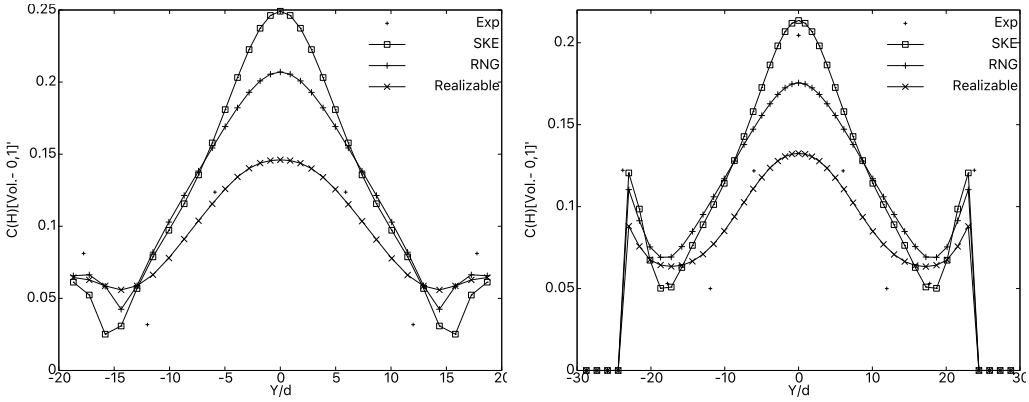

(a) Concentration at z=5L. (b) Concentration at z=5.95L.

Figure 4.24: Concentration for PIE for complex geometry.

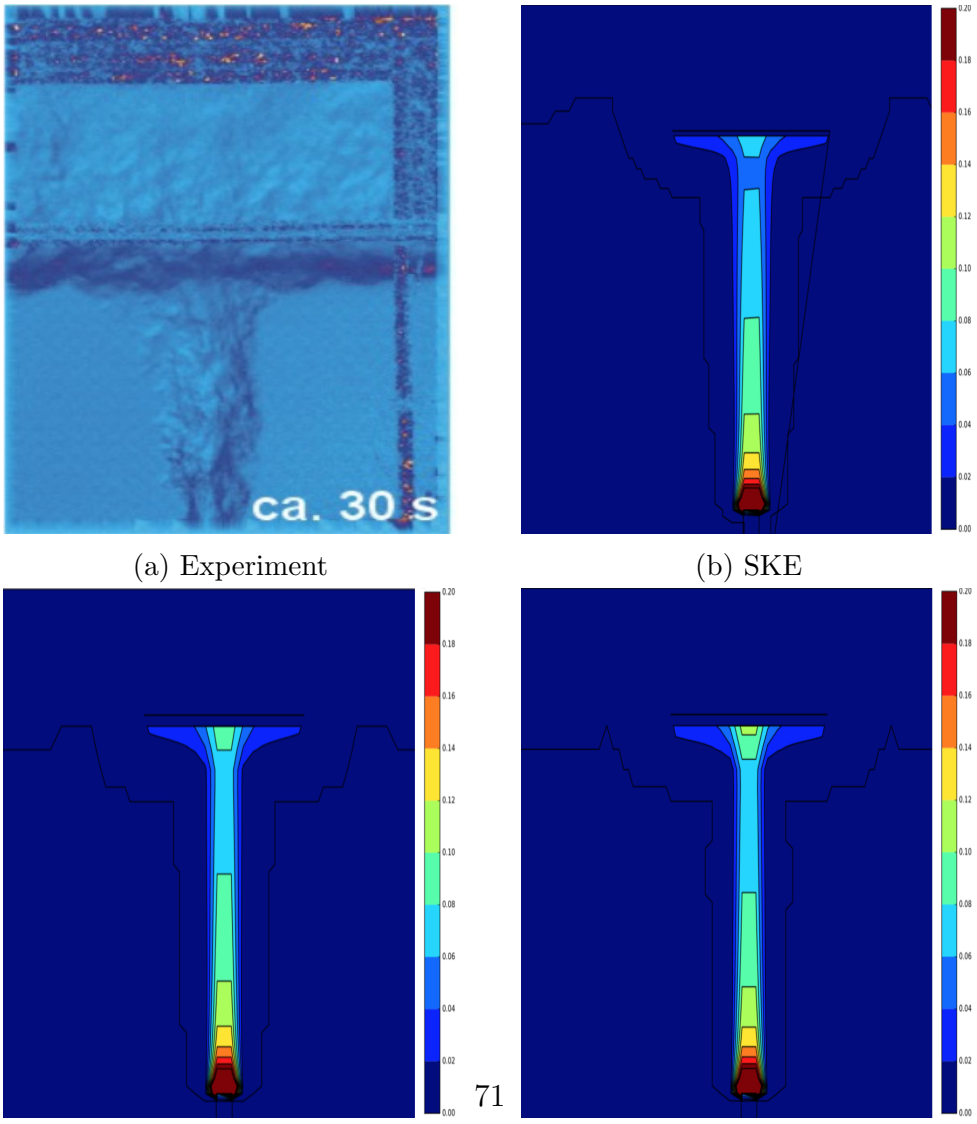

(a) Experiment (b) SKE

(c) RNG (d) Realizable

Figure 4.25: Schlieren picture of the experiment [46], and 2D cuttings of the three models for PIA simple geometry, taken at about 30 seconds.

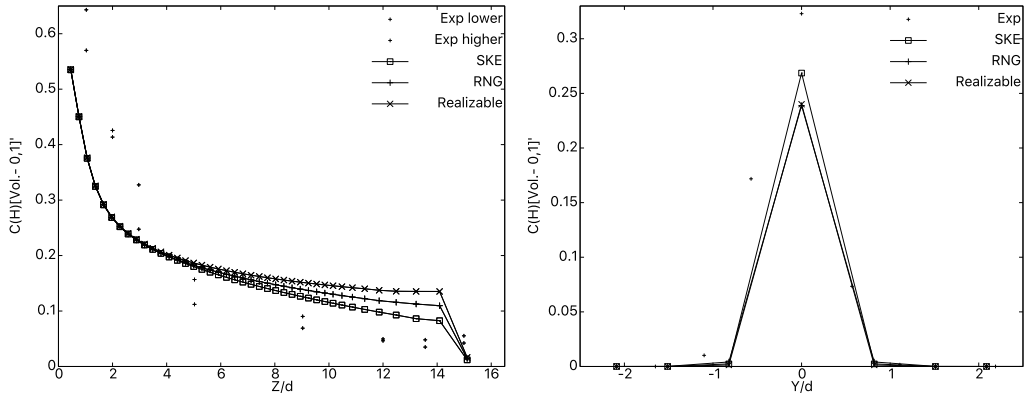

(a) Concentration in z-dir. (b) Concentration in y-dir.

Figure 4.26: Concentration for PIA for simple geometry.

4.3.4 Discussion

The purpose of this case study was to examine which of the turbulence models, SKE, RNG and Realizable, would best predict a high and low momentum buoyant jet with impingement. The following findings will be discussed: (1) SKE provided the most accurate results for both high and low momentum jet, (2) Realizable did not seem to properly predict the jet dispersion for the high momentum case (both geometries), but it provided reasonable results for the low momentum jet.

All the models were numerical stable. For all the simulations, SKE used about half the run time compared to the other two models. RNG and Realizable used approximately the same run time ($\pm$ 4 hours) for all the scenarios. This time difference between SKE and the other two models was considered significant. In addition, because SKE provided the most accurate concentration values compared to the experimental data, SKE was considered the best suited model for all three setups. That SKE simulated these experimental setups satisfactory has been found in a previous study. In a study by Middha and colleagues, [48] they simulated the same experimental setup with FLACS, but they only used SKE.

In the high momentum jet case, for both geometries, it was seen that Realizable predicted a too low concentration value and a wider spread, compared to the experiment. SKE and RNG, on the other hand, both predicted similar concentration and jet width. Both these models also provided results more similar to the experiment.

A possible reason for Realizable predicting a too wide jet may be that Realizable produced too much TKE, and dissipated too little turbulent kinetic energy at the release. When comparing the k and ϵ predicted by SKE with the predicted values by Realizable, it was found that SKE and Realizable had about equal dissipation rate, but Realizable had a higher TKE, at the release. This increase in TKE will lead to an increase in mixing, resulting in a wider spread of the jet. This may have its origin in that Realizable does not include the turbulent viscosity in the production term of the dissipation rate. For SKE and RNG, the turbulent viscosity is included in the production of the k and ϵ equation, and consequently, a large value is balanced out by a contradicting large value. Thus, it might be that the high momentum creates a high turbulent viscosity that is not balanced out by an increase in production of dissipation in the Realizable model, as it does for RNG and SKE. However, this is not considered a logical explanation, as the Realizable model was built for impinging flows in order to reduce the turbulence. As well as no previous studies have reported similar problems with Realizable.

Another possible reason might therefore be that the results from Realizable were taken at a transient time. Realizable has been reported to need a longer computational time compared to the other models in previous studies, and this could imply that Realizable needs longer time to reach the same stage as the other models, which might have affected the wider spread and too low concentration values produced by the model. The jet for the high momentum was measured over a short time span, between 3 to 4 seconds and all models were stopped at this time. While SKE and RNG may have had the time to reach a steady-state, Realizable might have needed a longer computational time in order to reach a similar state. If Realizable was in a more transient state, this might explain the lower concentration values as that is typical for transient leaks [20]. However, if the experimental result should also have been in a transient state, which it might, this implies that SKE and RNG was better able to predict the transient state of the experiment. Whereas Realizable needs longer computational time, and is not able to take in the changes in concentration. To be able to properly predict a transient dispersion is equally important as predicting dispersion that do reach a steady state [20].

Another possible reason for Realizable predicting a too low concentration and too wide jet might be that the interaction of turbulence created from buoyancy functioned poorly for the model. It might be that a different modelling of buoyancy could alter the results, and possibly enhance Realiz-

able's results. In a study by Maele and Merci [43], they found that a new improved model of buoyancy enhanced the performance of Realizable more than for SKE. However, as neither SKE nor RNG seemed to have a problem with how the buoyancy was modelled, this is not a likely explanation. Both these models were therefore considered better suited for this case.

For the low momentum jet, it seemed that Realizable was much more capable to reconstruct and predict the experimental dispersion. As the low momentum jet was measured over a longer time span, about 75 seconds, it is possible that all the models reached a steady state, while for the high momentum jet, Realizable still was in a transient condition, or later developed compared with the other two models.

As Realizable was capable to simulate the dispersion satisfactory for the low momentum jet, it is possible that the interaction between the buoyancy model Realizable was not wrong. It was also for the low momentum jet that the buoyancy had the largest effect. However, in the low momentum jet, the interaction between the buoyancy term and Realizable had a longer time to interact than for the high momentum jet. Consequently, it may be the interaction between the modelling of buoyancy and Realizable created an fluctuation in the results, that was dampened over a longer time span. Nonetheless, as the buoyancy term was equal for all models, and the other models provided good results, this was also not considered likely.

4.4 Case 4: Dense jet in a complex urban environment

For the last case an experiment that consisted of a dense jet released in an open-air industrial site was used. The experimental industrial site and data was built and provided from the university of Surrey [49]. This was a transient release with varying parameters, including wind (speed and direction), temperature, and pressure. Where it was measured a mean concentration over a long duration of time. The geometrical model included buildings and representation of the terrain surface. This makes for an interesting study of a complex geometry in a realistic scenario, to use for RANS model validation.

4.4.1 Experimental case

The industrial site used in the experiment was made for a project called EMU (Evaluation of Modelling Uncertainty) [49]. The EMU project's goal was to evaluate the sensitivity of results to the way a CFD code is applied [49]. The industrial site was an open-air site, implying that parameters such

as wind, temperature, atmosphere and pressure were not controlled. The industrial site consisted of several buildings that varied in size and shape. The buildings were located on a terrain with height variations ranging from zero to 30 meters and covering a horizontal area of about $1km^2$ (1km $\times$ 1km). An overview of the site can be seen in figure 4.27. Figure 4.27a shows where the MPs and leak is placed as well as a centre line going through the centre of the rows of MPs. For a more detailed description about the industrial site and experiment, see Hall [49, 50].

In the experiment, chlorine was released continuous through a nozzle with diameter of 1.74 m (used as L), and with a release rate of 230 kg/s. Consequently, this is a very large release, similar to a severe industrial accident scenario. Thus the experiment can be regarded as "full scale". The gas was released in a north-west direction. In addition, a wind was reported to blow in a north-west direction and was reported as stable, and at standard conditions [49]. The averaged wind speed was 5 m/s (used as characteristic velocity, U_{ref}), at a reference height of 10 m. The Reynolds number of the jet, based on the nozzle diameter and exit velocity was 13.11×10^6. The Reynolds number based on wind was calculated by using the wind speed and the length of a wall on the largest building (27×10^6) and the length of a wall on the smallest building (9.3×10^5). Accordingly, both the air and the jet at the release were turbulent. The densimetric Froude number for this case was 9.94, implying that density effects were large.

116 measurement probes were placed on the industrial site at different X, Y and Z positions. Only concentration was measured. The probes were placed in rows downwind of the leak, as close as 31.6L and as far as 402.3L from the leak (the probes placement is illustrated in figure 4.27a). The probes measured the concentration continuously for 900 seconds, and the mean concentration was calculated. No information about the accuracy of the probes was given in the experimental reports, and only mean concentration was reported, no time evolving data.

4.4.2 Simulation setup

The geometry of the experiment was constructed in FLACS according to specification provided from the article and report concerning the experiment [49, 50]. The geometry had to be rotated in order for the buildings to be in line with the Cartesian grid. This rotation of the buildings implied that everything from monitor points, leak direction, wind direction and terrain also was rotated. The terrain data was provided by [49], and was uploaded

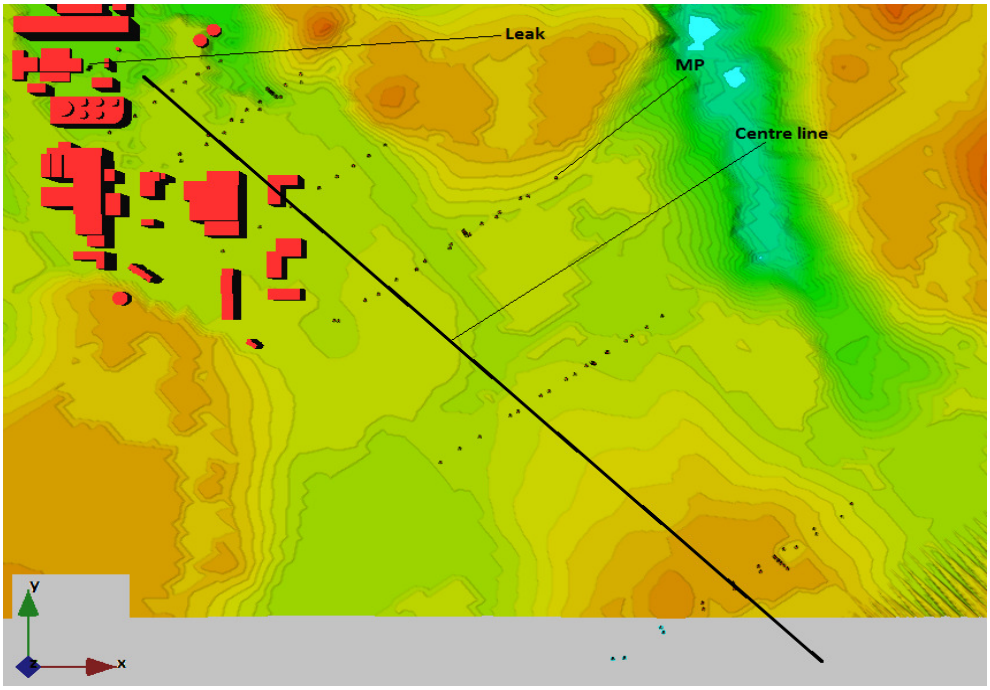

(a) Overview of MP placement, leak placement and centre line. Some of the MPs goes outside of the terrain, but was included in the simulations.

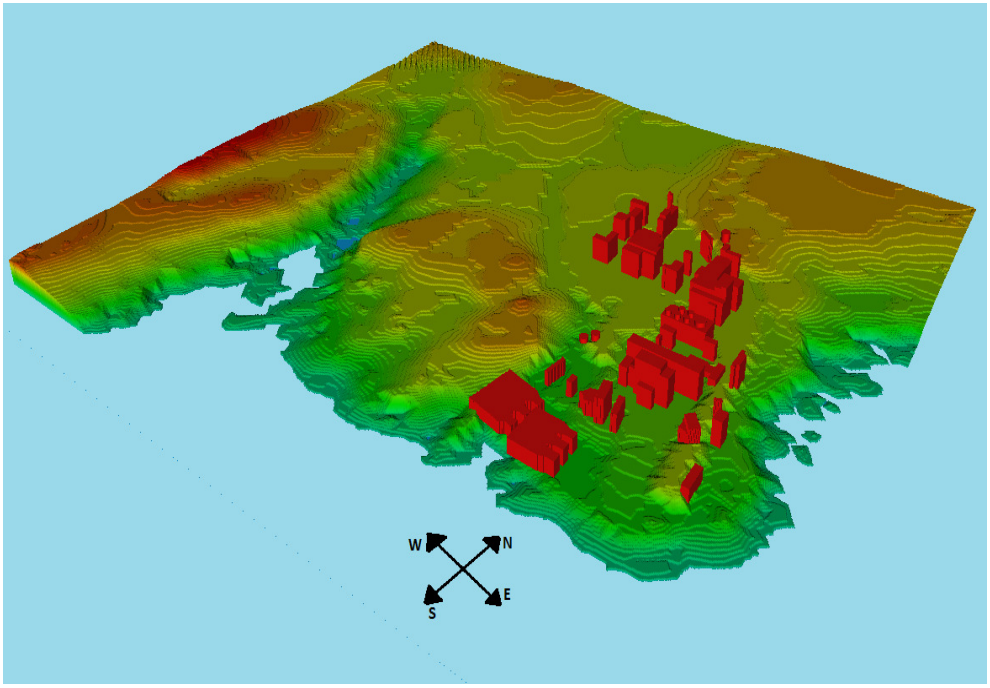

(b) Overview of the industrial site, with North- West- South- East- direction.

Figure 4.27: Overview of case geometry.

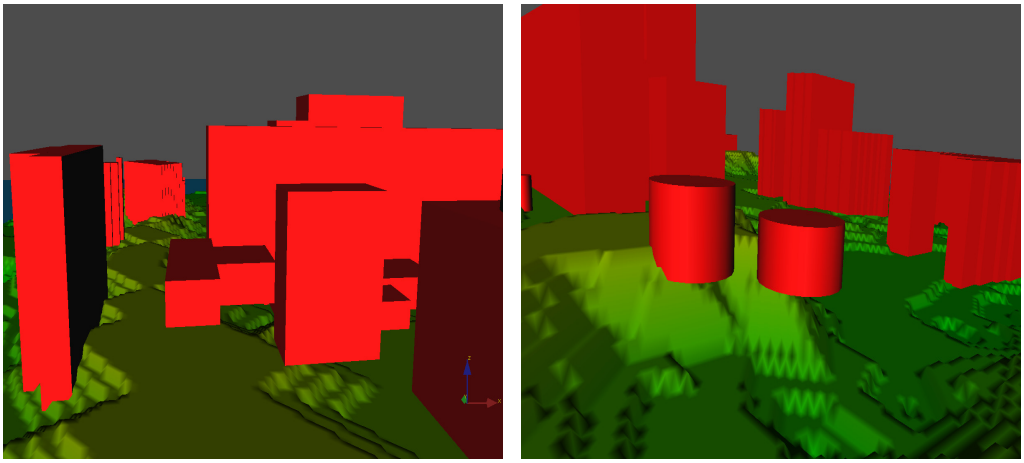

(a) (b)

Figure 4.28: Some of the buildings are inside the terrain, while some are above.

in FLACS. The terrain had a resolution of $1m^2$, which provides imprecise building placements in the terrain. This problem can be seen in figure 4.28, where either the buildings were partially above the ground or partially inside the ground. Accordingly, if a building did not match the terrain, the buildings placement was adjusted vertically in order for the bottom surface to cover as much as the terrain as possible.

The simulation volume included all the terrain and was, x: 1011.5L to 1465.5L, y: 2873.6L to 3362.1L, z: 0L to 86.2L. The simulation volume was divided into a core and a stretched domain. The core domain was centred around the buildings, and was x: 1034.5L to 1229.9L, y: 2902.3L to 3046L, z: 0L to 57.5L. Outside the core domain the stretched domain started and continued until the end of the simulation domain. The core domain consisted of a constant grid cell size, except around the release, while the stretched grid was built up of grid cells that increased in size. The grid was refined around the leak in order to get the correct area of the leak. As this simulation volume was quite large, large grid cells were used to cover the whole domain. The smallest grid cell in the core domain of all the simulations was $1.72L^3$.

Boundary conditions were defined as nozzle at the outflow of X and inflow of Y. The remaining boundaries were defined as wind. Solid walls from buildings and terrain imposed a no-slip boundary. Initial conditions about temperature and pressure was reported to be at standard condition, no information

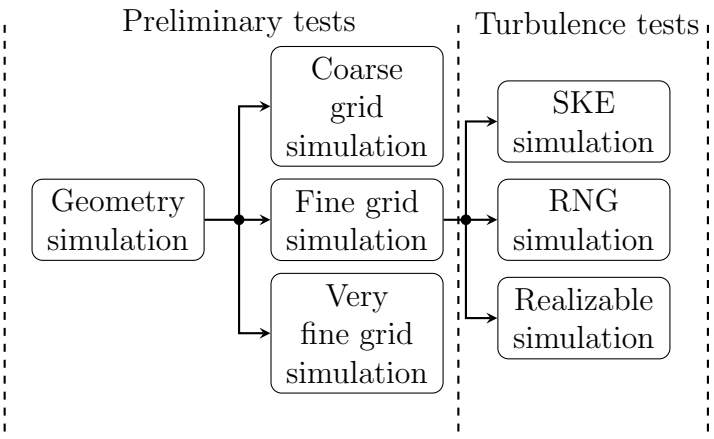

Figure 4.29: Flow chart, presenting in which order the simulations were performed.

about initial turbulence was provided.

In the simulations, MPs were defined at every measurement probes' placement. The MPs measured concentration (as in the experiment), as well as k, ϵ and velocity. The MPs made it possible to do direct comparisons of experimental and simulated data for concentration, and to do model comparisons for the other quantities. Only a visual comparison of graphs and CSF values were used[6]. All simulations were run with a time iteration summing up to 1100 seconds. The wind was given a build up time of 200 seconds before the gas was released. In accordance with the experiment, mean values for 900 seconds were calculated.

Figure 4.29 represents a flow chart of all the tests that were conducted, and in which order they were performed. As a first step Preliminary tests were done in the following order: Firstly a geometry simulation was performed to control that the geometry was satisfactory. Secondly a grid sensitivity test was performed. Based on the preliminary tests the Fine grid was chosen, and the turbulence tests were performed based on this. The process, and the choices made, will be presented in greater detail below.

For the sensitivity tests, three different grids were used: coarse grid, fine grid and very fine grid. Table 4.15 shows a detailed description of the sensitivity tests, including the grid cell size used and the number of grid cells in the simulation volume.

[6]see case 1 section 4.1.2 for a definition of CSF

Table 4.15: Test name along with a short description, number of grid points in the grid, N_i, and the average grid cell size in the core domain, $\Delta i_{\min}$ for the remaining preliminary tests.

Type of test	Description	Number of grid cells	Average grid cell size in core domain [m]
Coarse grid	This is a coarse grid	Nx - 105 Ny - 90 Nz - 36	$\Delta X_{min} - 5$ $\Delta Y_{min} - 5$ $\Delta Z_{min} - 5$
Fine grid	This is a finer grid than the coarser grid, in all directions	Nx - 126 Ny - 104 Nz - 37	$\Delta X_{min} - 4$ $\Delta Y_{min} - 4$ $\Delta Z_{min} - 4$
Very fine grid	This is a finer grid than the fine grid grid, in all directions	Nx - 146 Ny - 127 Nz - 47	$\Delta X_{min} - 3$ $\Delta Y_{min} - 3$ $\Delta Z_{min} - 3$

The results of the grid sensitivity tests can be seen in figure 4.30. Here, it seems as the fine grid has closest values to the experiment than the coarse grid, as well as there seems no great difference between very fine grid and fine grid. Therefore, it was considered that a further refinement of the grid for fine grid was necessary, as it did not increase the accuracy. The fine grid was therefore considered the best choice and was further used for the turbulence testing.

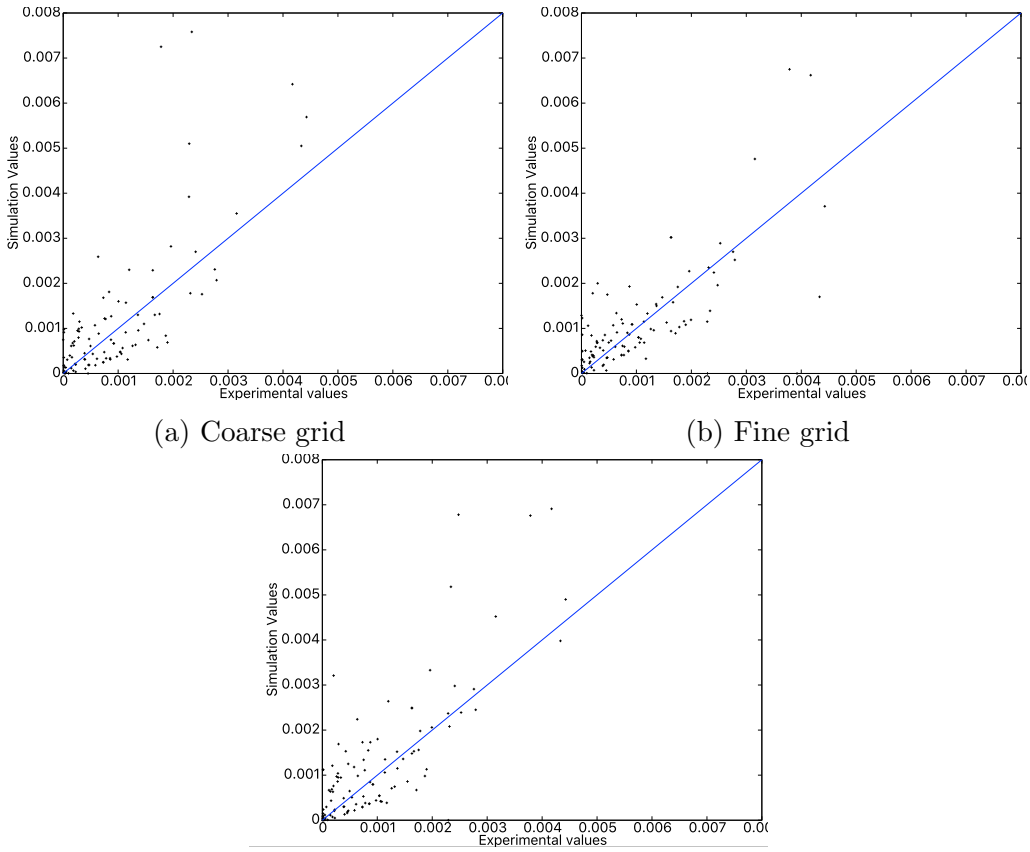

(a) Coarse grid

(b) Fine grid

(c) Very fine grid

Figure 4.30: Scatterplots from grid sensitivity testing, showing measured concentration values vs simulated concentration values.

4.4.3 Results

All models produced reasonable answers and showed good concentration profiles. Table 4.16 presents the simulated clock time. As shown in the table, SKE and RNG have about the same run time, while Realizable used 3 to 4 hours longer. This was not deemed a significant difference, as it is only a slight increase in time compared to the total time used for all the models.

Table 4.16: Clock time used for simulation with the different models.

Model	SKE	RNG	Realizable
Time[hour]	48.41	49.14	52.83

Table 4.17 show the CSF values for each row of MPs. As presented in the table, SKE and RNG have about equal CSF value at all rows. From the CSF values one can see that SKE and RNG always underpredicts the maximum concentration for the first 4 rows of MPs, whereas for the last two rows of MPs they overpredict the maximum concentration. Realizable, on the other hand underpredicts the maximum concentration of the two first rows of MPs. For the last four rows of MPs Realizable overpredicts the maximum concentration, especially for the last row.

Table 4.17: Concentration safety factor values for the three turbulence models for all rows.

	SKE	RNG	Realizable
Row 1	0.777	0.760	0.809
Row 2	0.811	0.790	0.948
Row 3	0.903	0.863	1.175
Row 4	0.838	0.777	5.600
Row 5	1.782	1.83	5.862
Row 6	4.399	4.985	8.002

Figures 4.31, 4.32 and 4.33 present the concentration values measured by the MPs. The horizontal axis represent normalised distance from the centre line and the vertical axis represents concentration values. Note that the MPs vary in height, some are close to the floor while other are higher up, this is not represented by any figure. SKE and RNG exhibits quite similar concentration values at all rows, whereas Realizable seems to provide higher concentration values, especially farther away from the release. It seems as all the models provide good concentration for the rows of MPs that is close to the buildings (row 1 to 3), while moving farther away from the buildings to the open field (row 4 to 6), Realizable overpredicts much, whereas SKE and RNG show more similar values compared to the experiment. At the MP rows farthest from the leak all models gives too high concentration values, compared to the experiment. Further investigation showed that for this case the width of the jet seemed to be equal for all models.

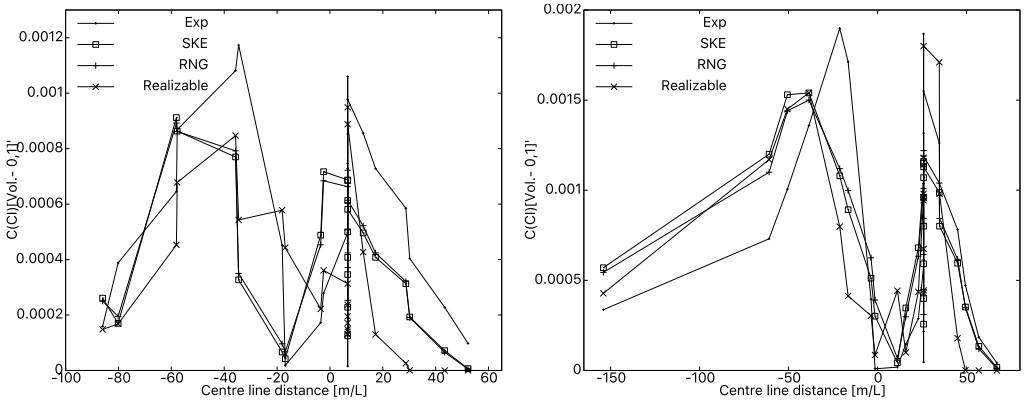

(a) First row of MP from the leak. (b) Second row of MP from the leak

Figure 4.31: Concentration of the first two rows of MPs.

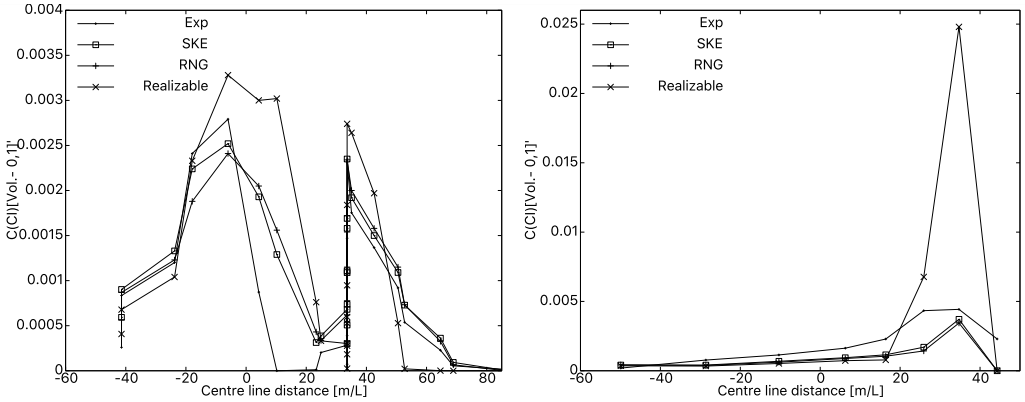

(a) Third row of MP from the leak. (b) Fourth row of MP from the leak.

Figure 4.32: Concentration of the third and fourth rows of MPs.

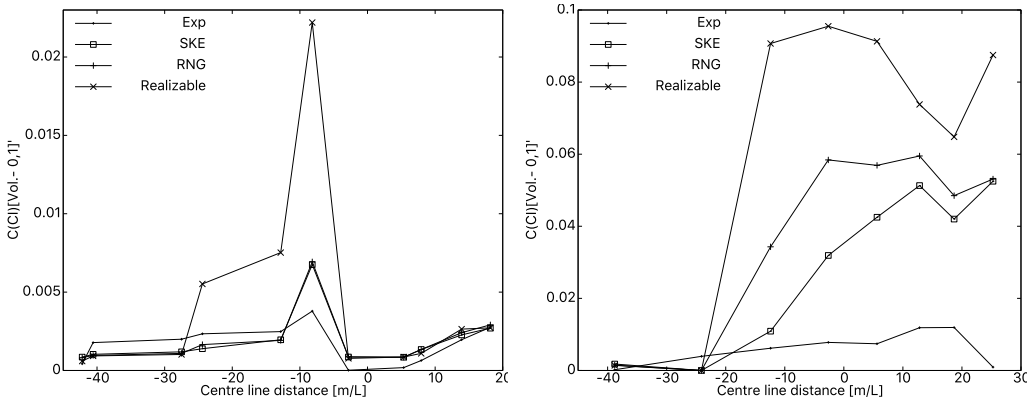

(a) Fifth row of MP from the leak. (b) Sixth row of MP from the leak.

Figure 4.33: Concentration of the last two rows of MPs.

It was performed an investigation of how the variables (concentration, velocity and TKE), measured by the MPs for each turbulence model, evolved over time. Both SKE and RNG were found to have small fluctuations in all the measured variables for the first 400 seconds after the gas was released. Realizable, on the other hand, had larger fluctuations that continued for the whole simulation time, indicating it did not, or perhaps will not, reach a steady state.

4.4.4 Discussion

The purpose of this case was to examine which of the three turbulence models, SKE, RNG and Realizable, would best predict a dense high momentum jet dispersed in an obstructed site. The following findings will be discussed: (1) of the three models, both SKE and RNG seemed to simulate the concentration values most accordingly to the experiment in the best time frame, (2) it seemed like Realizable depicts large fluctuations in the measured variables where the other two models show little fluctuations over the measured duration time span.

Both SKE and RNG provided concentration values that better resembles the experimental profile compared to Realizable. Both had CSF values that where closer to 1, compared to Realizable. When the concentration was measured around the buildings (MP rows 1 to 3) it seems as all the models produced about equal concentration, all CSF values is also about 1. Whereas, when the concentration was measured in the open field (MP rows 3 to 5) it seems as Realizable is overpredicting its concentration values. This can also be seen in the CSF values, where the maximum concentration is overpre-

dicted 5 to 8 times compared to experimental values. However, SKE and RNG also overpredicted the concentration in the open field. Nonetheless, all models seemed to be able to produce satisfactory results for a complex large-scale geometry.. Both SKE and RNG operated inside the same range in computational time ($\pm$ 0.5 hours), whereas Realizable used about three to four hours longer. This extra time may not be considered significantly longer considering the total model computational time. SKE and RNG provided the best results with the shortest time, and were therefore considered the best models for this scenario.

It might be that the fluctuations in the measured variables exhibit by Realizable was the reason for its lesser performance compared to SKE and RNG. The concentration values provided in the graphs are the mean values of each MP over 900 second. As this is a quite large timespan to measure, any fluctuations would probably be evened out and consequently Realizable showed reasonable results. However, if the time duration had been shorter it might be that these fluctuations would have provided unreasonable results for Realizable. It also seemed that SKE and RNG would have reached a steady-state, while Realizable would have continued to fluctuate, and thus only reach a quasi-steady state with large deviations. It is possible that without the fluctuations Realizable would have performed as good as SKE and RNG.

The fluctuation does not seem to have any physical origin, and it was only Realizable that showed it. Further investigation found that the mass residual was always under FLACS iteration criteria (mass residual less than 10^{-4}), therefor Realizable did not have a problem of convergence. Thus, it could be a problem within the model instead. It is possible that the fluctuations was caused by the set of equations used, or by the implementation of the equations into FLACS. However, Realizable is a highly tested and widely used turbulence model, and no one has ever reported a similar behaviour in the literature. That the equations might be producing fluctuations is therefore believed to be highly unlikely. As Realizable was newly implemented into FLACS, it could be possible that the implementation has some issues. Furthermore, it is not likely that the implementation of other parameters, including the geometry and terrain, caused the fluctuations, as none of the other models showed similar problems, and the models gave reasonable results.

It is possible that the C_μ term in the eddy viscosity model of Realizable caused the fluctuations. As the velocity fluctuates consistently with the concentration and turbulence for Realizable and as C_μ is a function of velocity,

it is possible that they operated in a loop, where one enlarged the other.

In conclusion: the results from this case study suggest that SKE and RNG were better suited for simulating the experiment, as they had higher concentration values and performed in a better time frame than Realizable. However, as Realizable had large fluctuations, it is possible that this affected the results, making Realizable to perform more poorly than the other models. It is therefore recommended that further studies using Realizable should be carried out in order to test if the model shows fluctuations in other gas dispersion scenarios.

5 Discussion

The aim of the study was to assess three well-known RANS two-equation eddy viscosity models, in four different gas dispersion cases. The purpose was to evaluate the models' behaviour compared to experimental data, in order to see which of the models was best suited for predicting dispersion scenarios. Also, a CFD software that uses partially resolved geometry was used to see its effect. The findings indicate that SKE was the best-suited model for most of the cases tested in this study, in addition to always providing satisfactory results. However, RNG also provided reasonably results in all cases suggesting that this might also be a satisfactory model for simulating gas dispersion. Realizable generally used the longest computational time, and was found the least suitable model for 3 out of 4 cases. The appendix gives a schematic summary of the results found in this study. That can be regarded as a starting point for further research.

It is a surprising finding that SKE is, overall, the best model, because previous research on the models' performance suggests that the models' predictability is situational, i.e. determined by factors such as the geometry, type of gas and type of release. For instance, RNG is previously reported to behave very well in urban environments and buoyant gases [2, 37, 14], whereas SKE has been found to work good in neutral gas dispersions in urban environments [38]. Realizable, on the other hand, seems to generally work best with dense gas dispersion [4, 36, 39]. Nonetheless, as this study has tested a wide range of dispersion scenarios, where SKE has been the preferred model in 3 out of 4 scenarios, it may be that SKE is the best suited turbulence model for dispersion scenarios.

Furthermore, it is surprising that the SKE was the best suited model, as both RNG and Realizable have been found to better reproduce experimental data, in different comparative studies. For example, Santiago et al., [14], did a comparative study using SKE, RNG and Realizable of a plume dispersion in a street canyon, and found that both RNG and Realizable performed better than SKE. Tominaga and Stathopoulos, [2], simulated a plume dispersion in a street canyon, and found that SKE was not capable of reproducing the flow whereas RNG and Realizable performed very well. This was also found in a study in 2013 by Lateb and colleagues, [7], where SKE gave inadequate results in a buoyant plume dispersion cases, and RNG and Realizable performed equally well. Also in 2014 a study by Rahimi and colleagues, [35], found that both RNG and Realizable provided better results than SKE, for a dense plume dispersion. Similarly, in 2014, a study by Abdi and Bitsuamlak,

[39], who found that both RNG and Realizable were virtually identical, both giving better estimates compared to SKE, in a wind flow simulation on a real complex geometry.

A possible explanation for why SKE was better in this study, is that all the modelled dispersion scenarios used configuration setups where SKE is known to perform good, including setups with high Reynolds numbers, no-swirl and little separation. Consequently, SKE was never put in a situation that challenged its known shortcomings. However, both RNG and Realizable are modifications of SKE, and were developed to overcome these shortcomings. Accordingly, they should have performed equally good as, or even better than, SKE under the same circumstances. Another possible explanation is that SKE operated good inside the experimental measurement region, but not outside this region. In the neutral dispersion case (case 2), it was believed that if the data had been measured over a larger region, RNG might have been better suited to predict the dispersion, as it better predicted the maximum concentration placement.

Even though most of the previous research suggest that SKE is in general the weaker of the three turbulence models, there exist some studies supporting the adequateness of the SKE model. Hang and colleagues (2013), for example, found that SKE was the better suited model of the three in a urban enivroment [38]. Similarly, in an another comparative study of a heated street canyon simulating pollutant by Xie et al in 2006, [3], it was found that all models were equally good.

Even though SKE in general was considered a better suited model for simulating gas dispersion, it does not always predict all the measured phenomena correctly. For example, SKE was not able to predict concentration fluctuations, as used in the dense plume scenario (case 1), or to predict the placement of maximum concentration, as used in the neutral dispersion scenario (case 2). Furthermore, SKE was not found to be superior to the other models; for most of the cases, RNG provided very close values to SKE. However, as information about the experiments' uncertainty was not provided, we do not know if both models operated inside the experiments' uncertainty range. If they did, it is possible that RNG also is a preferred best suited model, equally good as SKE.

A concern, however, is the finding that Realizable performed in an unexpected manner for two of the case scenarios. In the buoyant jet scenario with a gas that was lighter-than-surrounding-fluid (case 3), Realizable simu-

lated a too wide jet for the high momentum release. In the dense jet scenario with a gas that was denser-than-surrounding-fluid (case 4), Realizable showed large fluctuations in the measured variables. Both of these cases where high momentum jets and highly influenced by buoyancy effect. It seemed that for both cases there was some unphysical behaviour of the Realizable model. As there could not be found any previous literature on this problem, it is possible that there is an error with how Realizable is implemented in FLACS.

It could also be that Realizable does not "interact" properly with the subgrid model. It could also be that Realizable is a turbulence model that functions better when all objects are resolved on grid. It is, however, highly recommended that further work should be done on Realizable with FLACS.

5.1 Methodological discussion

Because the results of the study were based on concentration data, the models' accuracy and predictability evaluation was restricted, and a complete picture of the models performances was not provided. However, the experiments considered in the present work have some of the best dispersion data sets with least uncertainties. Consequently, the reported data is of high quality. In general, more information about the surroundings or a wider measurement area could have provided additional information, especially more data on turbulence.

A strength in this study is that the models have been tested in a wide range of dispersion scenarios, using different configuration setups. This provides a large application area of the models. As all models were tested with the same computer and using the same computation capacity, it was possible to compare computational time as a parameter, to characterise the practicality of the models. Lastly, grid sensitivity tests were run for all cases, as well as sensitivity on boundary conditions and other parameters, if deemed necessary. This implies that sources of modelling uncertainty were as limited as possible.

The PDR concept seemed to be a good approach and was easily applicable for all cases. For scenarios involving a subgrid geometry (case 1 and 4) the grid was easily applied and reasonable answers were produced in a good timeframe. It was also seen that variation of the grid size produced minor changes in the result which supports the value of the PDR concept. It did not seem that SKE and RNG had any problems with the interaction of the sub-grid modelling. For Realizable it was seen that the sub-grid model may have had a negative impact on the result for the dense plume scenario (case

1). When the sub-grid objects were removed, there was a great reduction in TKE difference between Realizable and SKE. It may be, that because the realizable condition was violated, the Realizable model dampen all turbulence generation around the roughness elements, which created a wrong TKE profile, and as a consequent, Realizable predicted TKE wrongly outside the plume. Thus is might be that the interaction between the sub-grid model and Realizable model may have function improperly. Nonetheless, the PDR concept for sub-grid modelling generally worked very well and is an excellent way of resolving all objects and terrain in a simple and fast fashion, providing reasonable and accurate results.

6 Conclusion

The aim of the study was to assess three well-known RANS two-equation eddy viscosity models, in four different gas dispersion cases. The purpose was to evaluate the models' behaviour compared to experimental data, in order to see which of the models was best suited for predicting dispersion scenarios. The cases used in the thesis were: CO_2 dispersion in a cross-wind, neutral dispersion in an urban environment, hydrogen jet impinging on a surface, and a dense jet dispersion on an industrial site. Overall, SKE was found to be the best-suited model in three of the four dispersion cases, and provided good results for all the scenarios. However, RNG also provided reasonably results in a practical timeframe, suggesting that it is also a good model for gas dispersion.

As the study was limited to assessing four different dispersion scenarios, more research is needed, especially with complex geometries using sub-grid modelling, in order to establish whether one of these models is better suited for gas dispersion simulations. More research on transient cases, were time evolving data is provided should also be studied, as this has not been covered here. It was also found that the interaction between the turbulence models and the production and destruction of turbulence from sub-grid and the buoyancy modelling may have given unexpected results and research on this should be conducted in order to improve the numerical simulations. Lastly, for a better evaluation of turbulence models, it is desirable to to have more turbulence measurements in experiments, especially for the non-academic setups.

References

[1] RS Cant, WN Dawes, and AM Savill. Advanced CFD and modeling of accidental explosions. *Annu. Rev. Fluid Mech.*, 36:97–119, 2004.

[2] Yoshihide Tominaga and Ted Stathopoulos. Numerical simulation of dispersion around an isolated cubic building: Comparison of various types of k–ε models. *Atmospheric Environment*, 43(20):3200–3210, 2009.

[3] Xiaomin Xie, Chun-Ho Liu, Dennis YC Leung, and Michael KH Leung. Characteristics of air exchange in a street canyon with ground heating. *Atmospheric Environment*, 40(33):6396–6409, 2006.

[4] SM Tauseef, D Rashtchian, and SA Abbasi. CFD-based simulation of dense gas dispersion in presence of obstacles. *Journal of Loss Prevention in the Process Industries*, 24(4):371–376, 2011.

[5] Jonas Allegrini, Viktor Dorer, and Jan Carmeliet. Buoyant flows in street canyons: Validation of CFD simulations with wind tunnel measurements. *Building and Environment*, 72:63–74, 2014.

[6] Egon Krause. Computational fluid dynamics: its present status and future direction. *Computers & fluids*, 13(3):239–269, 1985.

[7] M Lateb, C Masson, T Stathopoulos, and C Bédard. Comparison of various types of k–ε models for pollutant emissions around a two-building configuration. *Journal of Wind Engineering and Industrial Aerodynamics*, 115:9–21, 2013.

[8] F Scargiali, F Grisafi, A Busciglio, and A Brucato. Modeling and simulation of dense cloud dispersion in urban areas by means of computational fluid dynamics. *Journal of hazardous materials*, 197:285–293, 2011.

[9] Jr John D. Anderson. *Computational Fluid Dynamics The Basics With Applications*. McGraw-Hill Book Co., New York, 1995.

[10] Yoshihide Tominaga and Ted Stathopoulos. CFD simulation of near-field pollutant dispersion in the urban environment: A review of current modeling techniques. *Atmospheric Environment*, 79:716–730, 2013.

[11] Tania S Klein. *The development and application of two-time-scale turbulence models for non-equilibrium flows*. PhD thesis, University of Manchester, 2012.

[12] Stephen B. Pope. *Turbulent Flows*. Cambridge University Press, New York, 8th edition, 2011.

[13] Brian Edward Launder and DB Spalding. The numerical computation of turbulent flows. *Computer methods in applied mechanics and engineering*, 3(2):269–289, 1974.

[14] JL Santiago, F Martin, A Cuerva, N Bezdenejnykh, and A Sanz-Andres. Experimental and numerical study of wind flow behind windbreaks. *Atmospheric Environment*, 41(30):6406–6420, 2007.

[15] Benjamin R Cormier, Ruifeng Qi, GeunWoong Yun, Yingchun Zhang, and M Sam Mannan. Application of computational fluid dynamics for LNG vapor dispersion modeling: A study of key parameters. *Journal of Loss Prevention in the Process Industries*, 22(3):332–352, 2009.

[16] V.D Narasimhamurthy, H. Hisken, G. Atanga, and T. Skjold. Porosity/distributed resistance modelling for industrial CFD applications. In *Eighth National Conference on Computational Mechanics, MekIT'15, 18-19 May 2015, Trondheim, Norway, B. Skallerud, H.I. Andersson (Eds), International Center for Numerical Methods in Engineering (CIMNE)*, pages 321–331, 2015.

[17] W. Rodi and C.J. Chen. *Vertical turbulent buoyant jets – review of experimental data*. Pergamon Press, New York, 1980.

[18] W. Rodi. *Turbulent buoyant jets and plumes*. Pergamon Press, New York, 1982.

[19] Rajesh Kumar and Anupam Dewan. URANS computations with buoyancy corrected turbulence models for turbulent thermal plume. *International Journal of Heat and Mass Transfer*, 72:680–689, 2014.

[20] JS Puttock, DR Blackmore, and GW Colenbrander. Field experiments on dense gas dispersion. *Journal of Hazardous Materials*, 6(1):13–41, 1982.

[21] EA Brizuela. Errors due to correlations in evaluating mean density from Favre-averaged enthalpy and composition in turbulent reactive flow. *Combustion and flame*, 103(4):343–347, 1995.

[22] William K George. Lectures in turbulence for the 21st century. *Chalmers University of Technology*, 2009.

[23] J. Warnatz, U. Maas, and R.W. Dibble. *Combustion: physical and chemical fundamentals, modelling and simulations, experiments, pollutant formation*. Springer, Germany, 4th edition, 1996.

[24] Victor Yakhot and Steven A Orszag. Renormalization-group analysis of turbulence. *Physical review letters*, 57(14):1722, 1986.

[25] Tsan-Hsing Shih, William W Liou, Aamir Shabbir, Zhigang Yang, and Jiang Zhu. A new k-ϵ eddy viscosity model for high Reynolds number turbulent flows. *Computers & Fluids*, 24(3):227–238, 1995.

[26] Lars Davidson. Fluid mechanics, turbulent flow and turbulence modeling. Division of Fluid Dynamics, Department of Applied Mechanics, Chalmers University of Technology, 2015.

[27] TS Klein, TJ Craft, and H Iacovides. Assessment of the performance of different classes of turbulence models in a wide range of non-equilibrium flows. *International Journal of Heat and Fluid Flow*, 51:229–256, 2015.

[28] François G Schmitt. About boussinesq's turbulent viscosity hypothesis: historical remarks and a direct evaluation of its validity. *Comptes Rendus Mécanique*, 335(9):617–627, 2007.

[29] WP Jones and BEi Launder. The prediction of laminarization with a two-equation model of turbulence. *International journal of heat and mass transfer*, 15(2):301–314, 1972.

[30] Francis Harvey Harlow and Paul I Nakayama. Transport of turbulence energy decay rate. Technical report, Los Alamos Scientific Lab., N. Mex., 1968.

[31] VSASTBCG Yakhot, SA Orszag, S Thangam, TB Gatski, and CG Speziale. Development of turbulence models for shear flows by a double expansion technique. *Physics of Fluids A: Fluid Dynamics (1989-1993)*, 4(7):1510–1520, 1992.

[32] G Evola and V Popov. Computational analysis of wind driven natural ventilation in buildings. *Energy and buildings*, 38(5):491–501, 2006.

[33] JD Posner, CR Buchanan, and D_ Dunn-Rankin. Measurement and prediction of indoor air flow in a model room. *Energy and buildings*, 35(5):515–526, 2003.

[34] Gexcon AS. Flacs v10.4r2 user's manual. Technical report, 2015.

[35] A Rahimi, T Tavakoli, and S Zahiri. Computational fluid dynamics (CFD) modeling of gaseous pollutants dispersion in low wind speed condition: Isfahan refinery, a case study. *Petroleum Science and Technology*, 32(11):1318–1326, 2014.

[36] Hossein Kheirkhah Gildeh, Abdolmajid Mohammadian, Ioan Nistor, and Hazim Qiblawey. Numerical modeling of 30ˆ{\ circ} and 45 {ˆ\ circ} inclined dense turbulent jets in stationary ambient. *Environmental Fluid Mechanics*, 15(3):537–562, 2015.

[37] TL Chan, G Dong, CW Leung, CS Cheung, and WT Hung. Validation of a two-dimensional pollutant dispersion model in an isolated street canyon. *Atmospheric environment*, 36(5):861–872, 2002.

[38] Jian Hang, Zhiwen Luo, Mats Sandberg, and Jian Gong. Natural ventilation assessment in typical open and semi-open urban environments under various wind directions. *Building and environment*, 70:318–333, 2013.

[39] Daniel S Abdi and Girma T Bitsuamlak. Wind flow simulations on idealized and real complex terrain using various turbulence models. *Advances in Engineering Software*, 75:30–41, 2014.

[40] J. Havens and T. Spicer. Vapor dispersion and thermal hazard modelling. Technical report, Chemical Hazards Research Center Departmen of Chemical Engineering University of Arkansas, 2006.

[41] S Coldrick, CJ Lea, and MJ Ivings. Validation database for evaluating vapor dispersion models for safety analysis of LNG facilities, guide to the LNG model validation database. *Health and Safety Laboratory, Buxton, UK*, 2010.

[42] Rajesh Kumar and Anupam Dewan. Assessment of buoyancy-corrected turbulence models for thermal plumes. *Engineering Applications of Computational Fluid Mechanics*, 7(2):239–249, 2013.

[43] Karim Van Maele and Bart Merci. Application of two buoyancy-modified k–ε turbulence models to different types of buoyant plumes. *Fire Safety Journal*, 41(2):122–138, 2006.

[44] M Schatzmann, K Marotzke, and J Donat. Research on continuous and instantaneous heavy gas clouds. *Contribution of sub-project EV 4T-0021-D to the final report of the joint CEC-project, University of Hamburg*, 1991.

[45] M. Schatzmann and R.N. Meroney. A1-5 dispersion around a rectangular building. http://www.mi.zmaw.de/index.php?id=628, 2012.

[46] A Friedrich, J Grune, N Kotchourko, A Kotchourko, K Sempert, G Stern, and M Kuznetsov. Experimental study of jet-formed hydrogen-air mixtures and pressure loads from their deflagrations in low confined surroundings. In *Proceedings of 2nd international conference on hydrogen safety, San Sebastian, Spain*, pages 11–13, 2007.

[47] R Viskanta. Heat transfer to impinging isothermal gas and flame jets. *Experimental thermal and fluid science*, 6(2):111–134, 1993.

[48] Prankul Middha, Olav R Hansen, Joachim Grune, and Alexei Kotchourko. CFD calculations of gas leak dispersion and subsequent gas explosions: validation against ignited impinging hydrogen jet experiments. *Journal of hazardous materials*, 179(1):84–94, 2010.

[49] RC Hall. Evaluation of CFD modelling of gas dispersion near buildings and complex terrain. 144:293–304, 1999.

[50] R.C. Hall. Evaluating modelling uncertainty - project EMU final report. Technical report, WS Atkins Report WSA/AM5017/R7, 1997.

Appendix

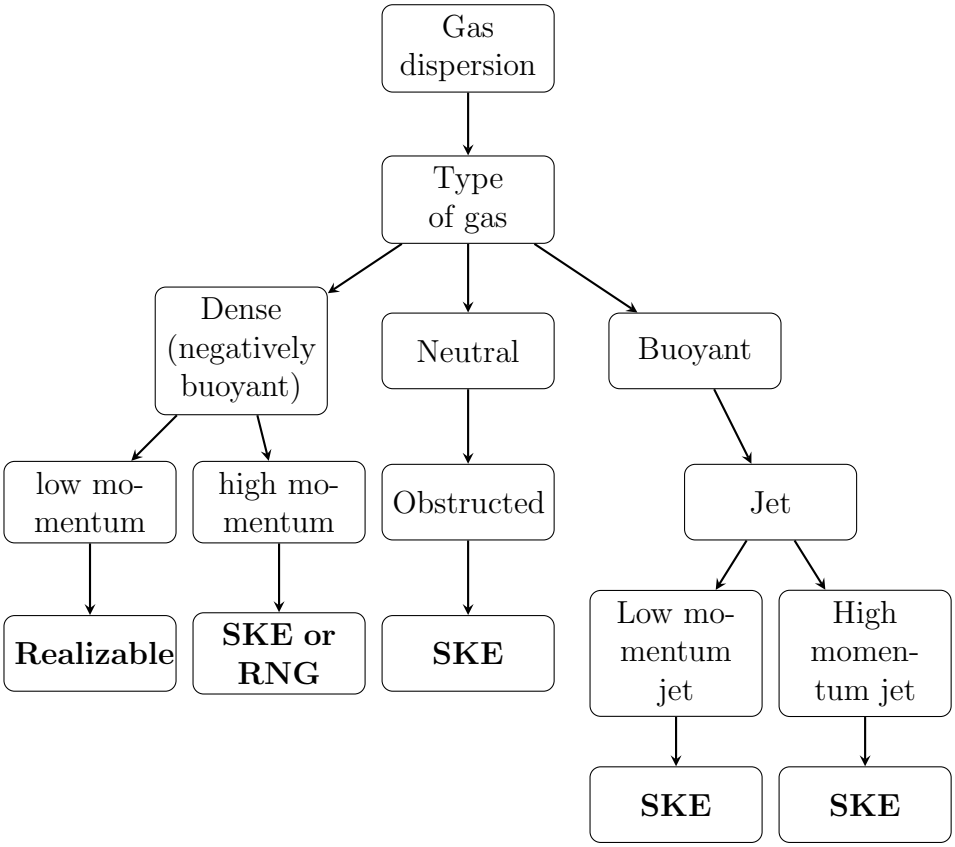

Figure 6.1: Overview of the findings, and possible guideline for further studies on turbulence modelling in gas dispersion simulations